8-2020

Exploring Structural and Electronic Properties of Triangular Adatom Layers on the Silicon Surface Through Adsorbate Doping

Tyler S. Smith
University of Tennessee, Knoxville, tsmit146@vols.utk.edu

To the Graduate Council:

I am submitting herewith a dissertation written by Tyler S. Smith entitled "Exploring Structural and Electronic Properties of Triangular Adatom Layers on the Silicon Surface Through Adsorbate Doping." I have examined the final electronic copy of this dissertation for form and content and recommend that it be accepted in partial fulfillment of the requirements for the degree of Doctor of Philosophy, with a major in Physics.

Hanno H. Weitering, Major Professor

We have read this dissertation and recommend its acceptance:

Steven S. Johnston, Cristian D. Batista, Gong Gu

Accepted for the Council:

Dixie L. Thompson

Vice Provost and Dean of the Graduate School

(Original signatures are on file with official student records.)

Exploring Structural and Electronic Properties of Triangular Adatom Layers on the Silicon Surface Through Adsorbate Doping

A Dissertation Presented for the

Doctor of Philosophy

Degree

The University of Tennessee, Knoxville

Tyler Scott Smith

August 2020

To my Father

Scott E. Smith

who taught me to never stop looking beyond.

Acknowledgments

I would like to take this opportunity to thank several people who have made my time at the University of Tennessee in Knoxville successful.

First, I would like to sincerely thank Dr. Hanno H. Weitering. I feel incredibly fortunate to have worked with him, as his leadership and support in my research has been invaluable. His knowledge and wisdom in condensed matter physics has inspired me to continually view scientific concepts with a fresh perspective. It is with his mentorship that I have become the scientist that I am today.

Additionally, I would like to thank Dr. Fangfei Ming and Dr. Paul Snijders, both who continuously challenged my knowledge in condensed matter physics. Dr. Ming taught me everything there is to know about Scanning Tunneling Microscopy. He also taught me good experimental practices that I use continually to this day. Dr. Snijders taught me to never stop growing my knowledge. His availability to answer questions and provide valuable discussion was formative to my growth as a student.

I would also like to thank the members of my committee, Dr. Steven Johnston, Dr. Cristian Batista, and Dr. Gong Gu, for their valuable discussions and questions.

I would also like to express my gratitude to all members in the groups of Dr. Weitering, Dr. Norman Mannella, and Dr. Snijders. Foremost, a substantial part of my knowledge in ultra high vacuum practices is due to the mentorship from Dr. Paolo Vilmercati, who taught good experimental practice in combination to providing enlightening discussion. Dr. Vilmercati also repaired the STM used in this work, making nearly all of the results in this work possible. My deep appreciation also goes to Dr. Steven Johnston for his valuable instruction on theoretical QPI calculations. I'd also like to thank my peers for their hard collaborative work and discussions: Dr. Nicholas Sirica, Nathan Traynor, Kaleb McClure,

Shiva Dahal, Xiyou Peng, Dr. Yang Wang, and Michael McConnell. Additionally, I'd like to thank Randal McMillan, whose unparalleled expertise in machining critical parts made the success of this project possible. Finally, I'd like to thank Ortega et al. at the Universidad Autónoma de Madrid for their valuable theoretical work.

Finally, I'd like to thank my father and mother, Scott E. Smith and Pamela D. Smith, for encouraging me to never stop challenging myself, and patiently supporting me throughout my studies. I'd also like to thank my incredible partner, Sarah, for her continual support, encouragement, and love.

Abstract

The analysis of the electronic structure and morphology of 1/3 monolayers (ML) of Sn or Pb on Si(111) and Ge(111) has played an important role in understanding the role of electronic correlations in two dimensions. Specifically, the two-dimensional lattice of partially filled dangling bonds of these so-called α-phases has been an important testbed for studying structural phase transitions and correlated electronic phenomena ever since the discovery of a surface charge density wave in the Pb/Ge(111) system more than two decades ago. With the exception of the novel Sn/Si(111) system, all α-phases undergo a charge ordering transition at low temperature. The uniqueness of this surface has further been observed in modulation hole doping experiments, where we have shown that the Sn/Si(111) system shows clear signs of doped Mott physics. This provides a rare insight into cuprate-like physics in a sp^3-bonded non-oxide system and suggests the possibility of realizing unconventional superconductivity on a conventional semiconductor platform. Indeed, recent measurements on this system reveals that the hole-doped Sn layers on a degenerately doped p-type Si(111) wafer are superconducting with a critical temperature of 4.7 $\pm$ 0.3 K. The triangular lattice symmetry and strong Mott correlations of the Sn-derived dangling bond surface state strongly suggest that the superconductivity may be unconventional and topologically non-trivial. This fascinating result motivates attempts to electron-dope this system using low-dose potassium deposition. Here, we find that potassium induces a charge ordering transition in the Sn sublattice. Temperature dependent studies on this surface reveal the complex interplay between the site location and diffusion of the K adatoms, and the charge ordering transition in the Sn sublattice. As the temperature increases from absolute zero, the K atoms start fluctuating about their equilibrium positions and eventually hop back and forth between neighboring lattice sites. During this process, long-range order is maintained.

At higher temperature the K adatoms begin to diffuse over much longer distance, ultimately leading to a complete melting of the K sublattice. K diffusion induces charge fluctuations between the dangling bonds of the Sn sublattice, and ultimately leads to melting of the charge order of the Sn lattice through a displacive and subsequently an order-disorder transition. In combination with theoretical work, this provides a rare atomically resolved insight into a multistep 2D melting transition.

Further studies are performed on the Pb/Si(111) system, as the true electronic ground state and mechanism behind the charge ordering transition has been controversial due to the still limited number of studies of this surface. A unique growth method is developed to grow larger domains on this surface, which greatly reduces the effects of defects and domain boundaries on the structure and electronic structure of the interface. This allows a comprehensive study of both the electronic and structural properties through quasiparticle interference imaging. To explore the role of spin-orbit coupling for heavy adatoms such as Pb, we introduced magnetic scattering centers (Mn) so as to break time-reversal symmetry in the QPI patterns. Our results provide clear evidence of Rashba-type spin-orbital coupling, although more detailed interpretation awaits further theoretical studies.

Table of Contents

List of Tables

List of Figures

Chapter 1

Introduction and Scope

1.1 Materials Revolution of the 20th Century

Technological advances in semiconductor electronics are largely responsible for the progress made since the materials revolution began in the mid-20th century. Most notably is the invention of the point-contact transistor in 1947 at Bell Laboratories by John Bardeen and Walter Brattain (Bardeen & Brattain, 1948), soon followed by the invention of the junction transistor in 1948 by William Shockley (Shockley, 1951). These revolutionary inventions enabled the construction of computers without the reliance on inefficient vacuum tubes, which at the time consumed a great amount of space and electricity. In fact, these inventions were so revolutionary for the computer era that Shockely, Bardeen, and Brattain were awarded the Nobel Prize in Physics in 1956. This was soon followed by the era of integrated circuits, originally invented by Jack Kilby and Robert Noyce in 1959 (Kilby, 1964; Noyce, 1964). This sparked a plethora of large innovative leaps in computer technologies in the following decades, as more transistors on each individual chip meant larger net computing power. The miniaturization of individual components on integrated circuits has led to a consistent growth of available computing power, originally posited by Gordon Moore in 1965. Moore predicted that the number of components per integrated circuit would double every two years. This concept is often referred to as "Moore's law" and has so far proven to be accurate. Moore's prediction has since been used as a 'goalpost' in the semiconductor industry. This trend over the past 50 years is shown in Figure 1.1. The continual pressure

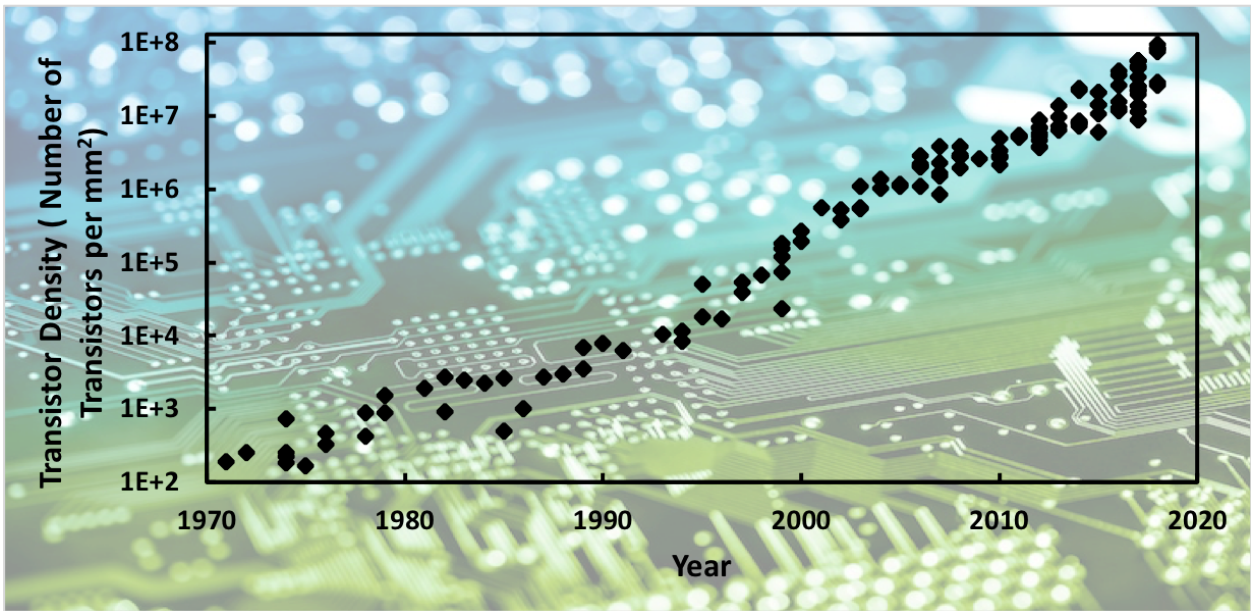

Figure 1.1: Log plot of transistor density for integrated circuits over time, exemplifying Moore's law in action, defined by a doubling every two years. Data taken from Wikipedia (2020).

to continue this trend has led to a multibillion-dollar industry focused on research and development into semiconductor technologies (Tokura *et al.* , 2017).

However, limitations have begun to present themselves in the 'physical scaling' method. At the time of this work, the size of transistors has reached below 10 nm. In this regime, electrons can now quantum tunnel outside of their desired pathway, possibly resulting in short circuiting the chip itself (Keyes, 2005). Additionally, larger densities of transistors produce a considerable amount of heat, motivating the need for new electronic materials with new functionalities involving new physical processes. That is, whereas conventional semiconductor technology is rooted in single electron transport, cooperative phenomena (e.g., magnetism, ferroelectricity, charge and spin density waves, superconductivity) may be exploited in pursuit of novel device functionalities.

Realizations of systems with electronic cooperative phenomena can come in many forms. For instance, one possible option is exploiting magnetic functionalities, involving the use of spin-polarized currents introduced by giant magnetoresistance (GMR) effects (Fert & Van Dau, 2019). This field of study is titled "spintronics", defined as manipulating the

quantum mechanical property of spin to prevent the problem of dissipative heat that plagues conventional charge transport. Research within the field of spintronics has led to the study of spin polarized currents in non-magnetic materials, such as the surface of topological insulators (defined by materials that conduct at the surface but are insulating in the interior) or at Rashba interfaces (due to spin-orbit coupling (SOC) at the interface) (Li *et al.* , 2016; Han *et al.* , 2018).

Other cooperative phenomena in low dimensional systems include unconventional superconductivity, found to exist in two dimensional sheets and fundamentally rooted in electronic correlations (Stewart, 2017). A superconductor is defined by a material that loses all electrical resistance when cooled to a certain temperature. This property opens the unique possibility of constructing devices with superconducting materials that would no longer have the difficulties involving dissipative heat generation that affect current circuit technology, and could possibly provide the technology to engineer qubits for quantum computing (Krantz *et al.* , 2019). Additionally, avenues to realize topological superconductivity using a combination of these behaviors is predicted to be useful for future innovational leaps (Sato & Ando, 2017). Understanding and utilizing such these phenomena could allow us to exploit such collective physics and usher in a new era of computational advancement.

1.2 Cooperative Phenomena on Semiconductor Surfaces

One such avenue for studying collective physics is exploiting Mott physics on semiconducting surfaces. This has not been very successful over the past few decades. Electronic instabilities at these surfaces often lead to a major structural rearrangement, which opens up a band gap and reduces the total electronic energy of the system (Bechstedt, 2012). These electronic instabilities are associated with the presence of partially-filled "dangling bonds", or unsatisfied orbitals associated with the surface adatoms (Figure 1.2(a)). Specifically, an ordered array of half-filled dangling bonds could be a good candidate for creating a two-dimensional narrow-band metal, or a two dimensional Mott insulator, as the lateral orbital

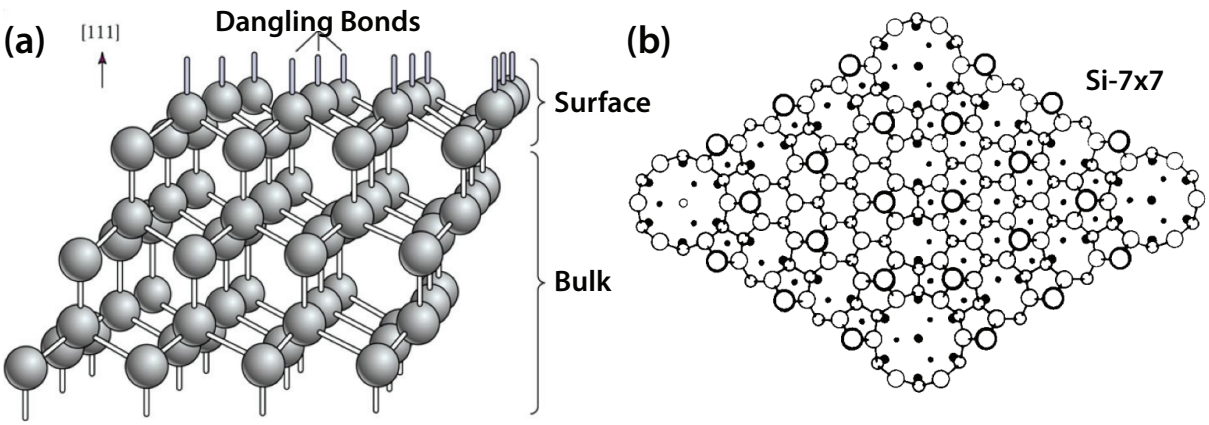

Figure 1.2: (a) An example of dangling bonds on a surface in an atomic model, visualized as exposed sticks above the surface. (b) A top view of the Si(111)-(7x7) surface. This is an extreme case of an atomic restructuring, where the number of dangling bonds is reduced from 49 to 19 (Takayanagi *et al.* , 1985).

overlap is small (Weitering *et al.* , 1997a; Ortega *et al.* , 2002; Profeta & Tosatti, 2007). However, atomic restructuring typically converts these partially filled dangling bond orbitals into fully occupied and fully depleted dangling bonds. Alternatively, they may be eliminated altogether by forming new bonds with neighboring atoms. An example of this is given in Figure 1.2(b) for the Si(111) surface, where the stable surface adopts a (7×7) supercell. Here, the number of dangling bonds is reduced by a ratio 19/49 as compared to the (1×1) truncated surface (Takayanagi *et al.* , 1985).

A select few systems do not undergo a major restructuring and represent good candidates for exploring the possibility of two-dimensional Mott physics. One possible realization of this scenario are the Group IV adsorbates (e.g., Sn or Pb) on (111) surfaces of Si or Ge. These so-called α-phases consist of a $(\sqrt{3} \times \sqrt{3})$ array of group IV adatoms with partially filled dangling bond orbitals (Figure 1.3) (Carpinelli *et al.* , 1996, 1997; Weitering *et al.* , 1997a; Petersen *et al.* , 2002). The large separation between the dangling bond orbitals (6.65Å) leads to small band widths and, consequently, correlations become important. These properties have proved to be a rich testbed for the study of electronic correlations.

In this dissertation, we will focus on the Sn and Pb-induced $(\sqrt{3} \times \sqrt{3})$ reconstructions on Si(111). Specifically, these are composed of 1/3 ML of Sn and Pb adsorbed on the Si(111)

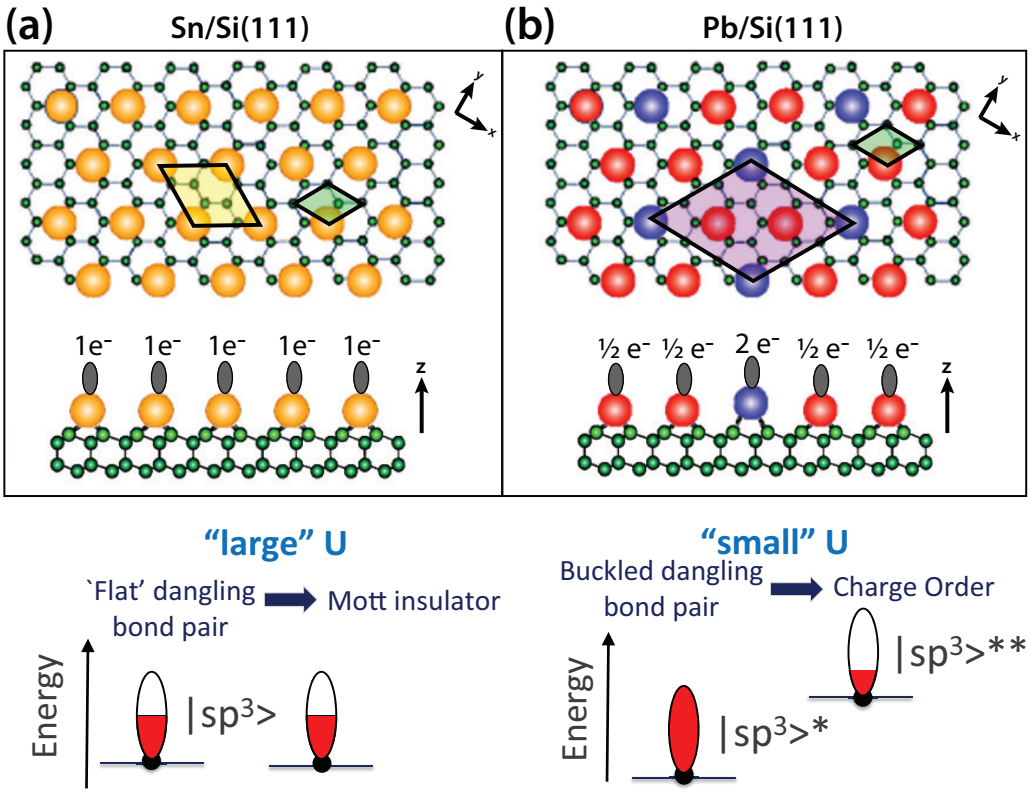

Figure 1.3: Schematic of the 1/3 ML reconstructed Sn (a) and Pb (b) surfaces on Si(111). The larger energy cost for double occupancy (defined by the energy cost U) prevents a redistribution of electronic charge over the Sn dangling bonds, whereas a smaller energy cost for the Pb case leads to a lower energy by redistributing the charge over the dangling bonds. The different filling between the dangling bonds then leads to orbital rehybridization and buckling of the Pb layer as the sp^3 orbitals are modified. The **x**, **y**, and **z** directions are $[01\bar{1}]$, $[\bar{2}11]$, and [111], respectively.

substrate. A schematic of these two surfaces is given in Figure 1.3. The Sn/Si(111) system is claimed to be a triangular lattice, spin 1/2 antiferromagnetic Mott insulator (Profeta & Tosatti, 2007; Li *et al.* , 2013; Ming *et al.* , 2017). The Pb system, on the other hand, is a correlated (3×3) charge ordered metal (Brihuega *et al.* , 2005; Tresca *et al.* , 2018).

For the Sn case, the Mott insulating phase is defined by strong on-site Coulomb repulsion, strong enough to cause localization of electrons on the Sn dangling bonds. Hole doping produces a metallic phase at low temperature (Ming *et al.* , 2017). We recently found that hole doping levels of the order of 10% produces a superconducting surface at low temperature (Wu *et al.* , 2019). This is consistent with other Mott insulating materials that exemplify a

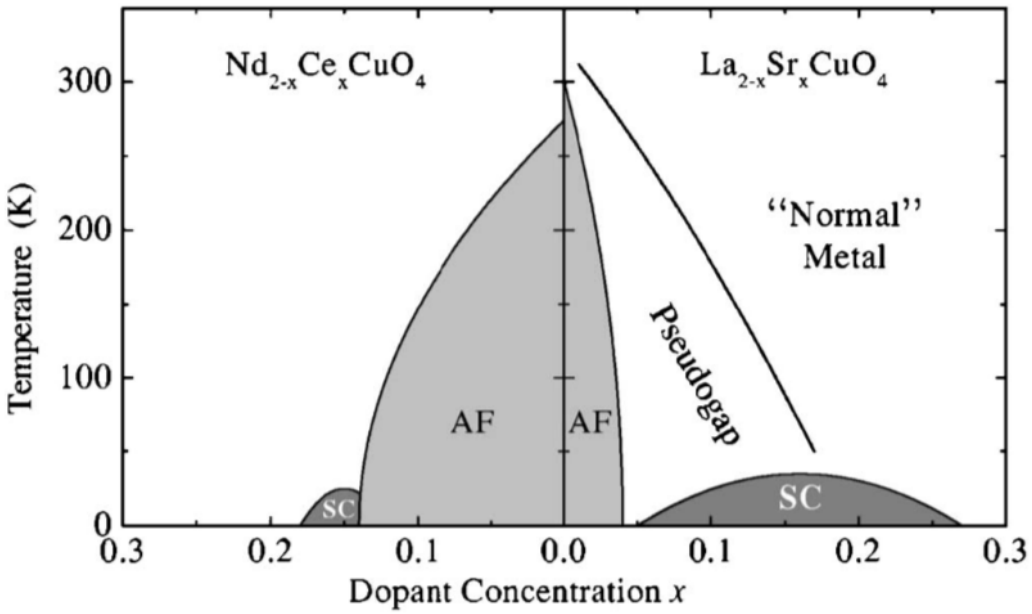

Figure 1.4: Doping dependent phase diagram of the cuprates for both electron and hole doping. The antiferromagnetic host compound ($x = 0$) ultimately becomes superconducting upon doping (SC) followed by becoming a normal metal upon overdosing. Taken from Damascelli *et al.* (2003)

variety of competing phases that can occur upon electron addition or removal. For example, in the case of the cuprates, the undoped case exemplifies an antiferromagnetic ground state (Lee *et al.* , 2006). Upon doping this becomes superconducting, followed by a normal metallic ground state found upon further doping in what is called the 'overdoped' regime (see Figure 1.4). This motivates further doping attempts to fully flesh out the doping-dependent ground states of the Sn and Pb systems.

Hole doping of the Sn/Si(111) interfaces was realized by adding boron dopants to the substrate. This, however, has its limitations as we were not able to increase the doping levels beyond 10%. In this thesis we explore an alternative approach by depositing electron and hole dopants on the surface. This is called adsorbate doping. Ideally, it is not desirable to place a dopant in the surface layer itself, as this can introduce further disorder and modify the chemistry of the surface. It is therefore very important to understand the precise role of the adsorbate species.

Our work is primarily motivated by the questions: "Is it possible to further hole dope the Sn/Si(111) and increase its superconducting T_c by adsorbing electron-accepting molecules?", and "how does this surface behave under electron doping?" This work attempts to answer these using adsorbate doping methods with organic acceptor molecules or alkali adatoms. In the latter case, the alkali-decorated Sn surface is observed to undergo a charge ordering transition (defined as a structural change due to the rearrangement of electrons in the Sn dangling bonds) (Tosatti *et al.* , 1995; Smith *et al.* , 2020). This finding raises additional questions: "What is the lattice location of the alkali adatom and what is its bonding configuration?"; "What is the influence the alkali adatom dynamics on the charge ordering of the Sn host lattice?"; "What role do the alkali atoms play in the charge ordering transition?"; "What does two-dimensional sublattice melting look like when atomic resolution is possible?"; "Is 2D sublattice melting a first order phase transition or does it have topological features (Kosterlitz & Thouless, 1973; Halperin & Nelson, 1978; Young, 1979)?"

In contrast to the Mott-insulating nature of Sn on Si(111), Pb on Si(111) is a correlated charge ordered metal (Tresca *et al.* , 2018; Adler *et al.* , 2019). Though isoelectronic with Sn, the heavier Pb surface will be subject to relativistic effects, spin orbit coupling, and a different Pb-Si interaction. The charge ordered phase is defined by a structural buckling at low temperature, leading to a symmetry broken ground-state. This is likely due to the smaller Coulomb repulsion in the Pb dangling bonds that allows for double occupancy, thus enabling a lowering of the total energy via a small lattice distortion. However, this system has so far been minimally studied, leading many questions open for debate: "What is the structural and electronic ground state of the system?"; "How does this surface behave under doping?"; "How can we corroborate the existence of spin-split surface state bands?".

The scientific tool that possesses superior capability to probe both electronic and structural properties of these systems is Scanning Tunneling Microscopy (STM). This allows *in situ* measurements on the above surfaces and is the only technique that can measure these properties on such a nanoscopic level. The full utility of STM includes atomic resolution imaging and voltage-current spectroscopy to extract the local density of states. Additionally, X-ray Photoelectron Spectroscopy (XPS) is used for chemical composition and electronic

structure; Angle Resolved Photoemission Spectroscopy (ARPES) is used to measure the electronic structure in momentum space; and Low Energy Electron Diffraction (LEED) is used to measure the surface periodicity. These techniques are used in tandem with the STM measurements. In some cases, the experimental output from these methods will be compared with collaborative theoretical work. This dissertation will attempt to address some of the questions above using this scheme.

1.3 Overview of thesis

Chapter 2 contains an overview of the ultra-high vacuum experimental apparatus used for growth and characterization of the samples. Next, we provide a theoretical description of STM and related methodologies, including a brief overview of Quasiparticle Interference Imaging. The chapter concludes with a brief description of the LEED and ARPES experiments.

Chapter 3 provides the experimental and theoretical background of the potassium decorated Sn/Si(111) surface, starting with a description of the Sn/Si(111) parent phase. It begins by describing the results of a collaborative work on modulation doping the Mott insulating parent phase. This description ends with a brief explanation of recent findings of superconductivity at low temperature for the doped surface that this author was involved in. These findings motivated the main body of this chapter (also published in Smith *et al.* (2020)), which centers around surface doping experiments using alkali adsorbates as electron donors. Here we find that the deposition of 1/6 ML of potassium results in a novel charge-ordered phase with three distinct atomic sublattices: triangular (Sn), honeycomb (K), and Kagome (Sn). After elucidating the structure and electronic properties of the charge-ordered ground state, we investigate the temperature evolution of these properties and show that K-atom diffusion is accompanied by charge fluctuations in the Sn sublattices, which ultimately results in the formation of a molten K sublattice and a step wise melting of the charge order in the Sn lattice. For the interpretation of the experimental findings, we enjoyed strong theory support by the group of Prof. Jose Ortega at the Autonomous University of Madrid.

After completing these studies, we took a closer look at the surface state band structure using ARPES. The filled-state spectra should reveal the electronic structure of the Kagome sublattice, which is expected to exhibit two dispersive bands with Dirac like band crossings and a third surface-state band that is extremely flat. Only very few Kagome systems have been elucidated via ARPES, and those systems typically are 3D crystals with layered structural features. Indeed, this might be the first case of a strictly 2D atomic Kagome sublattice. In this study, we identified multiple surface state bands that appear mostly consistent with the calculated DFT band dispersion for K/Sn/Si(111). The full dispersion cannot be resolved, however, because the bands are very close in energy and cannot be properly distinguished throughout the surface Brillouin zone.

Finally, we include a preliminary study of the closely related K/Pb/Si(111) system. Interestingly, this surface behaves in an identical fashion to the K/Sn/Si(111) system, showing three distinct sublattices at various STM tunneling biases. However, the surface state bands are shifted by ∼300 meV, indicative of a self-doping effect. This motivates possible future work into depositing alkalis onto other surfaces within the α-phase family.

Chapter 4 contains the growth and characterization of the Pb/Si(111) surface, beginning with the theoretical and experimental background of the system. The growth procedure and optimization is then described, with initial evidence consistent with a *1 up 2 down* buckling reconstruction or (3×3) charge ordered ground state. We attempted to hole dope this charge ordered phase using a variety of silicon substrates with different doping levels. This was not very successful as hole doping appeared to destabilize the α-phase relative to the neighboring $(\sqrt{7}\times\sqrt{3})$ phase. We then move to the Quasiparticle Interference Imaging on the undoped surface, from which the primary scattering vectors are extracted. This allows the electronic dispersion of the ground state to be compared with recently published theoretical work for this system (Tresca *et al.* , 2018). It is shown that the data is in good agreement with the model for a *1 up 2 down* ground state. Additionally, work using manganese adatoms as magnetic impurities for additional Quasiparticle Interference Imaging reveals new scattering features, providing evidence for a possible spin-split ground state on this surface.

Chapter 5 shows results from adatom deposition experiments on the Sn/Si(111) surface using a molecular dopant. Specifically, F4-TCNQ molecules were deposited. This is

motivated by the literature claiming that these molecules are extreme electron acceptors (Kumar *et al.* , 2017). Unfortunately, the molecules are found to have little effect on the surface, motivating further attempts using other species in order to achieve hole doping.

Finally, Chapter 6 summarizes the main conclusions from Chapters 3, 4, and 5, including an outlook for possible future experimentation motivated by the findings given in this work. In summary, in this thesis we explore the feasibility of doping two-dimensional surface systems with mixed success. From these findings we anticipate a future work in surface physics that might be of interest, such as surfactant doping or growth of Si(111) surfaces with higher doping levels, potassium decoration of Sn/Ge(111) and Pb/Ge(111) surfaces, or the use of Mn as a magnetic scatterer in other magnetic materials.

Chapter 2

Experimental Methods

2.1 The Ultra High Vacuum Apparatus

All of the experiments in this work are performed inside ultra-high vacuum (UHV) systems. Such an environment is necessary for keeping sample surfaces atomically clean, and to prepare atomically thin film materials without incorporating unwanted impurities originating from residual gases in the chamber. This removes uncertainties regarding the role of contaminants from the picture, and a high degree of confidence can be taken in the composition of the grown and measured samples. A cleaner environment also ensures a greater lifetime of the samples after the growth.

Different stages of growth and characterization were performed in two separate UHV chambers. The first (called "Growth and XPS chamber") was used in the preliminary growth and morphology study of the Pb/Si(111) system (See Section 4.2), and is equipped with an XPS, LEED, variable temperature STM (VT-STM), and an effusion cell for Pb deposition. In addition, the system is equipped with a sample manipulator for precise sample positioning, with capabilities for direct current heating of Si substrates for sample preparation and thin film growth. A schematic of this chamber is shown in Figure 2.1a.

Most of the data shown here were obtained in the more recently coupled system (titled "Coupled LT-STM/ARPES chamber"). A schematic of this chamber is shown in Figure 2.1b. This apparatus is composed of a low-temperature STM (LT-STM), metal MBE chamber

(equipped with a effusion cell for Sn deposition), oxide MBE chamber (not shown), ARPES, and an intermediate "Prep" chamber for further sample preparation.

2.2 Epitaxial growth in Ultra High Vacuum

Molecular beam epitaxy (MBE), rooted in ultrahigh vacuum evaporation, is the most sophisticated technique for the high-quality epitaxial growth of thin films and atomically abrupt crystalline interfaces. This is rooted in the precise control of beam fluxes and growth conditions, resulting in the utmost control of thickness and composition.

The surfaces in this work require a highly constant evaporation rate of about one monolayer per minute (ML/min), allowing epitaxial (i.e. layer-by-layer) growth. The most stable type of deposition source is the effusion cell (also called K-cell, named for physicist Martin Knudsen (Knudsen, 1934)). These cells use the concept of sublimation and effusion to precisely control the trajectory and rate of the deposited source material. Figure 2.2 shows a basic schematic of an effusion cell. The source material is placed inside a crucible (Pyrolitic Boron Nitride (PBN) and Alumina (Al_2O_3) crucibles are used in this work), which is then surrounded by a filament heater and radiation shielding. A pinhole aperture is placed above the crucible to control the cone of emission, in addition to a shutter for precisely beginning and ending the deposition. The effusion cells are also equipped with a thermocouple, mounted close to the crucible location, which is connected to a temperature control unit (typically using a PID feedback system) that regulates the output power to the heating filament. Effusion cells used for higher temperature applications are equipped with a water-cooling serpentine to reduce transmitted heat and degassing of the cell.

For several of the surfaces used in this work, the source material is required to be adsorbed onto a cold surface ($\sim$77 K). This necessitates a custom effusion cell configuration and geometry to avoid radiative sample warming, as the sample is temporarily taken out of contact with the cold cryostat using a "wobble stick" and placed above the effusion cell for thin film deposition. Figure 2.3 shows a drawing and final configuration of the custom effusion cell with radiation shield removed. This unique effusion cell was designed and fabricated by the author for the specific goals laid out for the experiments in this work.

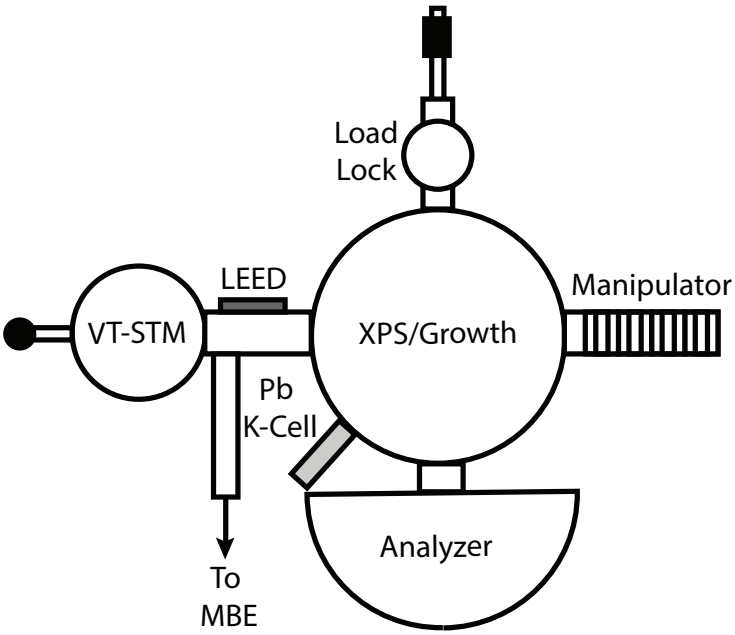

(a)

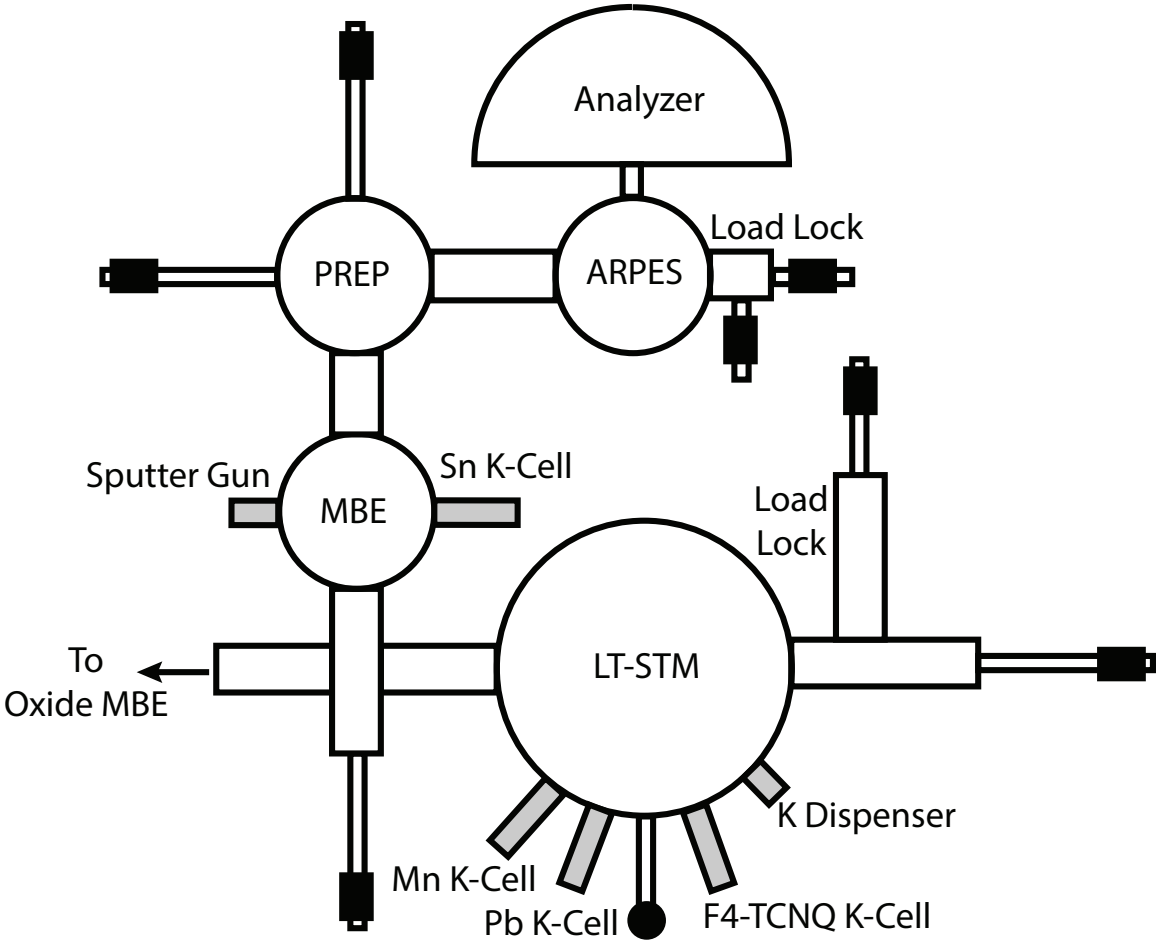

(b)

Figure 2.1: (a) Growth and XPS chamber (b) Coupled LT-STM/ARPES chamber

Figure 2.2: left: A schematic diagram of the effusion cell head. right: A SciCam low-temperature effusion cell used for Pb deposition in this work. (Oura *et al.* , 2010)

Other sources for sample growth include metal dispensers that allow clean deposition of alkali metals by combining a clean getter source (or reducing agent) with a stable salt (an alkali-metal chromate). This is necessary due to their high vapor pressure and reactivity of the alkalis to water. Briefly, the getter component of the dispenser is composed of a coating made of a reactive material that surrounds the alkali chromate material. By applying an electrical current, a reduction reaction occurs, and the getter material is able to adsorb nearly all of the chemically active gases that are produced. This provides a very clean alkali metal vapor. The dispensers used in this thesis are purchased from the SAES group.

The MBE methods described in this section are necessary for precise control of sample growth parameters. These processes commonly result in a surface reconstruction, where the surface overlayer rearranges into a different atomic configuration than the bulk. Optimizing the surface coverage and morphology by exploring the phase space made up of deposition time, rate, annealing temperature, and annealing time is a critical step for all surfaces in this work.

2.3 Characterization Techniques

2.3.1 Scanning Tunneling Microscopy and Spectroscopy

Experimental study of materials in the nanoscopic scale was revolutionized by the Nobel prize winning invention of the scanning tunneling microscope (STM) in 1981 by Gerd Binnig and

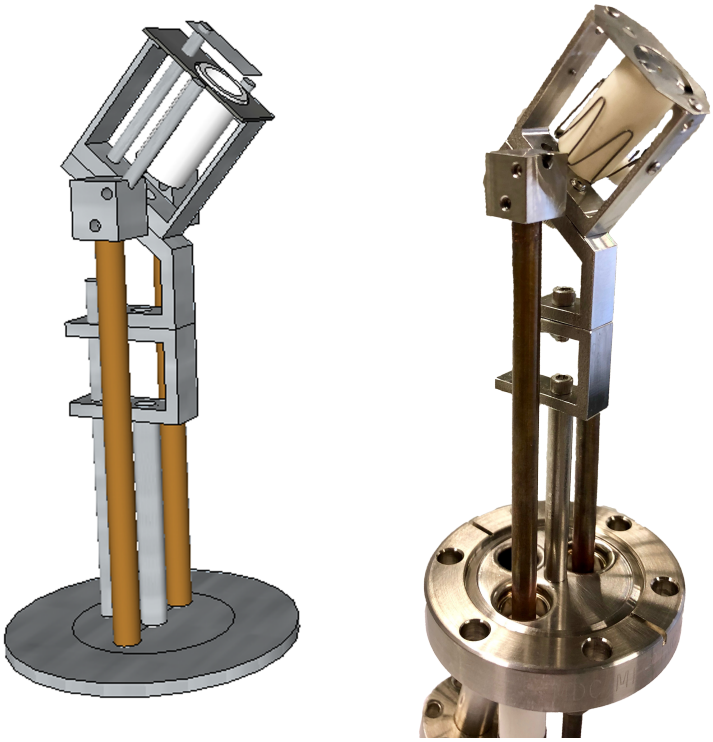

Figure 2.3: left: A drawing of a custom effusion cell designed for deposition onto a sample close to the cold LT-STM location. right: Final configuration of the custom effusion cell with radiation shield and shutter removed.

Heinrich Rohrer (Binnig & Rohrer, 1982). This technique was the first that could resolve the electronic structure at an atomic scale on practically any conducting surface, which naturally led to the means to map the spatial atomic structure.

The fundamental principle of the STM is based on electron tunneling. More specifically, the STM is composed of an atomically sharp metallic wire (typically W or PtIr), brought into the proximity of the sample to be measured. This causes the wavefunctions of the tip and sample to overlap, allowing electrons to tunnel through the vacuum barrier between the tip and sample. A simplified schematic of this is shown in Figure 2.4(a). Different potential biases applied between the tip and sample allow the full study of the sample electronic structure, as the tunneling current is strongly dependent on the wavefunction overlap and density of states.

The same concept can be applied to obtain STM topography images by moving the tip across the sample. Typically, these images are obtained in constant current mode, where a

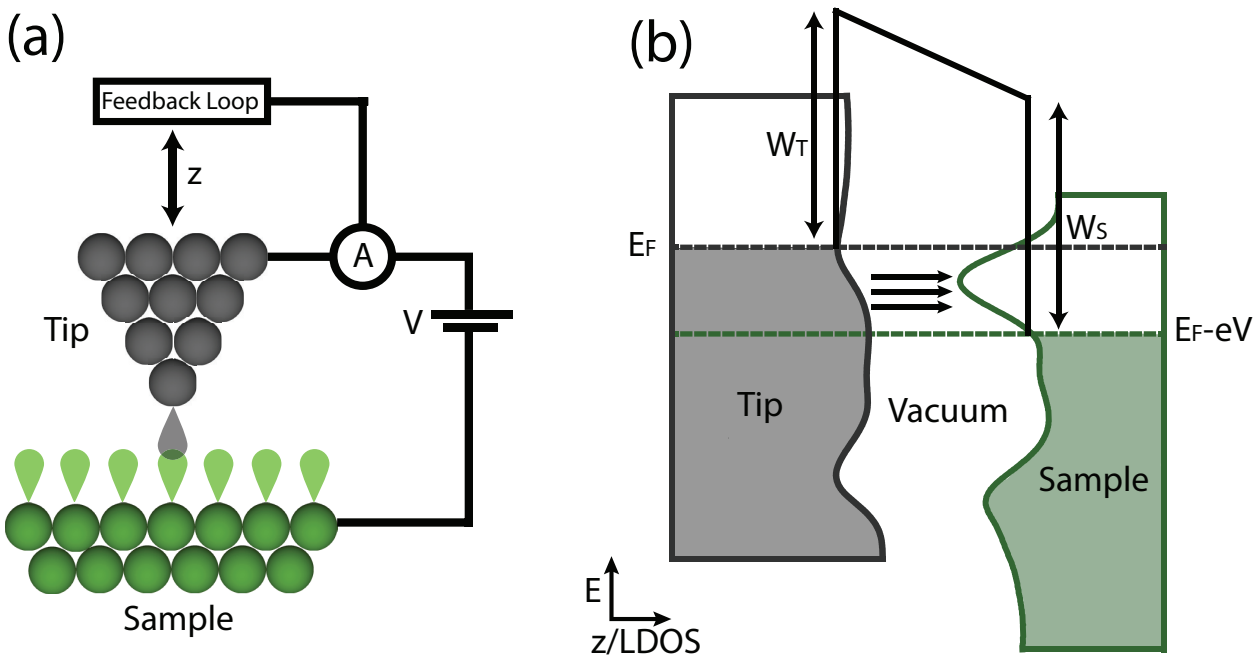

Figure 2.4: (a) Schematic of the operation of the Scanning Tunneling Microscope in constant current mode, where the tip height (z) is made variable using a feedback loop operation. (b) Diagram of the energy levels in the case of a positive bias applied to the sample (right). This allows electronic tunneling into the sample, accessing the unoccupied states. The rippling of the areas between the tip and sample are used to visualize LDOS variations in the tip and sample. Tunneling into the occupied states (not shown) is simply a matter of reversing the sample polarity.

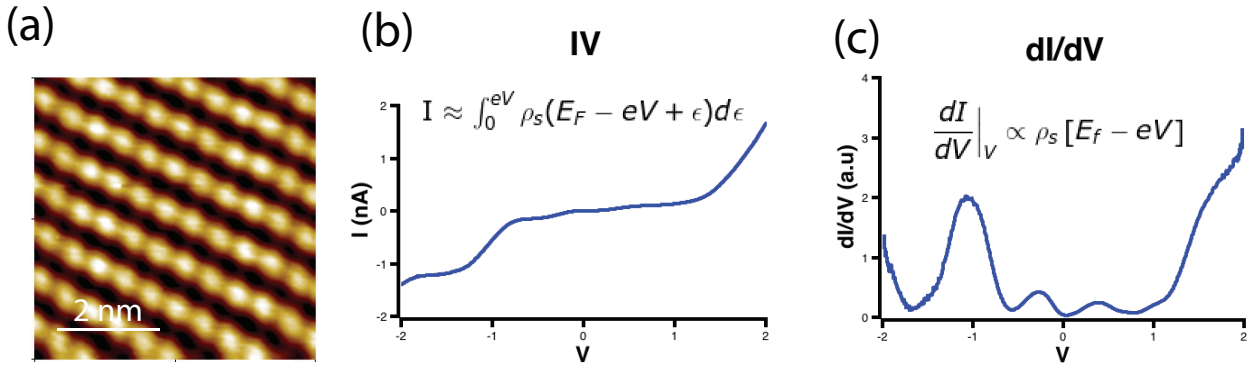

Figure 2.5: (a) A STM topography image taken in constant current mode. An I/V curve is then taken by disabling the feedback loop, sweeping the bias, and measuring the current (b). This is reproduced several times, allowing high data statistics. The resulting I/V curve is then differentiated, which is proportional to the LDOS (c).

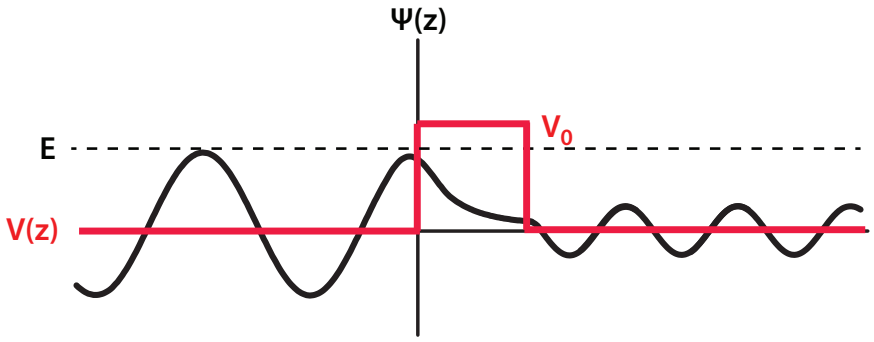

Figure 2.6: Illustration of a simple one-dimensional potential barrier exemplifying basic electron tunneling through a barrier. Here, the wave function is sinusoidal before the barrier and and is exponentially decaying within the barrier, with a reduced amplitude after.

feedback system is implemented. In this mode, the surface morphology is given by the tip height. An example of a STM topography image taken in constant current mode is given in Figure 2.5(a). This is made possible by precise control of piezoelectric ceramics, allowing sub-angstrom resolution in all three dimensions.

The fundamentals of electron tunneling can first be envisaged in a simple one-dimensional model (Griffiths, 2017). Figure 2.6 contains a schematic of this simple case. Consider the case of an electron tunneling through a finite barrier of width d

$$V(z) = \begin{cases} V_0 & d > z > 0 \\ 0 & \text{otherwise} \end{cases}.$$

Where the potential barrier given by V_0 is the region between the tip and sample (within this simplified model, no bias is applied between sample and tip, and the potential barrier is simply the work function W_T, or the height of the vacuum barrier). By solving the Schrödinger equation for the wavefunction inside the tunneling region, the original wavefunction from the tip $\psi(0)$ decays exponentially as:

$$\psi(z) = \psi(0)e^{-\kappa z}.$$

The decay constant is given by:

$$\kappa = \frac{\sqrt{2m(V_0 - E)}}{\hbar},$$

where E is the initial energy, m the electron mass, and $\hbar$ is the reduced Planck constant. From this simple toy model we can understand a variety of fundamental tunneling concepts between the tip and sample. The inverse of the decay constant κ^{-1} can be interpreted as the lengthscale of the tunneling. In this case, this is on the order of an angstrom. In addition, the tunneling probability is approximately the square of the wavefunction in a barrier of width d :

$$P(d) = |\psi(d)|^2 = |\psi(0)|^2 \, e^{-2\kappa d}.$$

This reinforces why the STM tip must be within angstroms of the surface in order to obtain proper tunneling conditions.

We can now formally describe the tunneling process in STM. Using the so named "Bardeen approach" to tunneling theory, the tunneling current is evaluated through the overlap of the wavefunctions of the two systems using Fermi's Golden Rule (Bardeen, 1961; Chen, 2008)

$$W_{\mu\nu} = \frac{2\pi}{\hbar} \left| M_{\mu\nu} \right|^2 \delta \left(E_\mu^S - E_\nu^T \right).$$

Here, $W_{\mu\nu}$ is the rate of tunneling from the initial state ψ_u^S of the sample to the final state ψ_ν^T of the tip with energies E_μ^S and E_ν^T, respectively. $M_{\mu\nu}$ is the tunneling matrix element, which is defined by the integral over a surface S in the barrier region lying between the tip and the sample

$$M = \frac{\hbar}{2m} \int_{z=z_0} (\Psi_\nu^* \frac{\delta \Psi_\mu}{\delta z} - \Psi_\mu \frac{\delta \Psi_\nu^*}{\delta z}) dS.$$

The tunneling matrix element when applied for the simple potential barrier above returns the same exponential dependence derived for the simplified case at the beginning of this section. The delta function implies that tunneling between states can only happen if the energy levels on both sides of the junction line up ("elastic tunneling"). In reality the tip and substrate contain a continuous spectrum of states, so the full sum of the final and initial states for all spin channels must be considered. Additionally, these experiments are performed at non-zero temperature, which creates a thermal distribution of electrons over the accessible energy

levels. The occupation probability of these levels is given by the Fermi-Dirac distribution

$$f(E - E_F) = \frac{1}{1 + \exp(E - \mu)/k_B T}.$$

The first step is to use Fermi's Golden Rule to derive both the tunneling current from tip to sample and vice versa, proportional to $eW_{\mu\nu}$, where e is the electron charge. Assuming a bias voltage V, this is given by

$$I(V)_{S\to T} = \frac{4\pi e}{\hbar} \sum_{\mu\nu} f(E_\mu^S - E_F^S)[1 - f(E_\nu^T - E_F^T)] \left|M_{\mu\nu}\right|^2 \delta(E_\nu^T - E_\mu^S - eV)$$

$$I(V)_{T\to S} = \frac{4\pi e}{\hbar} \sum_{\mu\nu} f(E_\mu^T - E_F^T)[1 - f(E_\nu^S - E_F^S)] \left|M_{\mu\nu}\right|^2 \delta(E_\nu^T - E_\mu^S - eV).$$

Here, a factor of 2 has been inserted in order to account for the two spin states of an electron. Then, the total tunneling current is simply given by the difference between the two

$$I(V) = \frac{4\pi e}{\hbar} \sum_{\mu\nu} [f(E_\mu^S - E_F^S) - f(E_\nu^T - E_F^T)] \left|M_{\mu\nu}\right|^2 \delta(E_\nu^T - E_\mu^S - eV).$$

The final step is to change from a summation over discrete states into an integral of the energies using the density of states by employing the familiar expression $\sum_\mu \to \int \rho(E) dE$. Following this conversion and a change of variable for simplification of the integrand, the total current is given by (Figure 2.4(b)) (Tersoff & Hamann, 1983, 1985)

$$I(V) = \frac{4\pi e}{\hbar} \int \left[f(E_F^T - eV + \epsilon) - f(E_F^S + \epsilon)\right] \times \rho_S(E_F^S - eV + \epsilon)\rho_T(E_F^T + \epsilon) \left|M\right|^2 d\epsilon.$$

Here, V is the bias voltage between the tip and sample and ρ_S and ρ_T are the density of states of the sample and tip (respectively). Two approximations can now be made: At finite T the Fermi distribution function can be taken as a step function, with the criteria that $k_B T$ be smaller than the energy resolution required in the experiment (for example, at liquid Nitrogen temperatures of 77K, $k_B T = 6.6$ meV, and at liquid Helium temperatures of 4 K $k_B T = .34$ meV). In addition, the tunneling matrix element is conventionally assumed to have a negligible effect on the tunneling current in relation to the density of states factor

(though there are many cases where this must be taken into account) (Bardeen, 1961). With these approximations the tunneling current is now of the form

$$I(V) = \frac{4\pi e}{\hbar} |M|^2 \int_0^{eV} \rho_S(E_F^S - eV + \epsilon)\rho_T(E_F^T + \epsilon)d\epsilon.$$

The change in integration boundaries is due to the approximation of the Fermi distribution as a step function. From this form of the tunneling current, a powerful observation can be made. If the density of states of the tip is known, the true density of states of the surface can be extracted. Typical preparation for a STM study involves ensuring that the tip is metallic, i.e. a flat density of states over the energy region of interest near E_F. In this case, ρ_T above no longer depends on energy, and the tunneling current becomes

$$I(V) \approx \int_0^{eV} \rho_s(E_F^S - eV + \epsilon)d\epsilon.$$

This leads to the relation between the tunneling current and local density of states (LDOS) of (note that this expression is approximate as the factor not dependent upon bias has been dropped)

$$\frac{dI}{dV} \propto \rho_s \left[E_F^S - eV\right].$$

This is the fundamental expression most commonly used to explain scanning tunneling microscopy (STS).

Experimentally, STS is performed by holding the tip-sample distance constant and sweeping the tip-sample bias, while the feedback loop of the STM is disabled. The LDOS can be obtained in two distinct ways. In the first, the tunneling current is measured as the bias is varied. In order to obtain a high signal-to-noise ratio, this is reproduced several times. The I/V data is then averaged and differentiated (see Figure 2.5(b,c)). The second uses a standard lock-in method by applying a small voltage oscillation excitation of $V(t) \approx \cos(\omega t)dV$ and measuring the response dI at a fixed frequency ω. This method is powerful as it directly measures the $\frac{dI}{dV}$ signal, with the caveat of requiring incredibly stable tunneling conditions, which is not always possible due to thermal drift and ceramic creep. Data using both of these methods will be used throughout the body of this work.

The ability of the STM tip to move across the sample can also be used in combination with the acquisition of local spectroscopic information. This mode, titled differential conductance imaging, allows full mapping of the LDOS at a specific energy, acquired as a function of the tip position. The process is as follows: A normal constant current image is acquired on a (x, y) grid. After each pixel is acquired, the STM tip pauses its motion, the feedback loop is turned off, and $\frac{dI}{dV}\Big|_V$ is measured using the lock-in amplifier method described above. Using this procedure at various energies can answer valuable questions about the local electronic structure.

2.3.2 Quasiparticle Interference Imaging

A powerful extension of differential conductance imaging evolved from the observation of standing waves in the experimental data, now called Quasiparticle Interference Imaging (QPI) (otherwise known as Fourier Transform $\frac{dI}{dV}$ mapping) (Hasegawa & Avouris, 1993; Crommie *et al.* , 1993; Petersen *et al.* , 2000). In summary, QPI is used to image standing waves in the electronic density, created by quasiparticles scattering off inhomogeneities on the surface of a crystal, such as defects or step edges. These standing waves in the presence of impurities are known as Friedel oscillations (Friedel, 1958). In fact, filled state dI/dV images at low bias are visualizations of energy resolved Friedel oscillations. The wave vectors of these oscillations depend strongly on the constant energy contour momentum of the electrons at the tunneling energy eV.

More formally (adapted from the explanation in (Petersen *et al.* , 2000)), in a single-particle picture, the electrons in a perfect crystal are Bloch waves $\psi_k(\mathbf{r}) = e^{i\mathbf{k}\cdot\mathbf{r}} u_{\mathbf{k}}(\mathbf{r})$, where u is a periodic function that has the same periodicity as the crystal. In this case, the modulations in the LDOS, given by

$$\mathrm{LDOS}(\mathbf{r}, E) = \sum_{\mathbf{k}} |\psi_{\mathbf{k}}(\mathbf{r})|^2 \, \delta(E - E_{\mathbf{k}})$$

will simply follow the periodicity of the crystal. However, upon the introduction of impurities into the system, the translational symmetry of the system is then broken, and the Bloch states elastically scatter from defects and interfere with one another. This leads to standing

waves created from a linear combination of the Bloch states of the form

$$|\psi_q(\mathbf{r})|^2 = |c_i\,\psi_{k_i}(\mathbf{r})|^2 + \left|c_f\,\psi_{k_f}(\mathbf{r})\right|^2$$

Therefore, the new wavefunctions will appear in the LDOS as interference waves with the wavevector between the initial and final state of the scattering process $\mathbf{q} = \boldsymbol{k}_i - \boldsymbol{k}_f$. The final eigenstates at energy E can be composed of all other states on the constant contour of energy in the electron dispersion $\epsilon_{\mathbf{k}}$. Then the Fourier transformed $\frac{dI}{dV}$ images $g(\mathbf{q}, V)$ can be considered as the autocorrelation of the constant energy contours. With some knowledge of the $\mathbf{k}$ dispersion of the system (from other techniques such as ARPES or theory), the $\mathbf{q}$ dispersion in $g(\mathbf{q}, V)$ images can be used to extract the constant energy contours and dispersion of the system in $\mathbf{k}$ space. For example, in the simplest of cases, the 2D free electron gas (2DEG) with a circular Fermi surface can be considered. Then, the dI/dV map at zero bias will simply correspond to scattering vectors between the Fermi momenta on each side of the Fermi surface, so the only component of the power spectrum will be a circle of radius $\mathbf{q} = 2\mathbf{k}_f$ (if measured with near zero bias). This is due to backscattering being the dominant effect from areas of large density of states in the constant energy contour. This is very nicely observed in Ag(111) (Grothe *et al.* , 2013) and Cu(111) (Petersen *et al.*

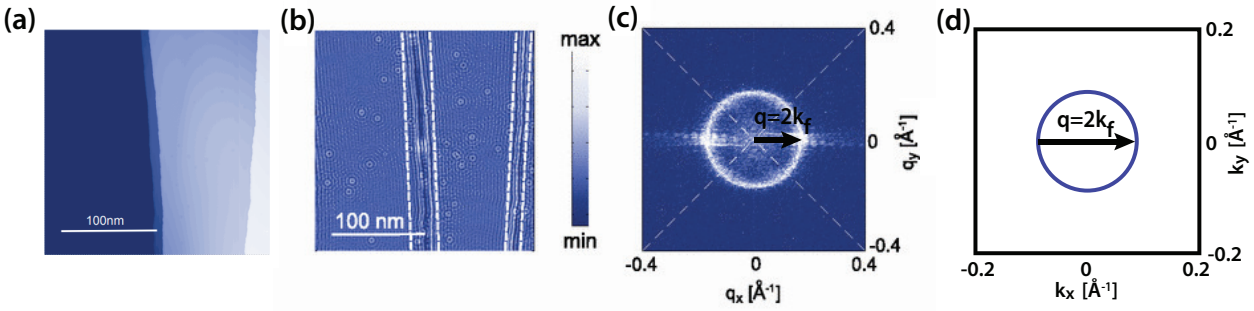

Figure 2.7: (a) 239 x 239 nm^2 topography and (b) dI/dV image of the Ag(111) surface obtained at V = -100 mV, T = 4.2 K. The oscillations of the LDOS due to the point defects are seen as Friedel like oscillations away from the step edges and CO adsorbates. (c) Fourier transform of the conductance map in (b), showing a circle with radius $q = 2k_f$. (d) Schematic of the Fermi surface contour. All images taken from Grothe *et al.* (2013).

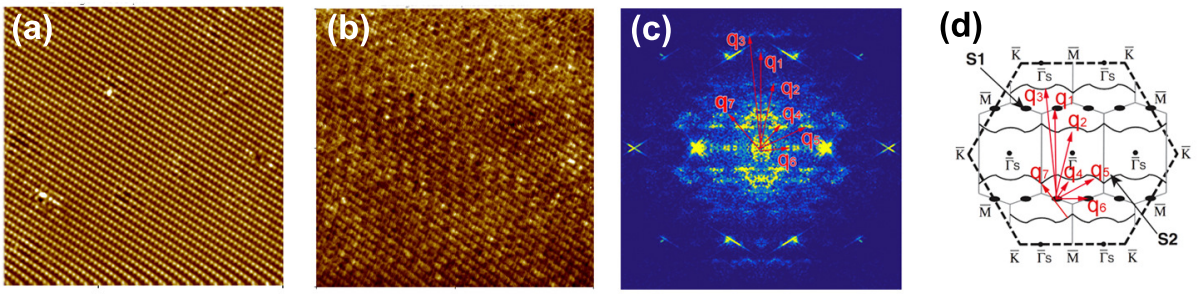

Figure 2.8: (a) 30x30 nm^2 STM topographic image. (b) Simultaneously acquired differential conductance map $g(\mathbf{r}, V)$ taken at a bias voltage $V = +5$ mV at 4.4 K. (c) Fourier transform $g(\mathbf{q}, V)$ of the conductance map in (b), with superimposed q-vectors. (d) Single domain DFT calculation with corresponding q-vectors of the Fourier transform in (d). Calculation of constant energy contours taken from (Kim *et al.* , 2010)

, 1998). This former case is given in Figure 2.7. Typically, the surface topography and $\frac{dI}{dV}$ images are taken simultaneously. The Fourier transform $g(\mathbf{q}, V)$ is then taken, which is directly compared to the theoretical Fermi surface. Of course, this can be very complex for nontrivial Fermi surfaces. Such a complicated system with multiple $\mathbf{q}$ scattering vectors is given in Figure 2.8.

It is important to note that in the presence of spin polarization the surface states will have forbidden backscattering channels, and states with different spin symmetries will not interfere with each other. However, it has been shown that introducing magnetic impurities into the system can allow spin-flip scattering by breaking the time reversal symmetry(Yoshizawa *et al.* , 2015; Okada *et al.* , 2011). Comparing different scattering channels in the QPI patterns from systems with and without magnetic scatterers can elucidate the true spin structure of the surface bands. This technique will be used in the case of the Pb/Si(111) system using magnetic Mn defects.

2.3.3 Low Energy Electron Diffraction

Low Energy Electron Diffraction (LEED) uses low energy electrons scattered elastically from a crystal to obtain the reciprocal lattice. The typical energy of these electrons is between 30-300 eV, which have a wavelength that is less than or equivalent to the interatomic distances

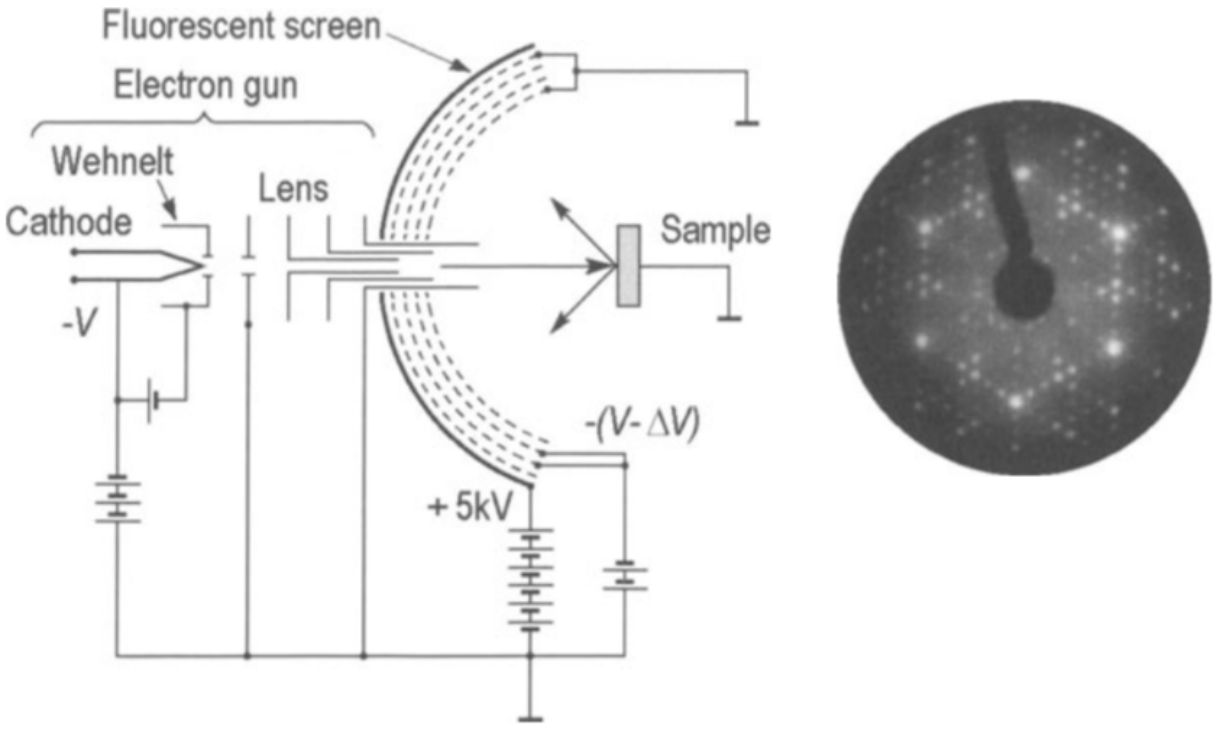

Figure 2.9: left: Accelerated electrons are emitted by an electron gun composed of a filament, Wehnelt, and electrostatic lens. They are then backscattered from the sample, passing through a series of grids, and fluoresce on a Phosphorous screen. right: a typical LEED pattern on a Si(111) 7x7 surface. Figure taken from (Oura *et al.* , 2010).

for a typical surface. In addition, the mean free path of these electrons is on the order of a few atomic layers, making this a very surface sensitive technique. A typical LEED setup is shown in Figure 2.9 (Oura *et al.* , 2010).

For diffraction on a 2D surface, the Ewald sphere construction (Oura *et al.* , 2010) can be used to find the proper diffraction conditions and extract the reciprocal lattice from the diffraction patterns, see Figure 2.10. Here, the incident wavevector $\mathbf{k}_0$ terminates at a reciprocal lattice point. A sphere of radius $\mathbf{k}_0$ is then drawn. Then, assuming that there is no periodicity in the z direction, the reciprocal lattice would consist of a periodic array of lines or 'rods' pointing normal to the crystal surface. The scattered intensity along these rods is weakly modulated, however, as the backscattered electrons do probe the perpendicular lattice periodicity, albeit over a very small distance into the solid. The intersection of these rods with the Ewald sphere satisfies the Bragg condition and thus contains positions

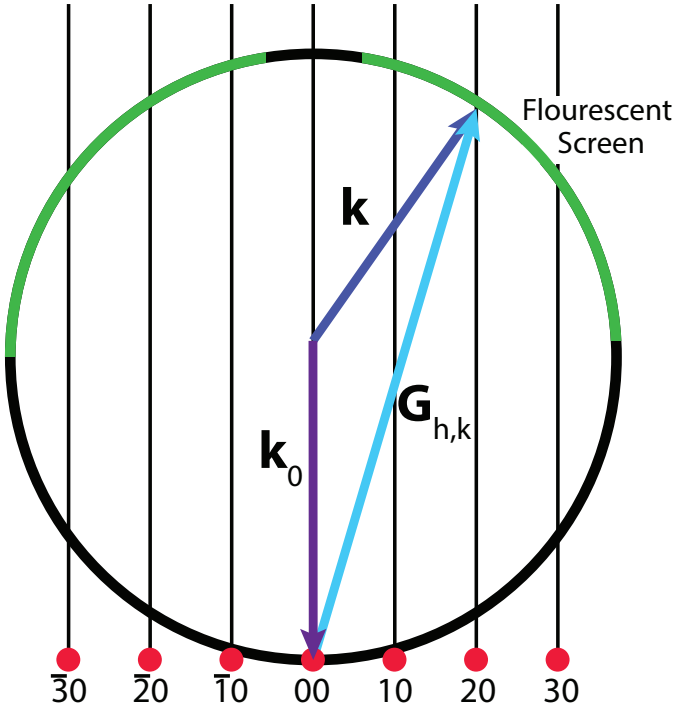

Figure 2.10: The Ewald sphere in 2D.

of constructive interference of the scattered electron beam. It follows that the diffraction pattern is directly related to the surface reciprocal lattice $\mathbf{G}_{h,k}$ by

$$\mathbf{k} - \mathbf{k}_0 = \mathbf{G}_{h,k},$$

where $\mathbf{k}$ is the scattered wave vector. In other words, the LEED pattern is an image of the 2D reciprocal lattice. In this work, LEED will be used to verify the symmetry and quality of the surface.

2.3.4 Photoemission Spectroscopy

Photoelectron spectroscopy (PES) is commonly used in condensed matter systems for studying the chemical composition and electronic structure of complex systems (Hüfner, 2013). The basic principle of PES is the photoelectric effect, where a beam of photons ejects an electron through photoionization. A model for this process is the so-called 'three-step

model' (Avella & Mancini, 2013), which describes the process by which an electron absorbs a photon, moves through a material to the surface, and is ejected into the vacuum. The kinetic energy E_K of this electron is given by

$$E_K = \hbar\omega - E_{\mathrm{i}} - \phi$$

where $\hbar\omega$ is the energy of the photon, E_{i} is the binding energy of the initial state of the electron, and $\phi = E_{\mathrm{vacuum}} - E_{\mathrm{Fermi}}$ is the work function of the electron energy analyzer (Oura *et al.* , 2010).

X-ray photoelectron spectroscopy (XPS) can be used to analyze the elemental composition, chemical state, and electronic configuration of a surface. The core levels show up as sharp peaks whose locations are defined by the electron binding energies, and thus represent a fingerprint of the atomic species on the surface. XPS provides a quantitative measure of the photoelectron intensity that can be used for quantitative analysis of the chemical composition of a surface, such as determinating the atomic composition ratio or stoichiometry of the metallic alloy or chemical compound, or for calibrating the adsorbate coverage during thin film growth.

Typical setup of an XPS system is given in Figure 2.11. It consists of an X-ray source, which can either be from a synchrotron-based light source or from bombarding an elemental anode source with high energy electrons. In this work, we will use the latter method, where the anode is made of aluminum. Then, the Al K_α emission spectra ($\hbar\omega = 1486.6$eV) is selected using a monochromator. Emitted electrons from the sample are selected using a hemispherical analyzer, which is composed of a series of lenses and concentric hemispheres to create an electric field where only electrons of a specific energy are selected to arrive at the detector.

The PES process for XPS described above is typically angle-integrated. However, by using a 2-D detector, manipulating the sample through the angles θ and ϕ, and using a photon source with higher energy resolution, the full bandstructure of the surface can be mapped. Specifically, an ultraviolet source allows a comprehensive study of the valence and conduction bands of a surface. This is commonly called Angle Resolved Photoemission

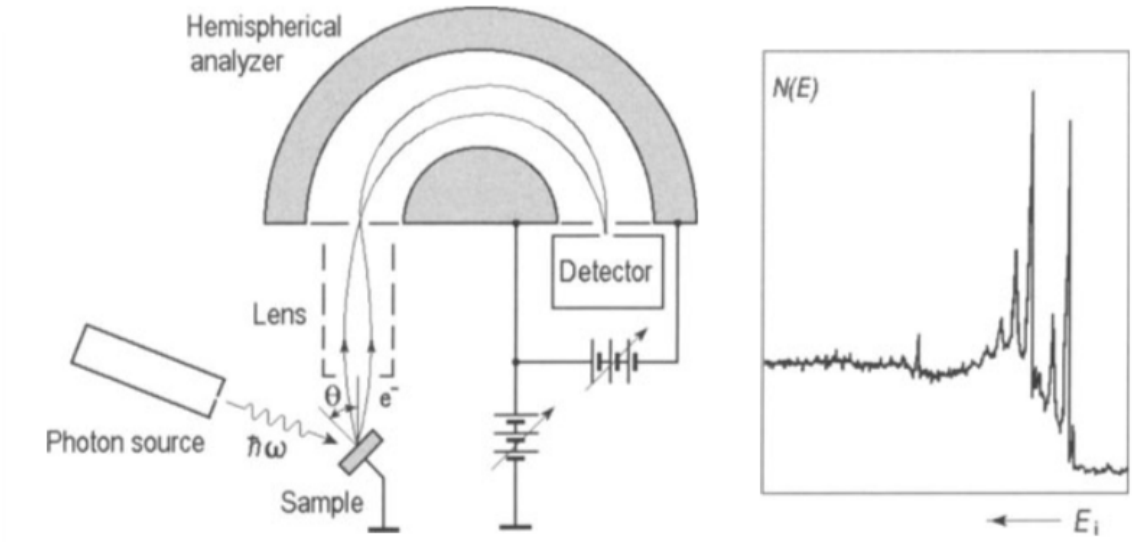

Figure 2.11: left: Schematic diagram of the XPS setup (taken from (Oura *et al.* , 2010)) Primary components are the photon source, sample, and hemispherical analyzer. Right: An example of an XPS spectrum of an aluminum sample.

Spectrosocpy (ARPES). The following paragraphs contain a short summary of the ARPES technique.

(This section modified from (Palczewski, 2010)). In a semiclassical approach, the momentum of photoelectrons outside of the sample is given by the relation

$$k = \frac{\sqrt{2mE_k}}{\hbar}$$

, where the wavevector can be separated into parallel and perpendicular components to the surface

$$\vec{k} = \vec{k}_{\perp} + \vec{k}_{||}$$

. Due to the translational symmetry at the surface, the parallel components of the momentum are conserved, while the perpendicular component is not. This is a consequence of the fact continuous symmetry is broken perpendicular to the surface, and thus the momentum conservation quantity cannot be derived using Noether's theorem (in this specific case, there exists a surface potential due to the surface-vacuum interface). This dependence can be neglected in the case of systems that are inherently 2D, where the primary momentum

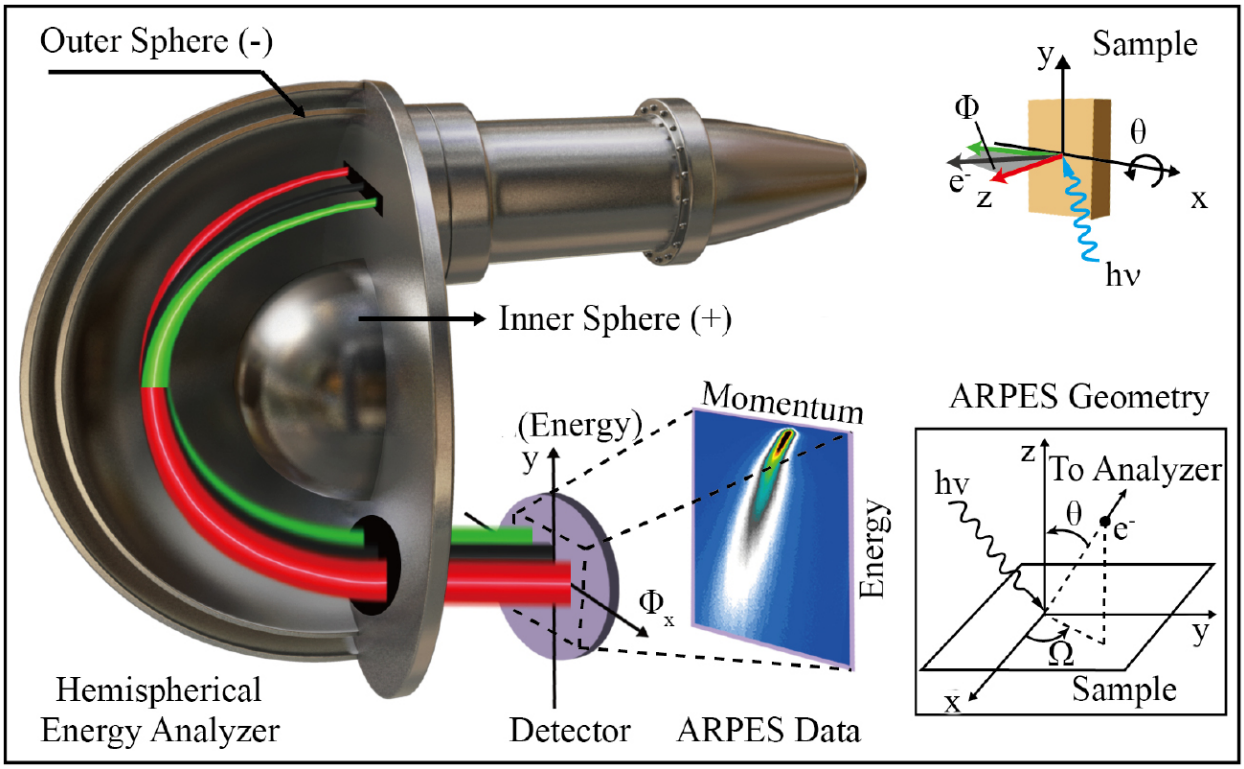

Figure 2.12: Left: Working principle of the ARPES hemispherical analyzer with 2D detector. Right: A schematic of the ARPES geometry, the emission angle is given by θ and ϕ. Taken from (Zhou *et al.* , 2018).

directions are perpendicular to the surface. For 2D systems, $\vec{k}_{\perp}$ is undefined, so only $\vec{k}_{||}$ is a conserved quantity, and thus becomes the quantity in consideration. Therefore, the momentum-dispersion relation $E(k)$ can directly be measured by changing the emission angle of the surface (Figure 2.12).

It is important to note that in order to fully describe the ARPES process, a full quantum mechanical derivation of the photoemission process is needed, as the electrons are in the presence of screening charges due to the existence of a crystal. In actuality, ARPES measures the single-particle spectral function that includes the electron self energy Σ, which contains all of the interactions of the electrons with other electrons and the crystal. The self energy posseses both a real and imaginary component that are related to the peak position and peak width when combined with ϵ_K, respectively. A detailed derivation of the many-body

description of PES is beyond the scope of this work, but has been covered extensively in reference (Avella & Mancini, 2013).

Chapter 3

Growth and Characterization of the K/Sn/Si(111) surface

3.1 Introduction

The Sn/Si(111) surface is one of the four so-called α-phases grown on either the Ge(111) or Si(111) semiconductor surfaces. These phases have been interesting testbeds for studying structural phase transitions and correlated electronic phenomena since their discovery several decades ago (Carpinelli *et al.* , 1996; Weitering *et al.* , 1997b; Goldoni & Modesti, 1997; Profeta & Tosatti, 2007; Cortés *et al.* , 2006; Tejeda *et al.* , 2007, 2008; Cortés *et al.* , 2013). At first glance, these low-dimensional phases are quite simple. However, they have continuously shown to be nuanced in both their physical and electronic properties due to the sublte interplay between their charge, lattice and spin degrees of freedom. In particular, the Sn/Si(111) surface studied in this chapter stands alone from the others, as it does not undergo a charge-order transition at low temperature (Ortega *et al.* , 2002). Moreover, it exhibits an insulating Mott-Hubbard ground state with possibly antiferromagnetic order (Li *et al.* , 2013), in contrast to the metallic ground states of the other systems (Modesti *et al.* , 2007). In this work, this system will be explored through a combination of modulation doping and adsorbate doping in an attempt to explore the full phase space of electronic and structural ground states for this surface. Specifically, the decoration of the Sn/Si(111) surface with alkali adatoms is found to induce a charge-order transition where the alkali dopants adsorb

at strongly preferred lattice sites. At elevated temperatures, the alkali atoms begin to diffuse across the surface and the alkali sublattice ultimately melts near room temperature. This 2D melting transition starts with short-range positional fluctuations in the K sublattice while maintaining long-range order, followed by longer-range K diffusion over small domains, and ultimately resulting in a molten sublattice. Concomitantly, the charge order of the Sn host lattice collapses in a multistep process with both displacive and order-disorder transition characteristics. Our combined experimental and theoretical analysis provides a rare insight into the atomistic processes of a multistep melting transition of a two-dimensional materials system.

Section 3.2 covers the experimental and theoretical background on this system, including recent results from a collaborative study. Section 3.3 describes the K calibration, registry, and morphology of the charge ordered $(2\sqrt{3} \times 2\sqrt{3})$-K ground state. Section 3.4 gives the experimental and theoretical results of a full temperature dependent study on this system, describing a concomitant sublattice melting and charge order transition. Section 3.5 contains LEED and ARPES results on this system. Section 3.6 shows preliminary results on a very similar charge ordered phase on the sister Pb/Si(111) system.

3.2 Experimental and Theoretical Background

The Si(111)-$(\sqrt{3} \times \sqrt{3})$ R30°-Sn surface is composed of $\frac{1}{3}$ ML of Sn adsorbed onto the clean Si(111) surface. The Sn adatoms are situated at the four-fold coordinated T_4 sites above the Si atoms, where all the dangling bonds of the Si substrate are passivated by the Sn adatoms, and where each Sn adatom possesses one half-filled dangling-bond orbital. A structural model and STM topographical image is shown in Figure 3.1. In a single-particle picture, the dangling bonds form a half-filled metallic surface state band.

As was mentioned above, this surface shows the potential to be an exemplary case of a single-band Mott-Hubbard Insulator. This is a result of the fairly large interatomic separation between the Sn atoms of 6.6 Å. In this highly localized regime, the overlap of atomic wavefunctions between the Sn adatoms is small, and the carrier tunneling or hopping probability between the adatoms is correspondingly reduced. Then, the energy cost to move

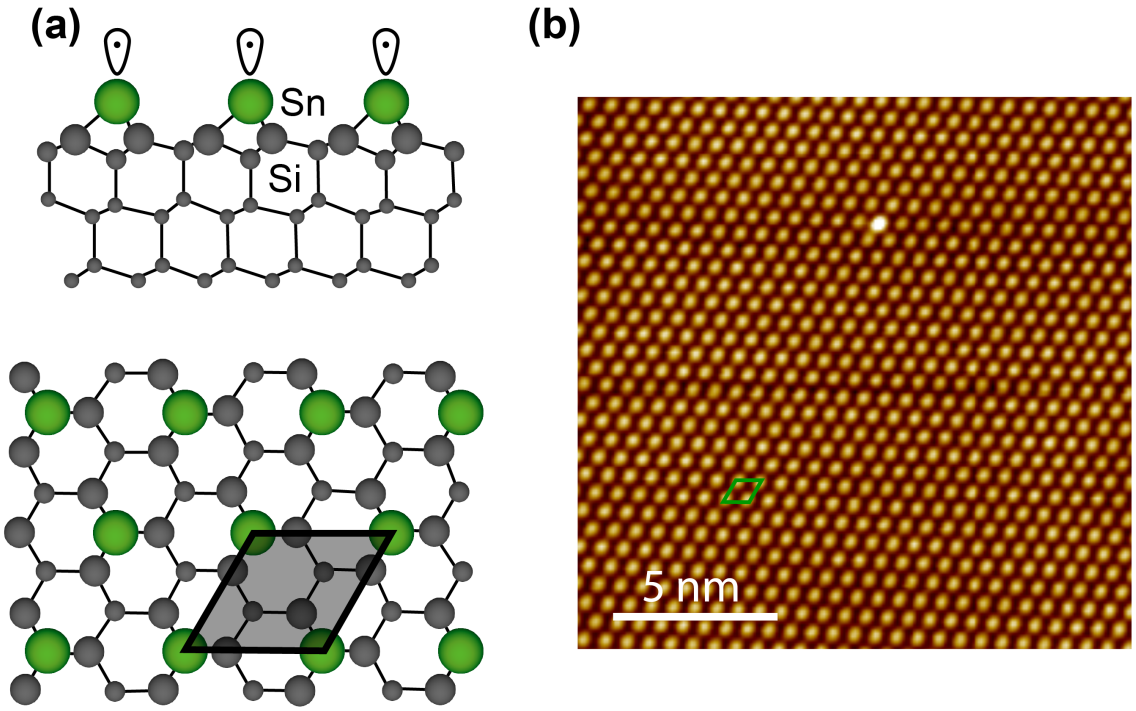

Figure 3.1: (a) Side and top views of the Si(111)-($\sqrt{3} \times \sqrt{3}$) R30°-Sn surface. The Sn adatoms are at the T_4 sites (green spheres). The gray spheres are the Si atoms below the grown deposited Sn atoms. The ovals above the Sn atoms signify the half-filled dangling bonds (one electron per dangling bond). The unit cell of the Sn reconstruction is marked by a shaded diamond. (b) STM topography image of the Si(111)-($\sqrt{3} \times \sqrt{3}$) R30°-Sn surface at 77 K, acquired at a sample bias of +2.0V and tunneling current of 200 pA. The bright defect is a Sn vacancy.

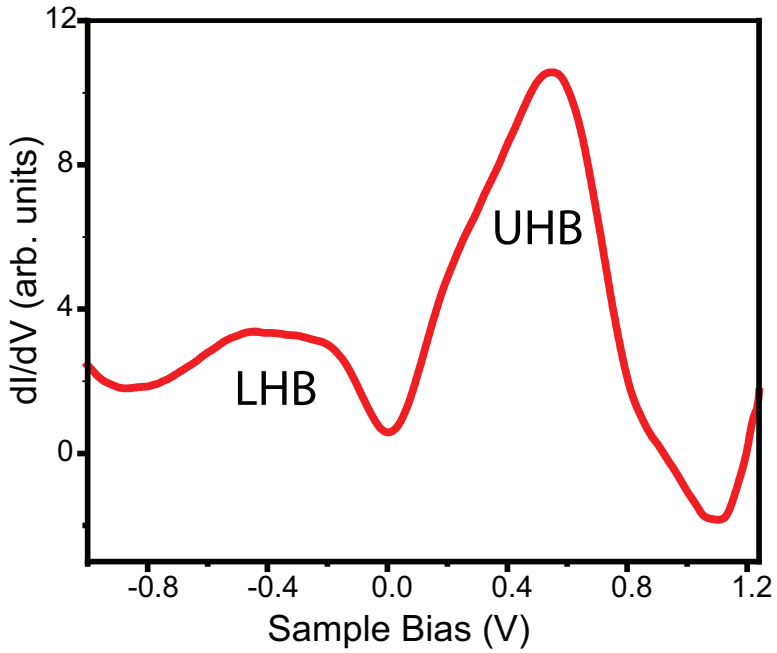

Figure 3.2: STS spectra taken on the undoped Si(111)-($\sqrt{3} \times \sqrt{3}$) R30°-Sn surface at 77 K.

an electron to a neighboring site, forcing the double occupancy of the dangling bond orbital, is greater than the kinetic energy gain associated with charge delocalization (i.e., U>W, where W is the bandwidth, respectively), and the half-filled surface-state band splits into two separate bands, called the Lower Hubbard Band and Upper Hubbard Band (LHB and UHB, respectively). STS on the Si(111)-($\sqrt{3} \times \sqrt{3}$) R30°-Sn surface shows a very clear LHB and UHB centered at -0.4 eV and +0.5 eV, respectively, with a Mott gap of about 0.2 eV. This is shown in Figure 3.2 (Ming *et al.* , 2017).

An interesting effect of the electronic correlation in Mott-Hubbard systems is the quite different behavior of the system in response to carrier doping (as compared to an ordinary band insulator), which can induce a metal-insulator transition via spectral weight transfer (FC-MIT) (Imada *et al.* , 1998). A schematic of the effect of doping of uncorrelated versus correlated systems is given in Figure 3.3. A typical 'non-interacting' semiconductor exhibits an occupied valence band and unoccupied conduction band, separated by an energy gap E_{gap}. As can be seen in the left panel of Figure 3.3(a), an undoped semiconductor composed of N sites with one doubly occupied orbital per site has $2N$ states occupied and $2N$ states

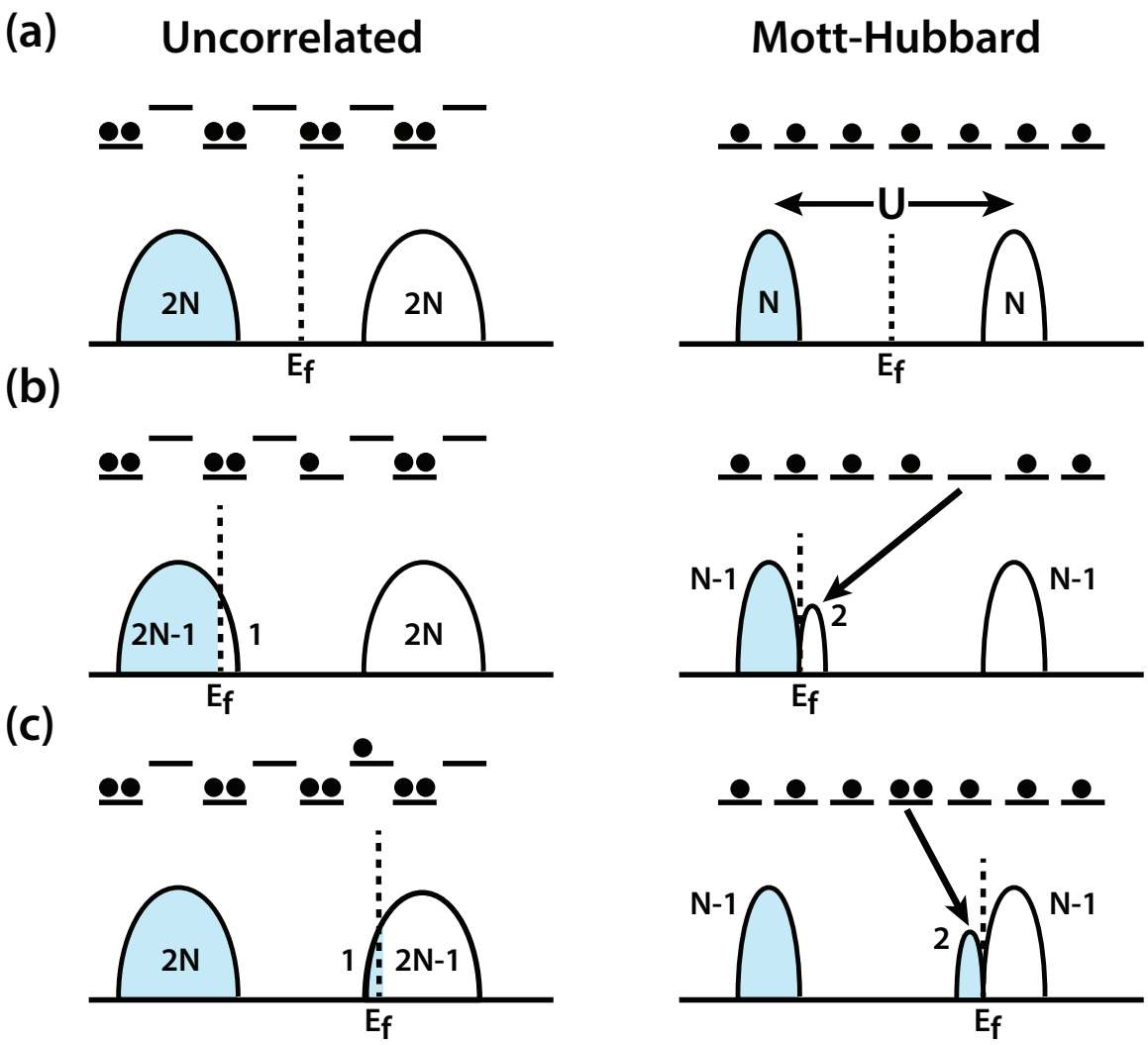

Figure 3.3: Schematic of the electron-addition and -removal spectra for an uncorrelated semiconductor system (left) and correlated Mott-Hubbard system in the localized limit (right) for the undoped (a), one-hole doped (b) and one-electron doped (c) cases. Note that the uncorrelated system has two distinct energy bands defined as the valence and conduction bands. The valence band represents a continuum of doubly occupied states whereas the conduction band only has empty states. In the Mott-Hubbard scenario, we consider a nominally half-filled band (one electron per orbital), where the density of states consists of two Hubbard bands, separated by the on-site Coulomb repulsion U that prohibits double occupancy. Modified from (Eskes *et al.* , 1991; Meinders *et al.* , 1993).

unoccupied. If one were to dope this system by removing an electron, the Fermi level (FL) will shift into the occupied band, leaving $2N+1$ electronic states above the FL and $2N-1$ below (Figure 3.3(b)). Electron doping the system behaves the same, leaving $2N+1$ states below the FL and $2N-1$ states above (Figure 3.3(c)). As a result, doping the uncorrelated

system results in a rigid shift of the chemical potential without any redistribution of spectral weight.

However, in a correlated electron system, the removal or addition of electrons will reduce the amplitude (spectral weight) of the UHB and LHB, creating a new feature in the density of states of different energy with a weight proportional to the number of carriers introduced. This is often called the quasiparticle peak (QPP) (Eskes *et al.* , 1991; Meinders *et al.* , 1993). For an intuitive picture, we can draw another simplified model. If we single-hole dope a Mott-Hubbard system of N electrons sitting on N atoms (right panel of Figure 3.3(b)), there will now be $N-1$ sites that are singly occupied, and as a result there are $N-1$ ways of removing an electron from a singly occupied site and $N-1$ ways to doubly occupy an atomic site. Therefore the amplitude (spectral weight) of both the LHB and UHB decreases from N to $N-1$. Since there are two ways to add an electron to the fully empty site, both of these electron-addition states will correspond to an energy slightly above the LHB (if the impurity potential of the dopant is neglected) (Eskes *et al.* , 1991; Meinders *et al.* , 1993). As seen in the right panel of Figure 3.3(b), these unoccupied states will correspond with a spectral weight transfer from both the LHB and UHB to a new feature above the Fermi level (Meinders *et al.* , 1993). Electron doping has the same effect: Since there are $N-1$ ways of adding another electron, the FL will be located below the UHB with an amount of spectral weight transferf below the FL corresponding to the amount of carriers introduced (Eskes *et al.* , 1991).

The as-grown Si(111)-($\sqrt{3} \times \sqrt{3}$) R30°-Sn surface makes for a very unique testbed to study these correlation effects, as Si(111) wafers can be bought commercially for a variety of doping levels. By changing the doping level of the bulk, the resulting imbalance of the Fermi levels in the bulk and at the surface will cause a charge transfer between the surface and the bulk. This concept, historically named "modulation doping" (Chang & Ploog, 1985), involves decoupling the surface layer from the ionized donors. Then the impurity atoms can be separated from the system of interest enough to minimize scattering from the charged cores of impurities, while being close enough for the impurities to donate their corresponding

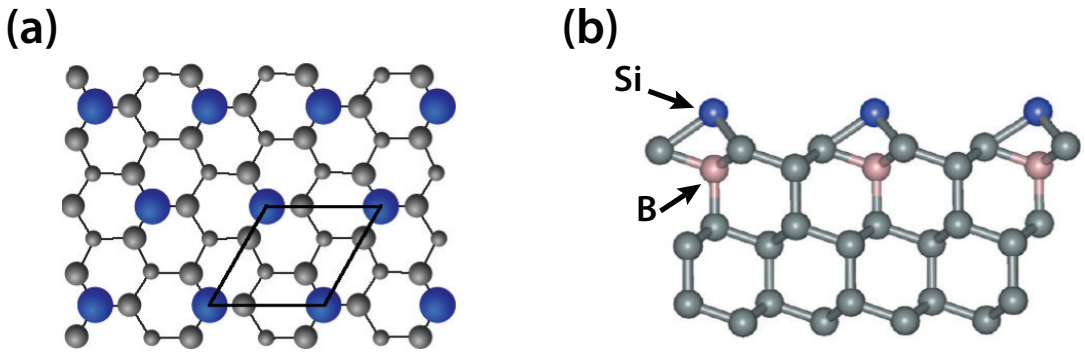

Figure 3.4: Top view (a) and side view (b) of the most heavily hole doped $(\sqrt{3} \times \sqrt{3})$-R30°-B surface. The subsurface Boron atoms at the S_5 sites are positioned beneath the Si atoms (blue). The $(\sqrt{3} \times \sqrt{3})$ unit cell is drawn in black.

carriers. Previously*, we successfully explored this idea by doping this system up to a 10% surface hole doping level using a variety of commercially available silicon wafers (Ming *et al.* , 2017) . The most heavily hole-doped system was grown on a unique surface, exhibiting a $(\sqrt{3} \times \sqrt{3})$ R30°-B reconstruction which is induced by the segregation of Boron into the S5 positions just below the surface (Bedrossian *et al.* , 1989; Huang *et al.* , 1990; Headrick *et al.* , 1989). A schematic of this surface is given in Figure 3.4, and a topographic image is given in Figure 3.7(d),(e).

The results of the modulation doping study is summarized briefly here. Figure 3.5 shows a series of doping dependent $\frac{dI}{dV}$ tunneling spectra. The bottom spectra is taken on the same surface as the "undoped" case in Figure 3.2. As the hole doping is increased, a new peak appears between the LHB and UHB, increasing in amplitude and driving the system into a metallic phase. This is the QPP, providing "smoking gun" evidence of correlated Mott physics. Zoomed in spectra at lower temperatures also shows a sharp peak right below the Fermi Level, attributed to a van Hove singularity in the DOS (see Figure 3.5(b)) due to a saddle point in the surface band dispersion at the $\bar{\text{M}}$ point (Ming *et al.* , 2017; Piriou *et al.* , 2011). This has rarely been observed in the DOS measured by STM. However, a

*This experiment was led by Dr. Fangfei Ming. This author assisted and received training while working on this project.

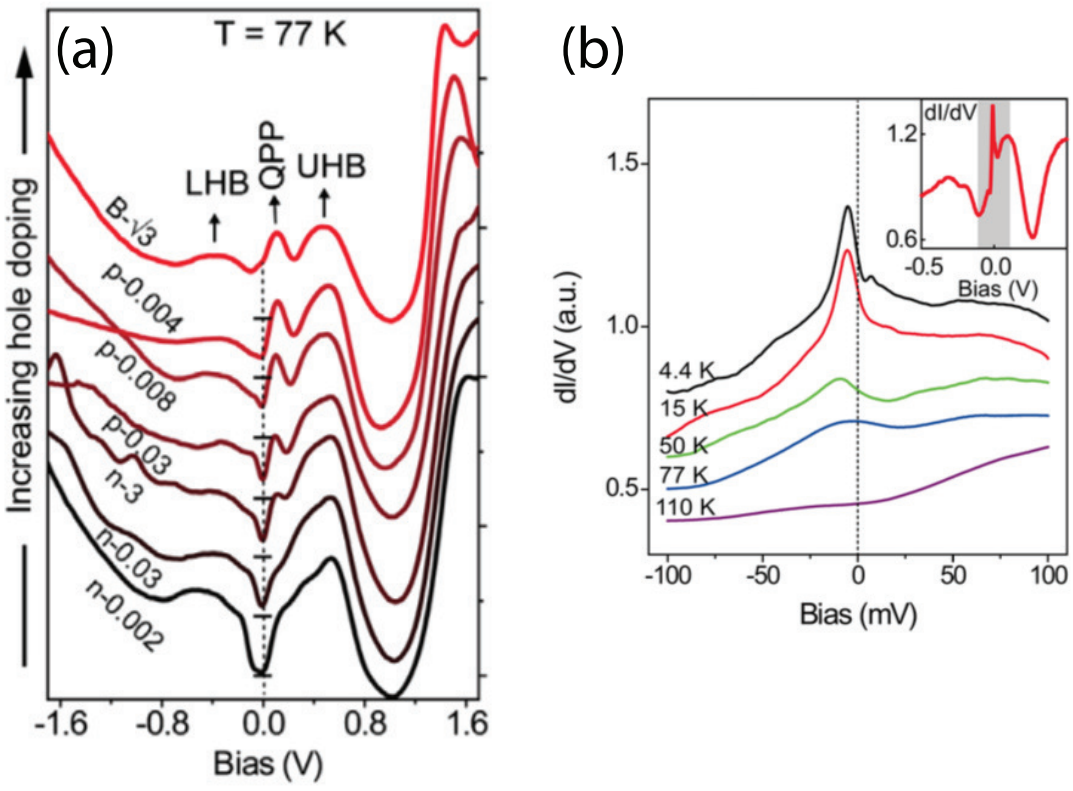

Figure 3.5: (a) $\frac{dI}{dV}$ spectra measured at 77 K for the Si(111)-($\sqrt{3} \times \sqrt{3}$) R30°-Sn system grown on different substrates with different doping levels. (b) High resolution $\frac{dI}{dV}$ spectra taken at various temperatures on the most heavily hole-doped surface, revealing a Van Hove Singularity at -6 meV.

select few systems have been shown to have VHS by STM, such as the doped cuprates and twisted graphene layers (Piriou *et al.* , 2011; Li *et al.* , 2010). These systems both exemplify superconductivity and charge density wave instabilities. This suggests a possible electronic instability below the 4.5 K temperature limit of the LT-STM in our laboratory.

These observations led to further work on this doped system in another LT-STM capable of reaching a temperature of 0.4 K. This author assisted in preliminary measurements with Dr. Kedong Wang's group and Dr. Fangfei Ming at The Southern University of Science and Technology of China in Shenzhen, Guangdong, China. Ultimately, it was found that this system indeed undergoes a superconducting transition with a T_C of ∼4.7 K. STS results of the superconducting transition are given in Figure 3.6. Though fits of the pairing symmetry do not rule out a conventional s-wave pairing channel due to electron-phonon coupling,

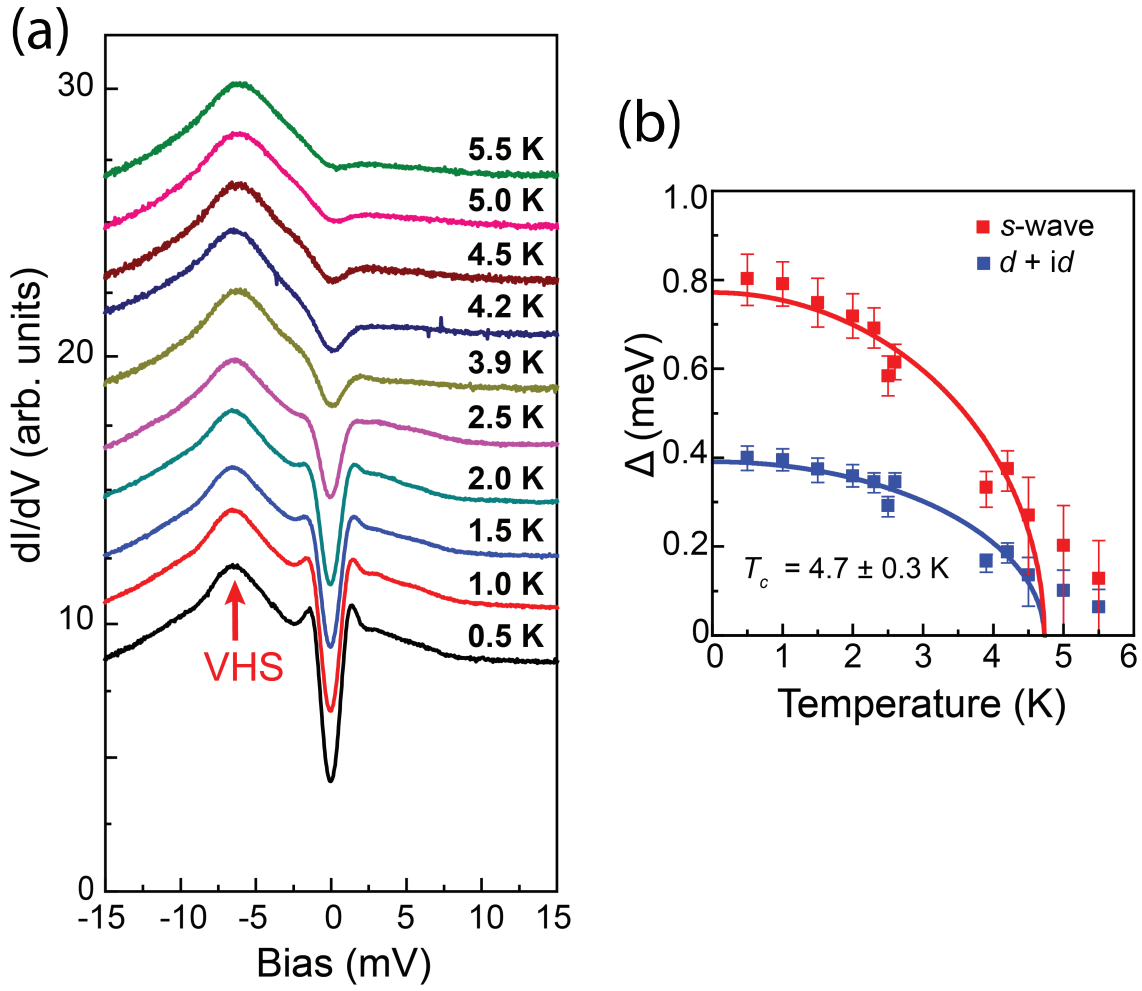

Figure 3.6: (a) Temperature dependent $\frac{dI}{dV}$ spectra of the most heavily hole-doped Si(111)-$(\sqrt{3}\times\sqrt{3})$ R30°-Sn surface. The superconducting gap is seen as a "dip" at zero bias. (b) The superconducting gap as a function of temperature. STS spectra are fit using both s-wave and chiral d-wave gap functions, which both agree on a superconducting transition temperature of $T_C = 4.7\pm0.3$K. Taken from Wu *et al.* (2019).

the strong Hubbard interaction and Coulomb repulsion should suppress the conventional channel and prefer an unconventional pairing symmetry. Details on this experiment and the corresponding analysis are given in Wu *et al.* (2019).

The modulation doped experiment shown here is an intriguing example of doped Mott physics, with many similarities to the results found in complex oxide physics (Segawa *et al.* , 2010). However, this system is unique as it is easily accessible with both ARPES and STM. It has a simple structure with well-defined chemical composition and represents one of the

very few examples of a single-band Mott insulator. A natural next step is to explore the effect of further doping. Unfortunately, the modulation doping approach has been limited to the availability of commercially available substrates, with a maximum hole doping limit of ∼10%. In addition, this doping scheme is not viable for electron-doping the system. Reasons include surface depletion of As or Sb carriers, as well as Boron contamination from Borosilicate components inside the UHV systems used to grow these surfaces (Liehr *et al.* , 1987). This contamination counteracts whatever doping level there is in the bulk, causing a significantly reduced n-type doping level near the surface. Other doping schemes must be utilized if the other side of the doping-dependent diagram is to be explored.

In order to overcome these limitations of the modulation doping technique, a new avenue must be pursued. One possible way of realizing this is placing charge dopant atoms directly on the surface in situ. Specifically, the use of potassium adatoms for surface doping experiments was originally posited and successfully implemented on the Si(111) surface (Weitering *et al.* , 1993). This technique, called adsorbate doping, has also been successfully utilized for 2D materials such as WSe_2, Graphene, and $FeSe_2$ (Wen *et al.* , 2019a; Zhang *et al.* , 2016). Adsorbate doping has also been used successfully to enhance the critical temperature in the high T_C cuprates (Hossain *et al.* , 2008). In these systems, adding potassium adatoms to the surface typically results in a noticeable hole doping, as each K atom tends to donate its electron due to its relatively low ionization energy of 4.34 eV/atom. The following sections outline the results of potassium addition onto the Si(111)-($\sqrt{3} \times \sqrt{3}$) R30°-Sn surface.

3.3 Growth and Surface Morphology

The growth of the Si(111)-($\sqrt{3} \times \sqrt{3}$) R30°-Sn surface, followed by the deposition of K, is a multi-step process. First, (111) oriented silicon wafers are prepared by flashing at ∼1200° C in the metal MBE chamber (Section 2.1). This results in a clean and ordered Si(111)-7x7 reconstruction for n-type and moderately doped p-type wafers, and a Si(111)-($\sqrt{3} \times \sqrt{3}$) R30°-B reconstruction on the most heavily doped p-type wafers due to surface segregation of boron dopants. For the latter case, the sample is annealed at ∼1030° C for some minutes to increase the B segregation, thus reducing the defect concentration. Before continuing to

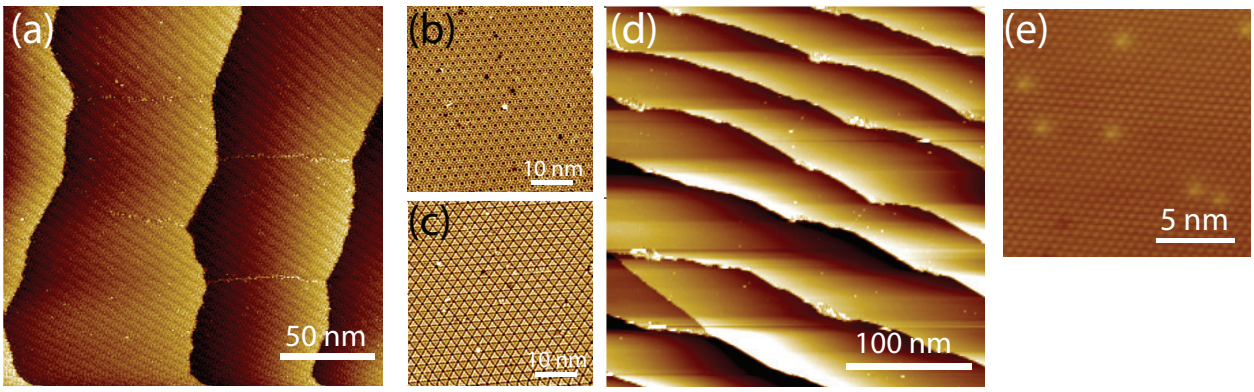

Figure 3.7: (a) Large scale image of a freshly prepared Si(111)-7x7 surface. (b),(c) show smaller scale images with atomic resolution in the unoccupied and occupied states. (d) Large scale image of a freshly prepared Si(111)-($\sqrt{3} \times \sqrt{3}$) R30°-B surface. (e) Small scale image of the surface in (d).

the next step, the sample quality is always checked by STM. STM topography images of clean wafers after this surface preparation process is given in Figure 3.7.

Freshly prepared surfaces are then transferred back to the metal MBE chamber, where the samples are brought to and held at a temperature of ∼600° C. A high-temperature effusion cell outfitted with a PBN crucible is then brought to a temperature of 980° C. Sn is then deposited on the hot sample for several minutes, followed by a post-anneal after deposition at the same temperature. STM images of the as-grown surface are shown in Figure 3.8. The morphology of the n-type and moderately doped p-type wafers mostly consist of the 1/3 ML ($\sqrt{3} \times \sqrt{3}$) phase, with a small amount of coexisting higher coverage ($2\sqrt{3} \times 2\sqrt{3}$) domains that appear near the step edges (labeled as $2\sqrt{3}$-HC in Figure 3.8(a)). Though this does not affect the STM study, these higher coverage domains are minimized for the ARPES studies to avoid overlapping of different domains in the measurement. The ARPES studies are presented in Section 3.5.

More heavily doped p-type wafers have a different sample morphology. Due to the presence of the segregated B dopants, the ($\sqrt{3} \times \sqrt{3}$) areas grow in a much more defected fashion. However, by increasing the ratio of the higher coverage ($2\sqrt{3} \times 2\sqrt{3}$) domains, small well-ordered ($\sqrt{3} \times \sqrt{3}$) patches of up to 100x100 nm^2 can be grown. Also seen on these

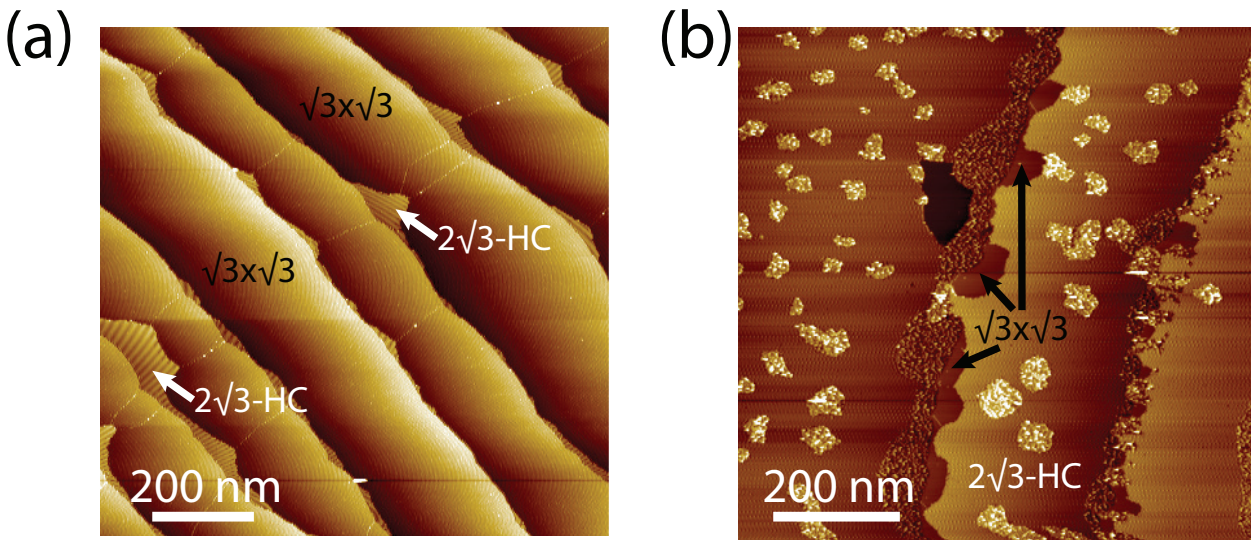

Figure 3.8: (a) Large scale image of the Si(111)-($\sqrt{3} \times \sqrt{3}$) R30°-Sn surface grown on the n-type surface. Only a small amount of the high coverage ($2\sqrt{3} \times 2\sqrt{3}$) (labeled as $2\sqrt{3}$-HC) is seen to nucleate near the step edges. The moderately doped p-type surface grows in an identical fashion. (b) Large scale image of the Si(111)-($\sqrt{3} \times \sqrt{3}$) R30°-Sn surface grown on the most heavily p-doped surface. Here, the high coverage phase makes up the majority of the surface. Images acquired at -1.5 V and 30 pA.

surfaces are amorphous Sn islands, which nucleate randomly across the surface. A large scale STM topography image of this surface is given in Figure 3.8(b).

After confirming the sample quality by STM of the above surfaces, K adatoms are absorbed onto the Si(111)-($\sqrt{3} \times \sqrt{3}$) R30°-Sn surface using a SAES dispenser described on page 15. Due to the diffusive nature of the K atoms, the deposition is done while the sample is still cold. The process is as follows: The sample is left in contact with the LT-STM cryostat and brought to a temperature of 77 K. After stabilization of the K dispenser, the sample is temporarily taken out of the STM sample stage and placed on a transfer arm in front of the potassium cone of emission. After leaving it in this position for some seconds, the sample is returned to the LT-STM. In this manner, a conservative estimate of the maximum temperature of the sample is ∼100 K.

The first part of this study involves the deposition of a small amount of K atoms onto the most heavily doped p-type Si(111)-($\sqrt{3} \times \sqrt{3}$) R30°-Sn surface. However, it was initially found that the K adatoms diffuse quickly over the surface at 77 K (Figure 3.9). Therefore, to

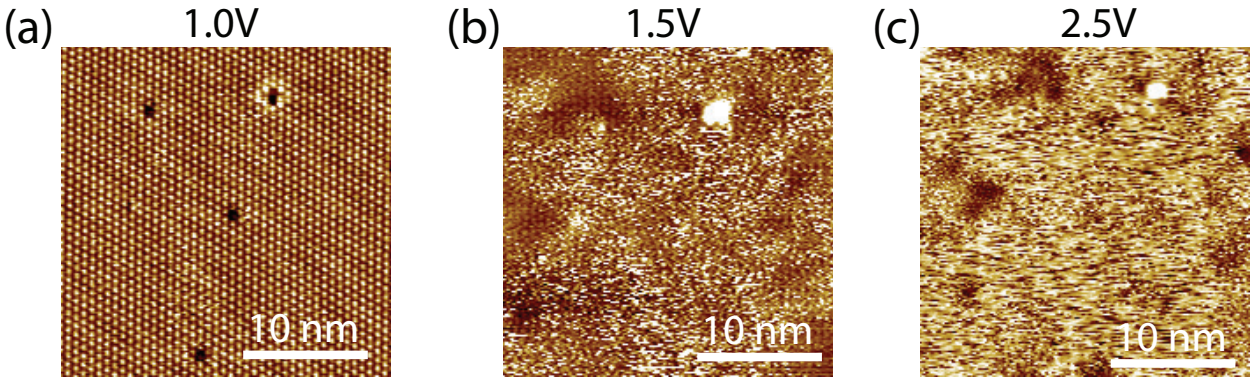

Figure 3.9: (a) STM topography image of the heavily doped p-type surface with a small amount of K deposited at 77 K. The tip tends to repel the K adatoms at some biases and the surface appears clean, while the K adatoms tend to diffuse and be dragged by the tip at others (b),(c). All images taken at 30 pA.

accurately measure the K coverage and for an initial study, the K adatoms were deposited and measured in a "frozen" state at 4.5 K[†]. At this temperature, the sticking coefficient (defined as the number of atoms that stick to the surface divided by the total number of atoms impinging on the surface) can be maximized while surface diffusion is strongly suppressed.

The potassium atoms were deposited onto a surface with coexisting high coverage $2\sqrt{3}$-HC and $(\sqrt{3} \times \sqrt{3})$ domains in order to compare the count the K adatoms. These appear as single point defects on the $2\sqrt{3}$-HC phase (Figure 3.10(a)). The K-decorated $(\sqrt{3} \times \sqrt{3})$ phase was then measured for comparison (Figure 3.10(b)). The simplest potassium construct on these domains appear as bright trimers, with "bowties" forming when two of these trimers are adjacent (circles and boxes in Figure 3.10(b), respectively). By simply counting the atoms on these two domains, the areal density of K adatoms on the high coverage phase is found to be equivalent to the areal density of the trimers on the $(\sqrt{3} \times \sqrt{3})$ domains. It follows that each trimer contains one potassium atom. With this knowledge, the total coverage of potassium is Θ_K=.008 ML, and the deposition rate is ∼.096 ML/min. For confirmation, two other independent methods were used to confirm this deposition rate. Details can be found in Smith *et al.* (2020).

To completely understand the registry of the K adatoms, the small trimer and bowtie constructs on the $(\sqrt{3} \times \sqrt{3})$ can be imaged at various tunneling biases at higher resolution.

[†]4.5 K calibration images taken by Dr. Fangfei Ming.

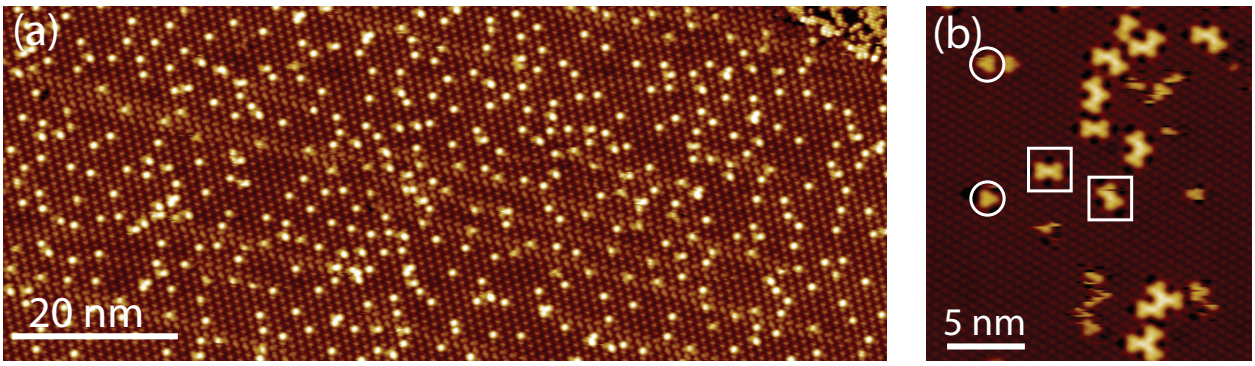

Figure 3.10: (a) STM topography image on the $2\sqrt{3}$-HC domain on a heavily doped p-type surface with Θ_K=.008 ML of potassium measured at 4 K. The adsorbed K atoms appear as bright single-point defects. (b) STM image on the same surface as (a) in a neighboring $(\sqrt{3} \times \sqrt{3})$ domain. K atoms appear as bright trimers in their simplest form (circled). Adjacent trimers appear as bowties (boxes). The areal density of the single points in (a) equal the trimer density in (b).

As mentioned earlier, the simplest construct observed on the surface is the bright trimer unit, shown in Figure 3.11(a). They are observed when imaging in the occupied states, and are in perfect registry with the Sn lattice. It is concluded that these are upward relaxed Sn atoms. Surrounding each trimer are dark depressions, taken as inward relaxed Sn atoms. This is also the case for the bowties, which are simply corner-shared trimer units. It follows that each bowtie contains two potassium atoms. Figure 3.11(d) is a high resolution image at this bias, where each bowtie is seen to consist of 5 bright upward relaxed Sn atoms with 4 dark downward relaxed Sn atoms.

When the tunneling bias is switched into the unoccupied states, a clear contrast reversal is observed (Figure 3.11(b),(e)). This is commonly observed in systems that have charge transfer between atoms on the surface (Carpinelli *et al.* , 1997). The downward relaxed atoms now appear as bright atoms, where the upward relaxed atoms appear slightly dimmer. It follows that the atoms that acquire extra charge relax upwards as measured in the filled state image, while those that relax downwards are depleted of charge and are more visible in the empty state image. This will be confirmed later by DFT calculations.

At higher bias in the unoccupied states is another contrast change (Figure 3.11(c),(f)). In this bias range, the resolution of the Sn atoms is lost. Instead, the trimer and bowtie units appear as single points or dimers, respectively. The individual points (and dimer atoms),

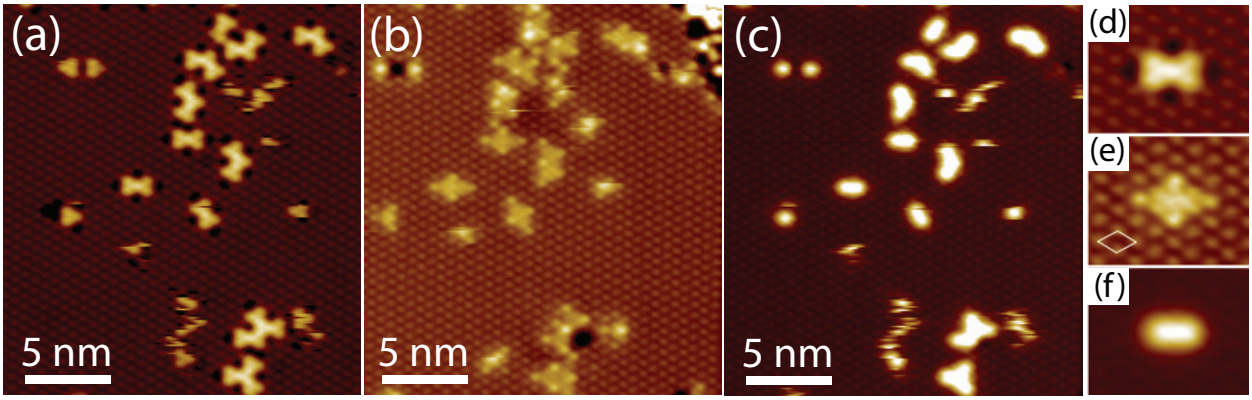

Figure 3.11: Various bias images on the most heavily hole-doped ($\sqrt{3} \times \sqrt{3}$) domain with .008 ML of potassium deposited. Three distinct regions with different contrast are observed. All images are at 30 pA and are measured at a tunneling bias of -0.5 V (a) +0.5 V (b), +1.5 V (c) -0.5 V (d) +1.0 V (e) and +2.0 V (f).

are positioned at the center of the trimer units, between the atoms. These are positions of the potassium atoms.

From these observations, it is apparent that the K atoms have a very local effect and preferential position within the Sn lattice. As the K coverage is increased, the trimer units begin to aggregate into larger units of corner-shared triangles (Figure 3.12). The neighboring trimers have the opposite orientation, seen in simplest example of the bowtie. As a result, the center of all triangles lie on a honeycomb lattice with a ($2\sqrt{3} \times 2\sqrt{3}$) periodicity. This is marked in Figure 3.12(a).

When the coverage of K adatoms totals Θ_K=1/6 ML, the original Si(111)-($\sqrt{3} \times \sqrt{3}$) R30°-Sn surface is converted into a fully homogenous ($2\sqrt{3} \times 2\sqrt{3}$) R30° reconstruction (henceforth called ($2\sqrt{3} \times 2\sqrt{3}$)-K). The diffusion of the K adatoms previously observed is no longer observable in this stable structure, allowing a full topography study to be done in the much less costly temperature of 77 K. The following paragraphs will summarize this charge-ordered phase.

A series of bias-dependent STM images on the ($2\sqrt{3} \times 2\sqrt{3}$)-K phase is given in Figure 3.13. These are taken on the most heavily doped p-type substrate, although identical behavior is observed on the other substrate doping types. As observed in the low coverage phase, three distinct contrast inversions appear, revealing three distinct sublattices.

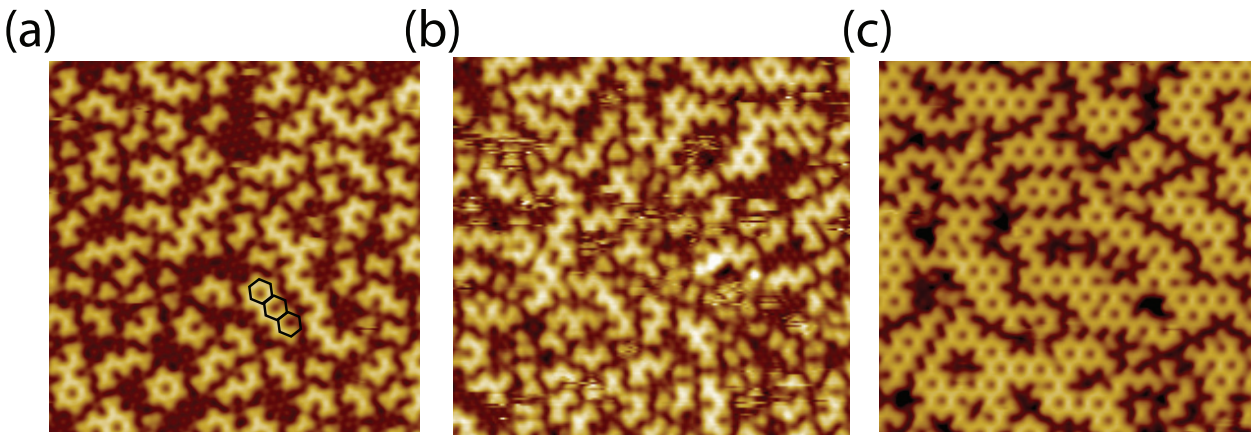

Figure 3.12: The $(\sqrt{3} \times \sqrt{3})$-Sn surface with increasing amounts of adsorbed K adatoms. The center of the chained triangles lie on a honeycomb lattice, marked in (a).

Beginning in the filled states, a Kagome lattice is apparent with three bright atoms and one dim atom per $(2\sqrt{3} \times 2\sqrt{3})$ unit cell (marked in purple in Figure 3.13). These are the Sn up atoms. In subsequent STM images, the bias is incrementally changed towards the empty states. Beginning at around +0.35 V, the contrast inverts, and the previously dim Sn atoms become more apparent. Ultimately, this forms a bright triangular lattice, which is most apparent at +1.0 V. These are the down Sn atoms, and the Kagome lattice is no longer seen clearly. A third contrast inversion begins at around +1.2 V, where the triangular lattice fades and a bright honeycomb lattice appears, becoming most apparent at +2.5 V. These are the K adatoms, located at the center of the chained triangles of the Kagome lattice.

The combination of these observations on bias dependent structures with varied degrees of K coverage provides a fully consistent structural analysis of this phase. This can be defined as a charge ordered phase due to the bias dependent contrast changes that indicate a rearrangement of the charge on the lattice. High quality STM images taken at the most optimal bias for each of the three sublattices are shown in Figure 3.14. In summary, there are four Sn adatoms and two K atoms per $(2\sqrt{3} \times 2\sqrt{3})$ unit cell. With this knowledge and basic electron counting arguments, it can be concluded that there are six valence electrons that must be distributed over four Sn dangling bonds (assuming the K atoms are completely ionized). Therefore, three of the dangling bond orbitals on the Sn atoms are fully occupied, where one is completely empty. This is directly deduced from the bias dependent imaging

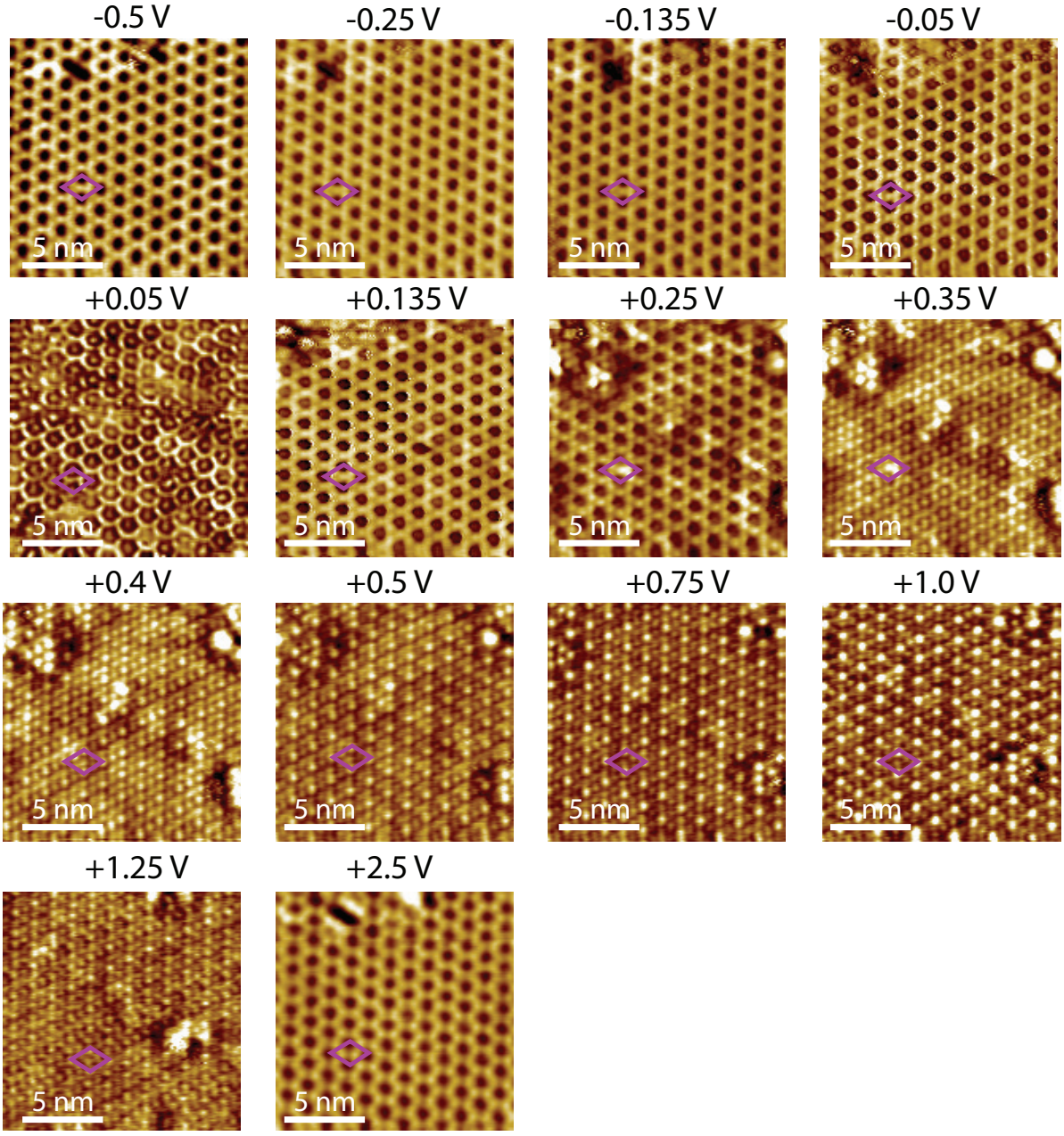

Figure 3.13: A series of STM topography images on the $(2\sqrt{3} \times 2\sqrt{3})$ charge ordered reconstruction with 1/6 ML K on the most heavily doped p-type substrate. All images measured on the same region. STM parameters are the same for all images, with a tunneling current of 100 pA and a temperature of 77 K. The same $(2\sqrt{3} \times 2\sqrt{3})$ unit cell is marked in purple.

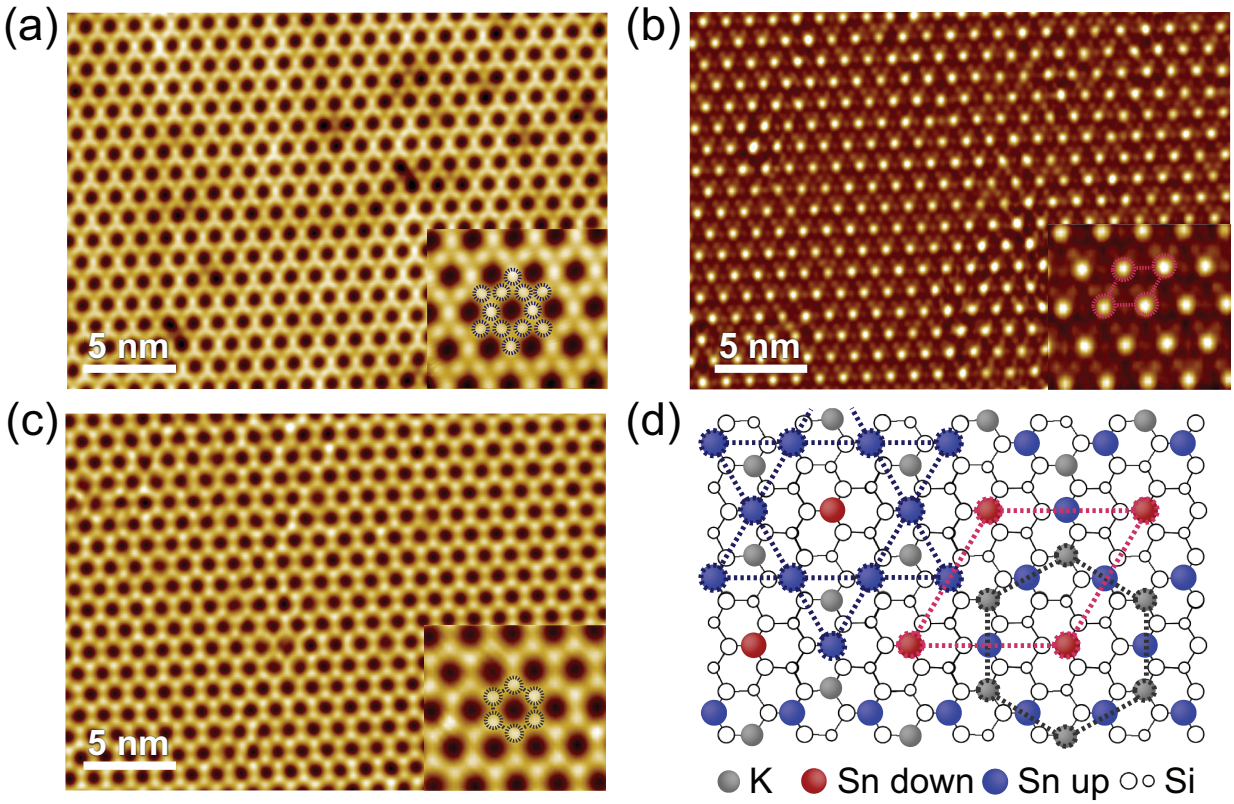

Figure 3.14: High quality STM topography of the three distinct sublattices of the $(2\sqrt{3} \times 2\sqrt{3})$-K on the same surface area. STM parameters are (a) -1.5 V and 1 nA, these are the Sn up atoms that make up the Kagome lattice; (b) 1.0 V and 1nA that reveal the Sn down atoms that make up the triangular lattice ; and (c) 2.5 V and 1 nA, showing the K locations that make up the honeycomb lattice. The insets in are smaller scale images, which more clearly reveal the corresponding sublattices. (d) The $(2\sqrt{3} \times 2\sqrt{3})$-K structure. The K atoms reside at the T4 adsorption sites at the centers of the Sn 'up' triangles. Kagome, Triangular, and Honeycomb lattices are marked in blue, red, and black, respectively.

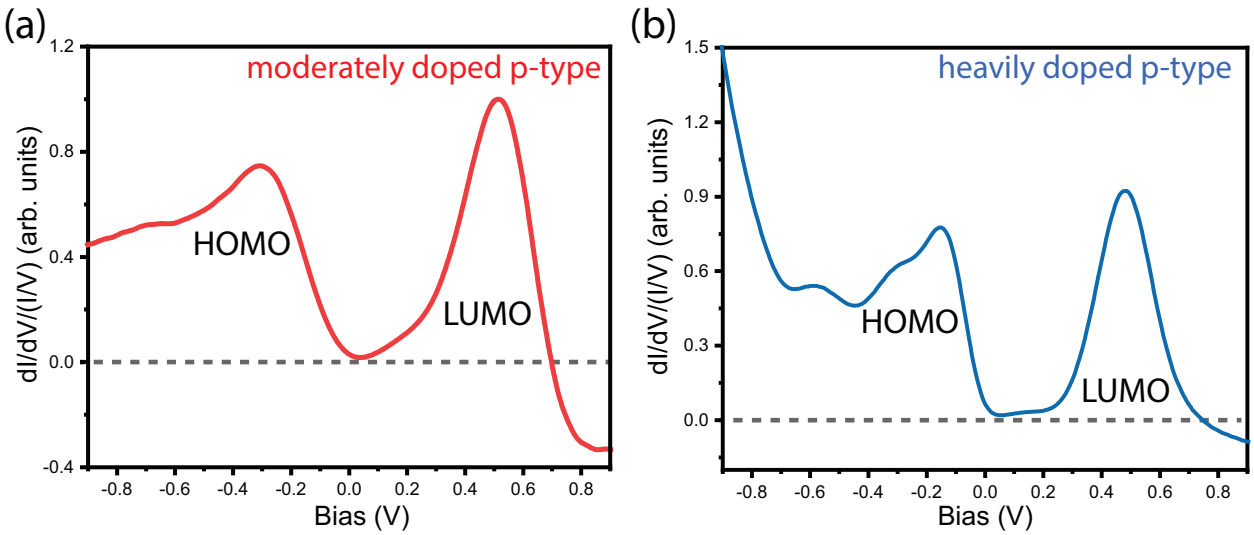

Figure 3.15: Normalized $\frac{dI}{dV}$ spectra on the $(2\sqrt{3}\times 2\sqrt{3})$-K structure on (a) the moderately doped p-type and (b) the heavily doped p-type sample at 77 K.

results, as the three Sn atoms with doubly occupied dangling bonds relax outward and form the Kagome sublattice. In the same way, the Sn atoms with empty dangling bonds relax inward, which forms the triangular sublattice. It is clear that the K adatoms not only donate an electron, but redistribute the charge on the Sn dangling bonds. As the electron filling and structure are highly interlinked, this leads to a periodic buckling distortion of the Sn lattice.

Figure 3.15 shows normalized $\frac{dI}{dV}$ spectra on both the moderately doped p-type and heavily doped p-type substrates at 77 K. Though there are quantitative differences, the qualitative peak positions are very similar. STS is not possible on the n-type at 77 K, possibly due to a smaller substrate conductivity. Here, we will focus on the moderately doped p-type (as it best represents the system without substrate doping or edge effects from the high coverage Sn phase). The most prominent peaks in the LDOS are centered at -0.3 eV and +0.5 eV. In order to describe these features in the LDOS, the language from the electron structure of molecules will be adopted. Then, the feature centered at -0.3 eV will be henceforth called the HOMO (Highest Occupied Molecular Orbital) and that centered at +0.5 eV will be titled the LUMO (Lowest Unoccupied Molecular Orbital). Here, the LUMO is associated with the empty dangling bonds of the down atoms of the triangular lattice, and

the HOMO is associated with the fully filled dangling bond orbitals of the Sn up atoms that make up the Kagome lattice. The ground state is insulating with a HOMO-LUMO splitting of ∼0.85 eV at 77 K.

By comparing to other 2D charge ordered phases that tend to undergo structural and/or electronic phase transitions as a function of temperature (such as other α-phases on Si or Ge (Carpinelli *et al.* , 1997; Dudr *et al.* , 2004)), a logical next step is to perform a full temperature-dependent study on these various physical properties. As will be shown, the $(2\sqrt{3}\times 2\sqrt{3})$-K system undergoes a variety of phase transitions that provide a unique insight into the mechanism behind 2D sublattice melting.

3.4 Temperature Dependent STM/STS

3.4.1 Experimental Results

As the lattice and electronic degrees of freedom are strongly coupled in surface physics, both STS and STM topographical studies can be used to explore the order parameters for phase transitions in 2D. More specific to this case, the HOMO-LUMO splitting observed in the previous section can be taken as a measure of the Sn up-down lattice distortion in the charge ordered $(2\sqrt{3} \times 2\sqrt{3})$-K phase (recall that the HOMO is directly associated with the up atoms, where the LUMO is associated with the down atoms). Therefore, any change in the magnitude of the HOMO-LUMO gap can be taken as a signature of changes of the vertical adatom heights.

Figure 3.16(a) shows temperature dependent normalized $\frac{dI}{dV}$ spectra on the moderately doped p-type surface. (Figure 3.16(b) contains the $\frac{dI}{dV}$ spectra on the most heavily doped p-type for a consistency check. This data is much lower quality due to various experimental difficulties on this surface, such as a higher rate of potassium diffusion on the neighboring high coverage Sn phase, and the small domain sizes of the $(2\sqrt{3} \times 2\sqrt{3})$-K domains). The HOMO-LUMO gap gradually decreases starting at $T \approx 130$ K and levels off at $T \approx 200$ K. This is more easily seen by plotting the full temperature dependence of the HOMO-LUMO

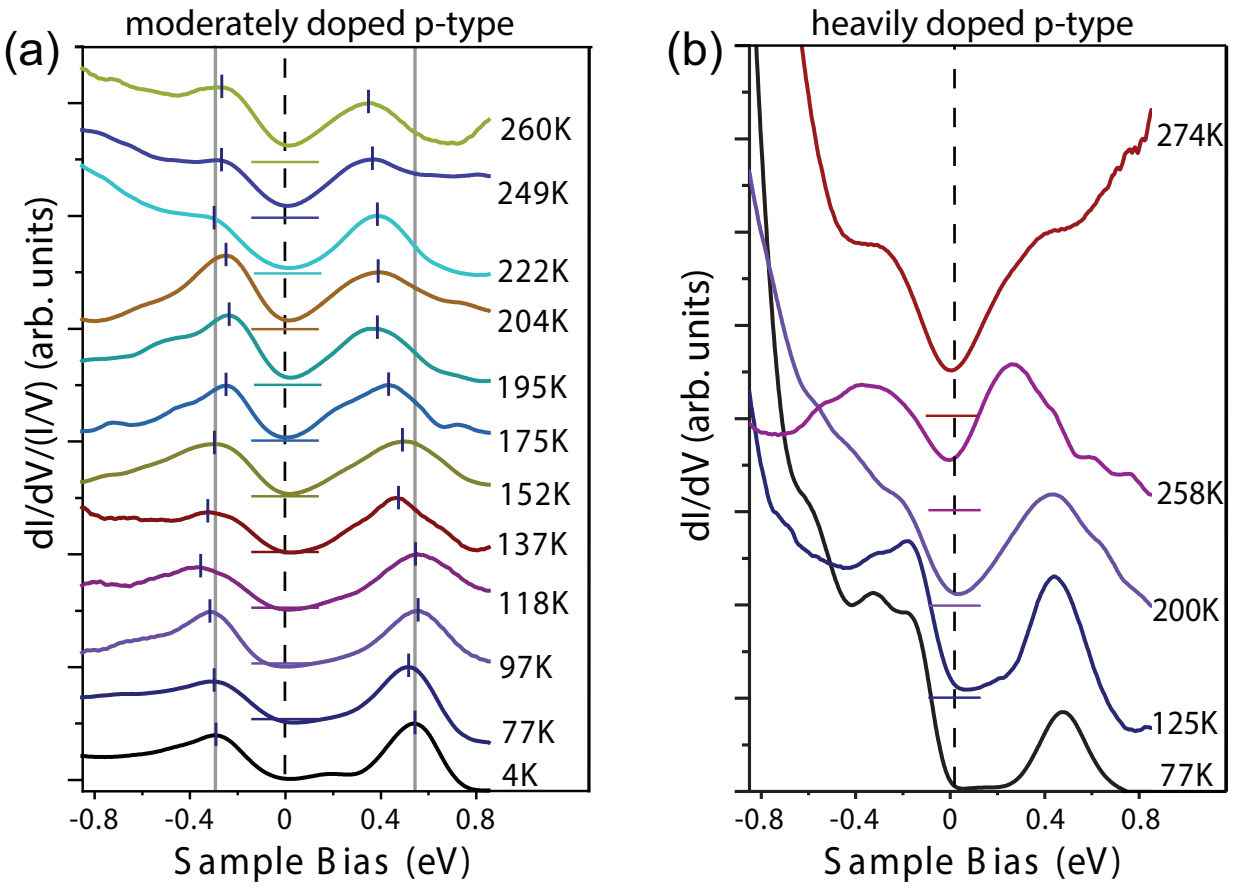

Figure 3.16: (a) Temperature dependent dI/dV/(I/V) spectra of the $(2\sqrt{3}\times 2\sqrt{3})$-K phase on moderately-doped p-type Si(111). Due to the nature of the diffusing K adatoms, spectra were obtained using weak tunneling conditions (I_T=30 pA), averaging several I/V curves and differentiating. The HOMO/LUMO maxima are indicated by vertical tick lines on each curve. Vertical lines mark the HOMO/LUMO locations at 4 K as a guide to the eye. The reduction of the HOMO-LUMO splitting above 118 K is primarily due to the apparent shift of the LUMO state. Horizontal lines below each spectrum indicate the zero of the tunneling conductance for each curve. The gradual increase in zero-bias conductance (ZBC) above 175 K exemplifies a gradual insulator-metal transition. (b) Temperature dependent $\frac{dI}{dV}$ spectra taken on the heavily doped p-type for a consistency check.

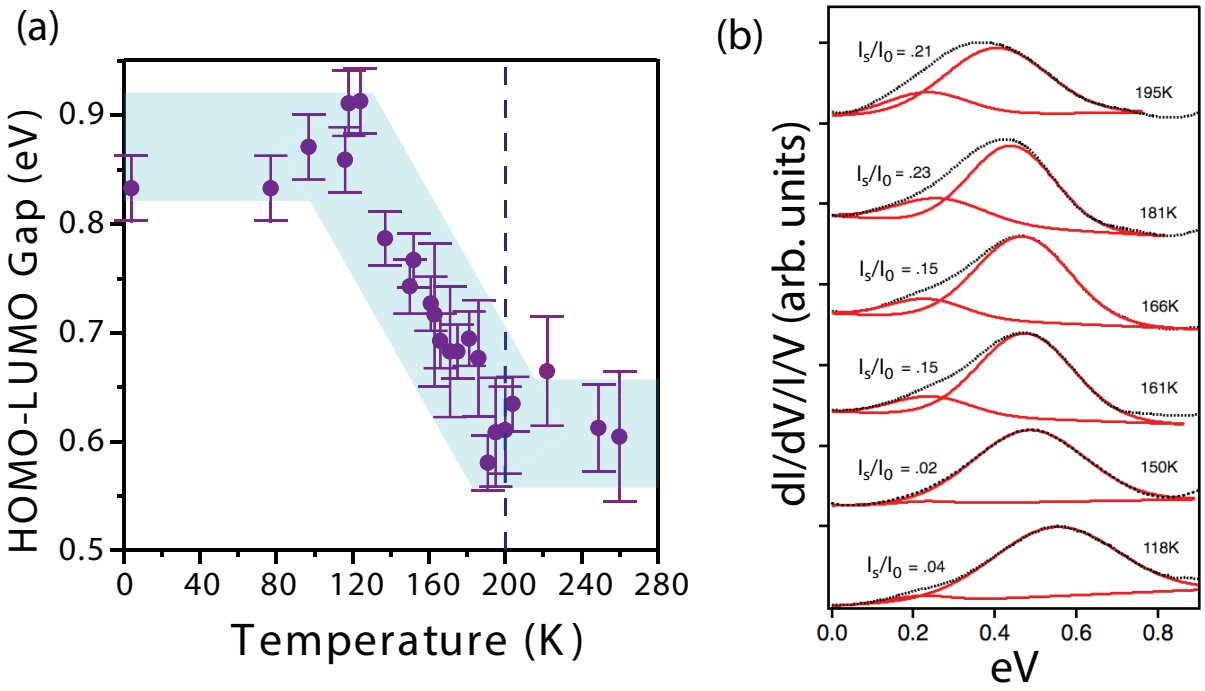

Figure 3.17: (a) Change of the experimental HOMO-LUMO gap on the moderately doped p-type, as measured from the positions of the LDOS maxima. Error bars were estimated from the small fluctuations in the HOMO-LUMO positions in different experimental runs. (b) Gaussian fits of the LUMO as a function of temperature. Though there is still a slight downshift of the main peak, a not insignificant part of the shift is due to the appearance of a shoulder at about +0.2 eV. The ratio of the area of the shoulder to the total area of both gaussians is given by I_s/I_0.

gap, shown in Figure 3.17(a). Note that there is a gradual metal-insulator transition above T = 170 K. The HOMO remains fairly constant at $\sim$ -0.27 $\pm$ 0.03 eV.

The decrease of the HOMO-LUMO gap is primarily due to an apparent downward shift of the LUMO, or more accurately, the formation of a shoulder on the low-energy side of the LUMO state. A more detailed analysis of a few temperature dependent LUMO spectra are given in Figure 3.17(b). These are fit with two gaussians, with a shoulder at an approximate position of +0.2 eV (detailed fitting parameters are given in Table 3.1). The ratio of the area of the shoulder over the total area of both peaks is given as I_s/I_0. This ratio slowly increases as the temperature approaches 200 K. As will be shown in the theory Section 3.4.2, the shoulder is associated with a local Sn adatom relaxation induced by short-range hopping of potassium adatoms.

Table 3.1: Fitting parameters for the gaussian fits in Figure 3.17(b), including the ratios of each peak over the total spectral weight of the LUMO.

Temperature (K)	Peak 1 ratio	Peak position (eV)	Peak 1 width (eV)	Peak 2 ratio	Peak 2 position (eV)	Peak 2 width (eV)
118	0.041	0.215	0.100	0.959	0.551	0.21
150	0.018	0.229	0.090	0.982	0.486	0.190
161	0.152	0.245	0.130	0.848	0.476	0.160
166	0.149	0.234	0.130	0.851	0.469	0.160
181	0.232	0.267	0.150	0.768	0.443	0.150
195	0.209	0.234	0.140	0.791	0.404	0.180

We now move to the temperature dependent topography. All three substrate doping types show consistent behavior, as shown in Figures 3.18 (heavily doped p-type), 3.19 (moderately doped p-type, and 3.20 (n-type). Here, we will focus on the latter. The ground state at 77 K is composed of a surface that is fully covered by the $(2\sqrt{3}\times 2\sqrt{3})$-K structure. Grain boundaries are observable between the charge ordered domains, since there are four equivalent adatom sites per $(2\sqrt{3} \times 2\sqrt{3})$ unit cell prior to K deposition. Therefore, these grain boundaries separate four out-of-phase domains. These are displayed by different colors in Figure 3.20(a). The sample is then slowly warmed up to room temperature by blowing out the liquid nitrogen from both cryostats in the LT-STM. This ensures a very slow thermalization at a rate of $\sim$.1

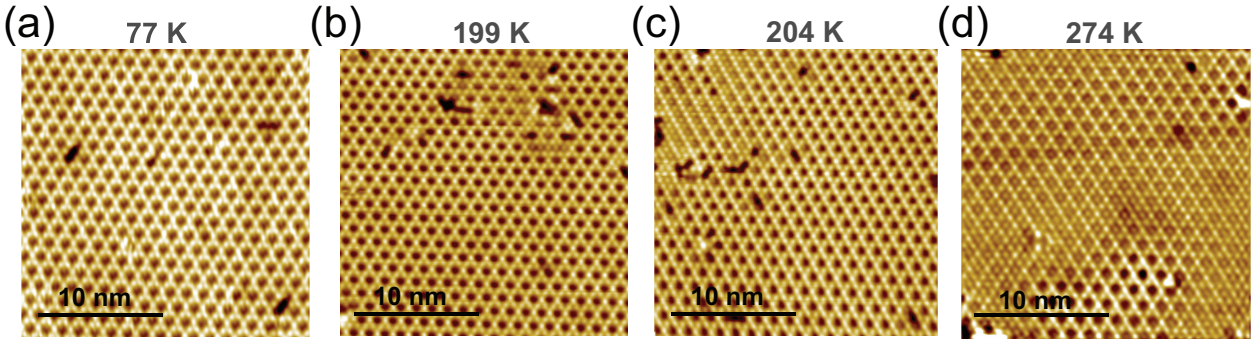

Figure 3.18: Temperature dependent STM topography of the $(2\sqrt{3}\times 2\sqrt{3})$-K structure on heavily doped p-type Si(111). Images were acquired at (a) -1.5 V 30 pA (b-d) -0.5 V 30 pA.

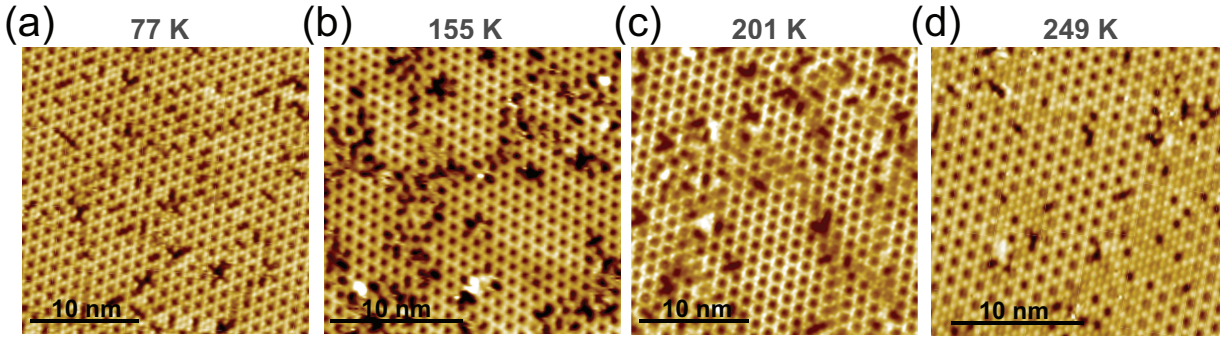

Figure 3.19: Temperature dependent STM topography of the $(2\sqrt{3} \times 2\sqrt{3})$-K structure on the moderately doped p-type Si(111). All images were obtained with a sample bias of -1.5 V and 100 pA tunneling current.

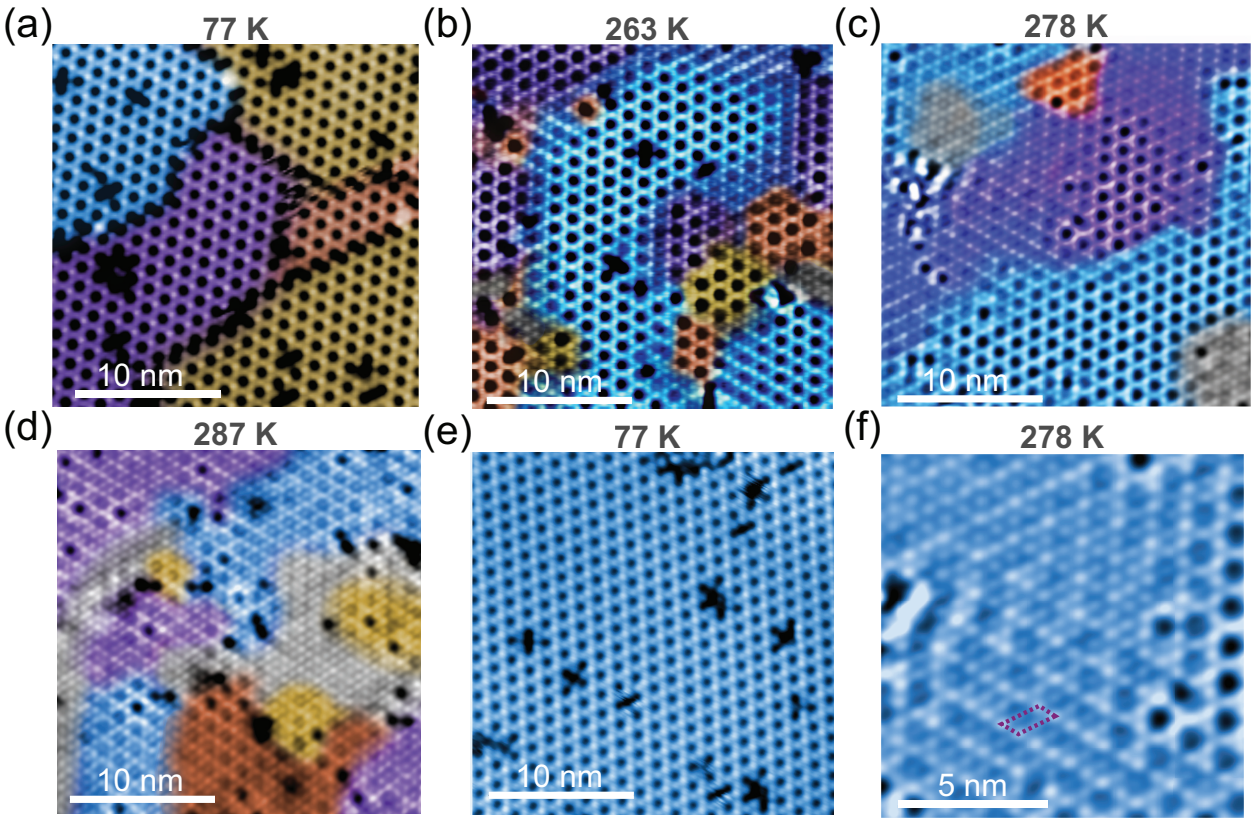

Figure 3.20: Temperature dependent STM topography of the $(2\sqrt{3} \times 2\sqrt{3})$-K structure on n-type Si(111). All images were obtained with a sample bias of -1.5 V and 30 pA current

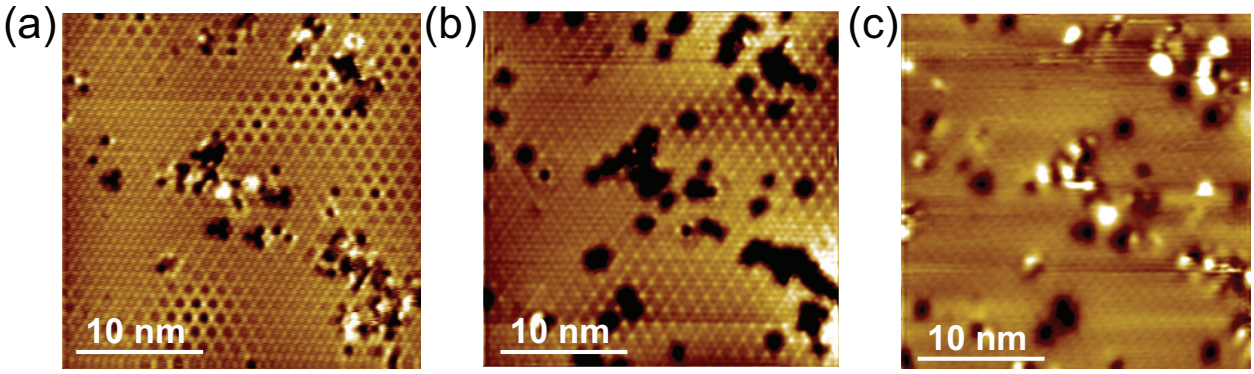

Figure 3.21: STM topography of the $(2\sqrt{3} \times 2\sqrt{3})$-K structure on n-type Si(111) at 294K. These images were acquired at -1.5 V 30 pA (a), 0.5 V 30 pA (a), and 2.85 V 30 pA (c).

K/min (attempts at a faster warming of the sample leads to the destruction of the surface order). As the temperature increases, the grain boundaries begin to disappear, and small patches of the $(2\sqrt{3} \times 2\sqrt{3})$-K phase begin to convert to a new $(\sqrt{3} \times \sqrt{3})$ lattice. These patches (marked in gray in Figure 3.20(b-d)) grow larger as the temperature continues to rise. However, some of the areas do not fully convert to the $(\sqrt{3} \times \sqrt{3})$ order. Some weak $(2\sqrt{3} \times 2\sqrt{3})$ charge ordering still exists at high temperature, as well as another coexisting $(\sqrt{3} \times 2\sqrt{3})$ phase. The latter appears as stripe-like order in Figure 3.20(c) (zoomed in image on this striped phase is given in panel (f)). The sample is then subsequently cooled back to 77 K. STM imaging after temperature stabilization shows a single-domain $(2\sqrt{3} \times 2\sqrt{3})$-K lattice (Figure 3.20(e)), indicative of the "annealing out" of domain boundaries.

Bias dependent topography on this surface at room temperature is given in Figure 3.21. This surface was slightly contaminated as the substrate was allowed to warm over the course of 24 hours for proper thermalization of the LT-STM, causing the (typically cold) cryostat walls to release any cryogenically pumped material into the chamber. However, enough of the surface was preserved to take several high-quality images at various biases. The coexistence of the Kagome and $(\sqrt{3} \times \sqrt{3})$ phases is still seen at this temperature (Figure 3.21(a)). Images of the same area at tunneling bias corresponding to the triangular or Kagome sublattices reveal similar results (Figure 3.21(b)). However, upon measuring the honeycomb lattice, atomic resolution is almost completely lost, with faint signs of $(\sqrt{3} \times \sqrt{3})$ order, which seem

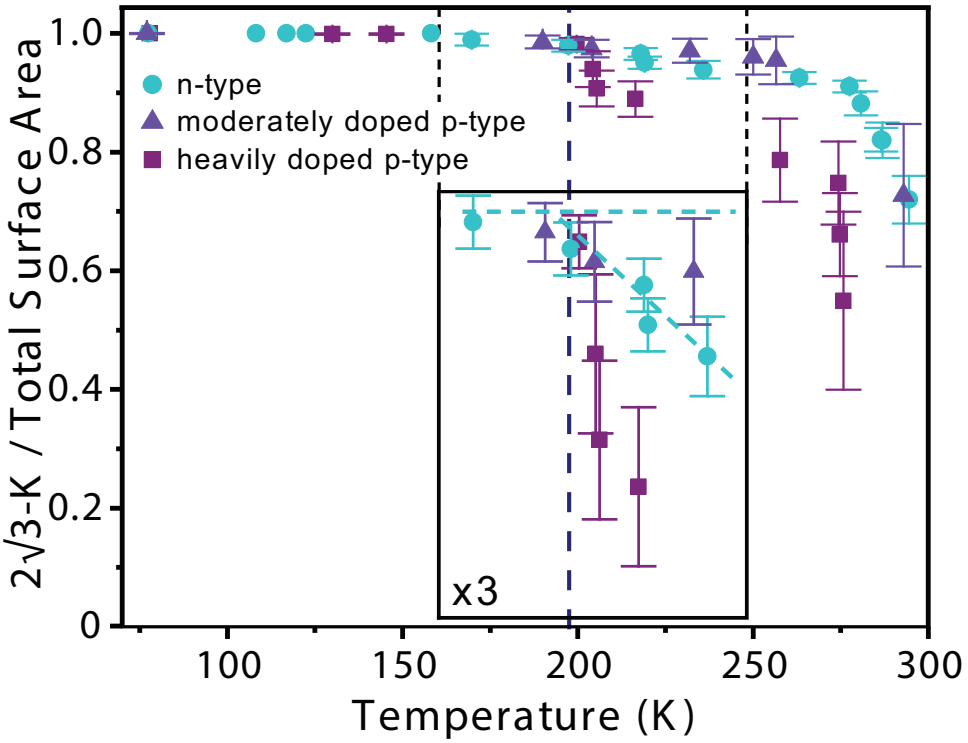

Figure 3.22: Area fraction of the low-temperature $(2\sqrt{3} \times 2\sqrt{3})$-K phase on all three substrates. Dashed lines mark the location of the onset of the $(\sqrt{3} \times \sqrt{3})$ phase. Inset: The onset occurs on all substrates at the same temperature (but with a different rate on different doping types).

to originate from the Sn atoms (Figure 3.21(c)). Imaging at this bias always reveals streaks, usually a sign of diffusing atoms on the surface.

The temperature dependent area fraction of the charge ordered $(2\sqrt{3} \times 2\sqrt{3})$-K phase can be used as another order parameter for the phase transition (that is, in addition to the HOMO-LUMO gap). This is shown in Figure 3.22. Below 200 K, the surface is entirely composed of the $(2\sqrt{3} \times 2\sqrt{3})$ phase. At and above 200 K, the $(2\sqrt{3} \times 2\sqrt{3})$, $(2\sqrt{3} \times \sqrt{3})$, and $(\sqrt{3} \times \sqrt{3})$ phases coexist. Interestingly, this onset temperature agrees perfectly with the leveling off of the HOMO-LUMO gap decrease seen in Figure 3.17. The zoomed-in inset shows that all three substrates behave similarly. However, the surface grown on the most heavily doped p-type substrate seems to behave much more drastically. Another slope change is seen at ∼275 K for the most heavily doped substrate, and at ∼290 K for the other two doping types. Where initially the area fraction decreases much more gradually,

this appears to occur in a much faster manner. This is indicative of a possible first-order transition to the $(\sqrt{3} \times \sqrt{3})$ phase. In the following section, along with corroboration by theoretical calculations, these two regimes will be shown to encapsulate two different phase transitions.

3.4.2 Theoretical Results and Discussion

Density functional theory (DFT) and molecular dynamics within the DFT framework (DFT-MD) calculations were performed using Quantum Espresso and the Fireball code, respectively. (NOTE: Theoretical calculations were performed by the Ortega group, details about the calculation are given in Smith *et al.* (2020).) From the energy-minimized structure, the height difference between the Sn up and down atoms (or between the Kagome and triangular lattices, respectively) is 0.23 Å. In addition, the K adatoms were found to be 0.75 Å above the Sn up atoms (the honeycomb lattice). The structure given in Figure 3.14(d) is in full agreement with these DFT calculations. STM simulations performed by the Ortega group (shown in Figure 3.23) are also fully consistent with the STM topography given in Figure 3.14.

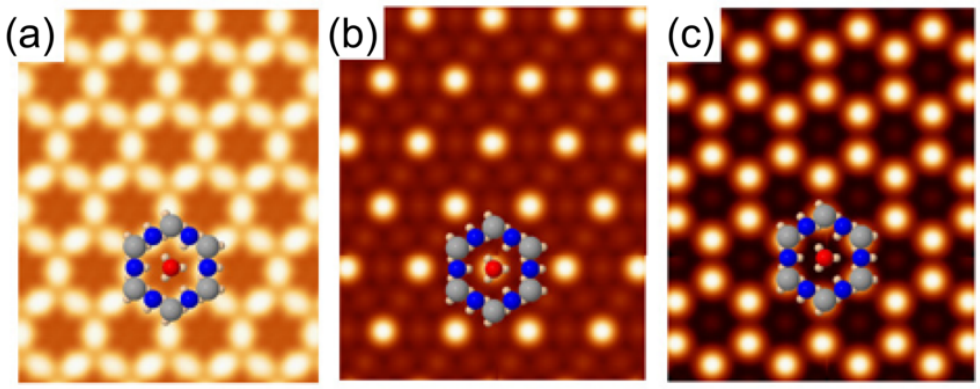

Figure 3.23: Simulated STM images for the $(2\sqrt{3} \times 2\sqrt{3})$-K structure. The images were calculated at a tip-sample distance of 5 Å for different voltages. (a) -1.0 V, (b) +0.5 V and (c) +1.7 V. The atomic structure is superimposed. The blue marbles are the Sn-up atoms and the red marbles are the Sn-down atoms. Grey marbles are the K atoms.

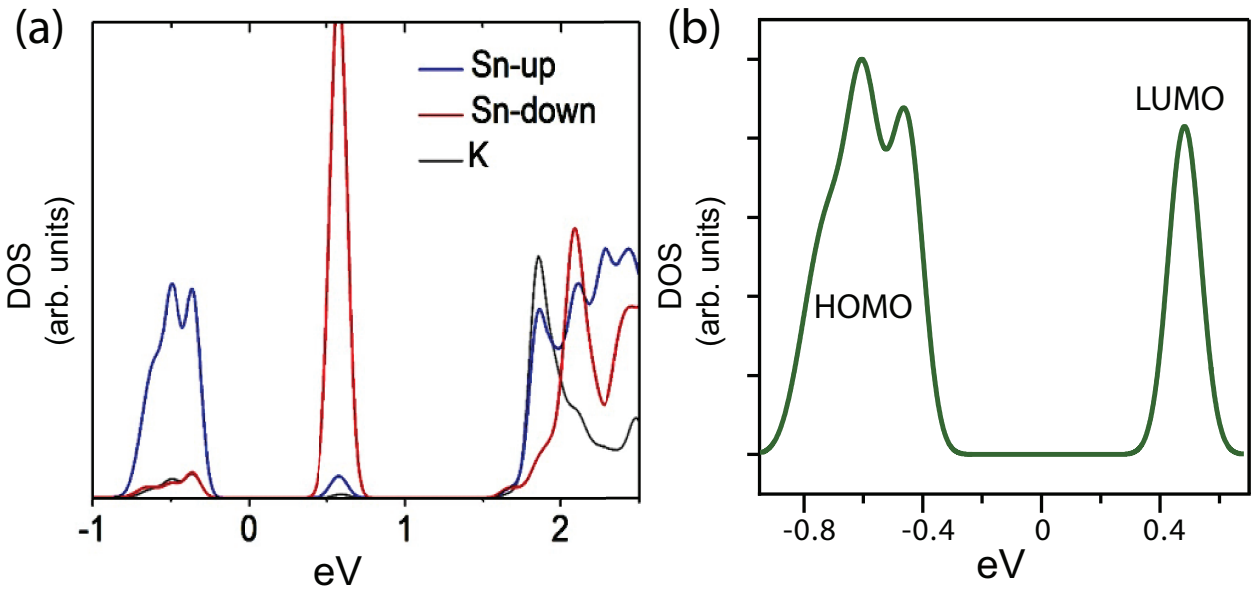

Figure 3.24: (a) Theoretical projected DOS of the $(2\sqrt{3} \times 2\sqrt{3})$-K ground state. The contribution from the Sn-up atoms (blue) dominate the occupied states (which make up the kagome lattice), while the contribution from the down atoms (red) dominates the low energy side of the unoccupied states (these make up the triangular lattice). The potassium atoms (gray) have a greater contribution in higher energy in the unoccupied states (these make up the honeycomb lattice). (b) Total DOS of the $(2\sqrt{3} \times 2\sqrt{3})$-K ground state, in very good agreement with experimental DOS, with only a slight overestimation of the band gap.

The simulated STM images can be more easily understood by comparing to the calculated projected density of states in Figure 3.24(a). This was also calculated with DFT, using the PBE0 hybrid functional (For details, see (Smith *et al.* , 2020)). In the filled states, the Sn up atoms have the strongest contribution to the DOS (blue line). In the empty states, the low energy side is dominated by contributions from the Sn down atoms (red line). The contribution to the DOS from potassium atoms are higher in energy in the empty states (gray line). The dominant contributions from each of these atoms are fully in agreement with the observations made in experiment. In addition, the total DOS in Figure 3.24(b) are in great agreement with the experimental DOS, with only a slight overestimation of the band gap (common in the PBE0 calculations (Hasnip *et al.* , 2014; Garza & Scuseria, 2016)).

With the ground state confirmed by DFT, a possible next step is to perform molecular dynamics calculations at various temperatures in an attempt to describe the phase transitions

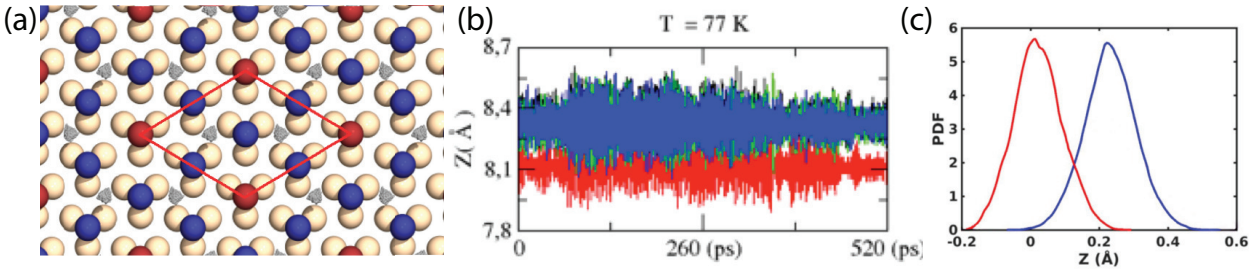

Figure 3.25: (a) Top view of the $(2\sqrt{3} \times 2\sqrt{3})$-K from the DFT-MD calculation at 77 K. Colors of the Sn up, Sn down, and potassium atoms are blue, red, and gray, respectively (same as in in Figure 3.14). (b) Up-down motion of the Sn atoms in the $(2\sqrt{3} \times 2\sqrt{3})$. Each line tracks a different atom in the unit cell. The down atom is in red, the three up atoms are in blue, black, and green. (c) Probability Distribution Functions of the Sn atoms from (b).

observed in experiment. These were first performed at 77 K, where the potassium atoms are shown to rattle around in their respective T_4 sites (Figure 3.25(a)). The Sn atoms also vertically oscillate around their up/down equilibrium positions, shown in Figure 3.25(b). Each atom in the $(2\sqrt{3} \times 2\sqrt{3})$ unit cell is tracked here, but it is obvious that the Sn up atoms (in blue, green, and black) oscillate around the same equilibrium position, where the Sn down atom (red), oscillates at an equilibrium position ∼0.23 Å below that of the Sn up atoms. This is more easily seen by plotting the probability distribution function (PDF) in Figure 3.25(c).

Upon increasing the temperature, potassium atoms begin to fluctuate to neighboring open T4 sites, initially at shorter range (Figure 3.26). In a basic combinatorics argument, there are a total of eight sites per $(2\sqrt{3}\times2\sqrt{3})$ unit cell, leading to 28 possible configurations of the potassium atoms within the unit cell. Only four of them are representative of the ground state. Of course, as these potassium atoms fluctuate, a natural result is that the charge order of the Sn atoms is affected. To gain some initial understanding of this affect, DFT calculations were performed for a system where one potassium atoms is displaced, which creates a larger $(4\sqrt{3} \times 4\sqrt{3})$ unit cell (Figure 3.26(b)). Here, the K atom moves away from one of the Sn up atoms (labeled Sn1), and lands next to a Sn down atom (Sn2). This leads to Sn1 to relax downwards by .04 Å and Sn2 to relax upward by .07 Å (indicated in the figure by lighter shades of blue and red, respectively). The DOS of this new (potassium

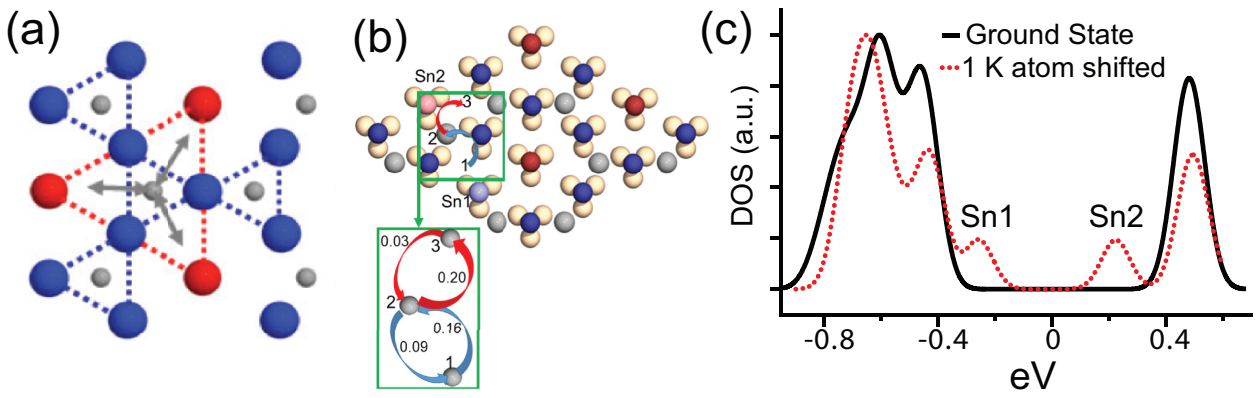

Figure 3.26: (a) An illustration of the behavior of the potassium atoms upon increasing the temperature of the system, where the K atoms visit (previously empty) neighboring T4 sites. (b) The $(4\sqrt{3} \times 4\sqrt{3})$ unit cell when one K atom is displaced from site 1 to site 2. Energy barriers for the hopping between three different sites for the potassium are given in the green box (c) Calculated DOS of the $(2\sqrt{3} \times 2\sqrt{3})$ ground state with LDOS from the $(4\sqrt{3} \times 4\sqrt{3})$ unit cell, that has one potassium neighbor moved to it's nearest T4 site, representing the behavior of the K atoms at increased temperature. New states appear closer to the fermi energy.

displaced) configuration is superimposed onto the ground state DOS in Figure 3.26(c). New states within the ground state band gap appear from the contribution of Sn1 and Sn2 at -0.25 and +0.22 eV, respectively.

By directly comparing these DFT results upon the displacement of one K atom and the experimental shift of the LUMO as a function of temperature, it becomes evident that the increase of spectral weight of the shoulder as shown by the fits in Figure 3.17(b) corresponds to the emergence of the Sn2 state. The Sn1 state does not appear as clearly in the occupied states, simply explained by the greater number of Sn up atoms in the unit cell (a 3:1 ratio). In more detail, the $(4\sqrt{3} \times 4\sqrt{3})$ unit cell with one potassium displaced has a total spectral weight transfer to the Sn1 and Sn2 states of 1/12 and 1/4, respectively.

Figure 3.26(b) also contains the values of the energy barriers for each potassium movement. The initial energy barrier for potassium hopping to the nearest neighbor site is 0.16 eV. However, the energy for the potassium atom to return to its original site is only 0.09 eV, where the energy to hop to another site is 0.20 eV. Therefore, at intermediate temperatures (~150 K), it is much more probable of the potassium atom to return to its

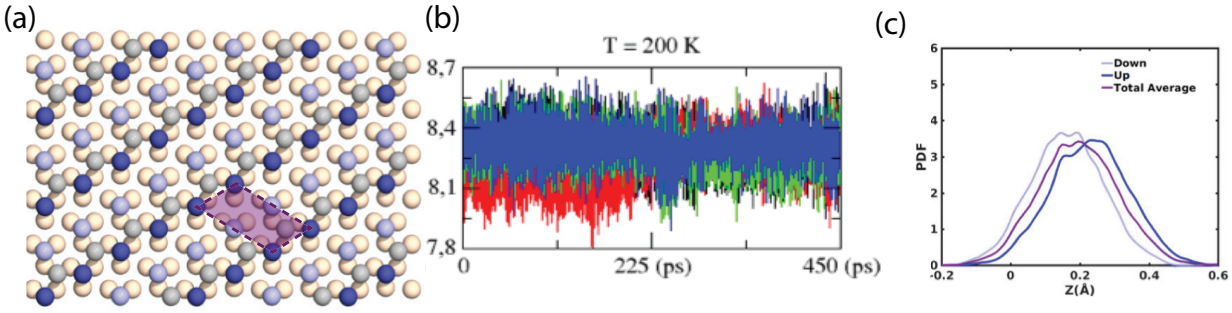

Figure 3.27: (a) Top view of the $(\sqrt{3} \times 2\sqrt{3})$-K reconstruction from the DFT-MD calculation above 200 K. Dark blue atoms are now the up atoms, and light blue atoms are the lower atoms. The $(\sqrt{3} \times 2\sqrt{3})$ unit cell is marked by the purple rhomboid. (b) Up-down motion of the Sn atoms at the transition temperature of 200 K, where the potassium atoms begin to diffuse over longer range. Colors of the atoms are the same as in Figure 3.25. (c) Probability Distribution Functions of the Sn atoms from (b). The purple line is the total average of the Sn atom locations.

original site. This encapsulates the "short range diffusion" of the potassium atoms. However, as the temperature is increased, these energy barriers are more easily overcome.

As the temperature increases above 200 K, the potassium atoms begin to visit all 24 configurations mentioned previously. All of these configurations correspond to a new stripe-like surface reconstruction of $(\sqrt{3} \times 2\sqrt{3})$, in perfect agreement with the intermediate phase observed in Figure 3.20(f). The atomic model for this phase is given in Figure 3.27(a). The movement of the Sn atoms over time at this temperature is shown in panel (b). About halfway through this calculation, the down atoms are seen to buckle upwards, and some of the Sn up atoms move to an intermediate height between the original up-down Sn locations. The overall heights are shown in the PDF in Figure 3.27(c), where the up atoms remain at their original position of +0.23 Å, but the down atoms have increased in height to ∼+0.10 Å below the up atoms. This is in very good agreement with the measured height difference of 0.08 Å by STM. As will be discussed later, this contains the hallmarks of a displacive transition, where the positions that the Sn atoms oscillate around at low T and high T are substantially different.

The last regime for this surface is at room temperature (300 K). Here, the K atoms diffuse very quickly and between every possible T4 site. Figure 3.28 shows the DFT-MD results

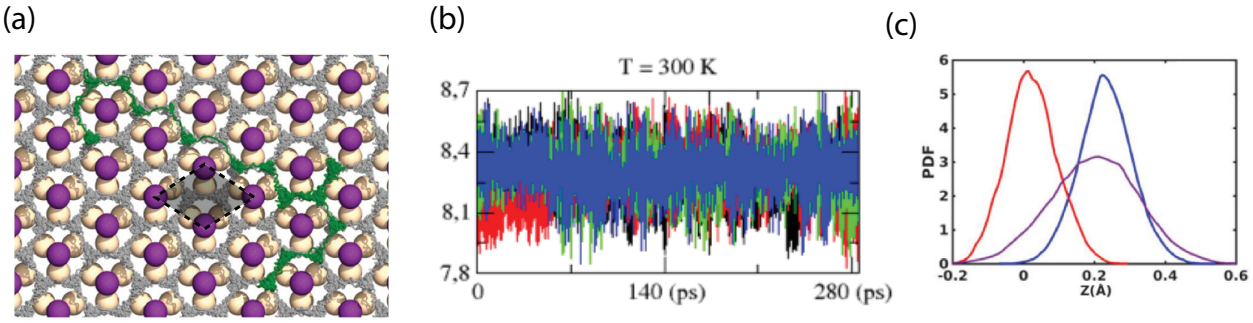

Figure 3.28: (a) Top view of the $(\sqrt{3}\times\sqrt{3})$-K reconstruction from the DFT-MD calculation at 300 K. The gray squiggles track the motion of the K atoms, where the green line follows a signle K atom over 300 ps in the DFT-MD simulation. The $(\sqrt{3}\times\sqrt{3})$ unit cell is marked by the gray rhomboid. All Sn atoms are now equivalent and are marked in purple. (b) Up-down motion of the Sn atoms at 300 K, showing the equivalency of all Sn atoms. Colors of the atoms the same as in Figure 3.25. (c) Probability Distribution Functions of the Sn atoms from (b). The purple line is the position of the Sn atoms at 300 K, where the blue and red are the initial locations of the Sn atoms to emphasize the buckling of the Sn order.

with this molten sublattice. This causes the Sn atoms to fluctuate between all $(\sqrt{3}\times 2\sqrt{3})$ configurations. This results in total loss of charge ordering in the Sn sublattices, with an apparent $(\sqrt{3}\times\sqrt{3})$ reconstruction at 300 K. All Sn atoms now appear equivalent, as seen both experimentally and theoretically (Figures 3.21 and 3.28, respectively). This type of transition is referred to as an order-disorder transition. Here, the disorder is the fluctuation between all of the striped $(\sqrt{3}\times 2\sqrt{3})$ configurations.

3.4.3 Discussion

The combination of the theoretical and experimental work allows a full discussion of this two-step phase transition. As the temperature increases, the potassium atoms begin to move to the nearest empty T4 sites. This is the first regime. The potassium atoms return to their original sites quickly due to the high energy cost to move into other sites, which leads to this regime being strictly short-ranged. Therefore, the surface retains its long-range $(2\sqrt{3}\times 2\sqrt{3})$ order up to 200 K. However, as the potassium atoms move into these nearest-neighbor sites, the charge is redistributed on the Sn dangling bonds, leading to relaxations of the up-down Sn adatom positions. This is directly apparent from the reduction of the HOMO-LUMO

gap and the appearance of a shoulder on the LUMO, leading to a gradual insulator-metal transition.

Above 200 K is the second regime. The potassium atoms begin to diffuse over longer distances and between many sites. The new configurations made by these diffusing potassium atoms make up a new $(\sqrt{3} \times 2\sqrt{3})$ striped-like phase, where the Sn atoms are displaced into new equilibrium positions. As the temperature is increased further, the surface appears as a fully covered $(\sqrt{3} \times \sqrt{3})$ surface as the Sn atoms fluctuate between different $(\sqrt{3} \times 2\sqrt{3})$ structures.

It is important to note that the appearance of the $(\sqrt{3} \times 2\sqrt{3})$ is an actual displacive transition. Though the Sn atoms still oscillate around their equilibrium positions, these positions are different in regards to the $(2\sqrt{3} \times 2\sqrt{3})$ ground state, i.e. the Sn atoms have "unbuckled" into a different position. In contrast, the appearance of the $(\sqrt{3} \times \sqrt{3})$ order due to fast fluctuations between the different striped configurations is a process commonly called an order-disorder transition, where the surface only appears as a $(\sqrt{3} \times \sqrt{3})$ lattice over a relatively longer timescale. A "snapshot" of this surface at 300 K would still show a $(\sqrt{3} \times 2\sqrt{3})$ ordered surface. However, what is rare for this system is the existence of BOTH a displacive and order-disorder transition, commonly taken as mutually exclusive (Pérez-mato *et al.* , 2000).

Another interesting observation for this system is the similarity to the process predicted by the Kosterlitz, Thouless, Halperin, Nelson, and Young (KTHNY) theory for 2D melting (Kosterlitz & Thouless, 1973; Halperin & Nelson, 1978; Young, 1979). This theory involves phase transitions of 2D crystals involving a two-step process involving the emergence of topological excitations. The process is defined by the disassociation of dislocation pairs for the first "melting" process into an intermediate phase titled "hexatic". However, this system still contains orientational order. The loss of this orientational order is then led by the disassociation of a second kind of defect, disclinations. Both the solid-to-hexatic transition and hexatic-to-isotropic liquid transition are continuous in the KTHNY theory, though recent simulations on very large systems within the so-called "hard disk model" has predicted a discontinuous/first order transition (Bernard & Krauth, 2011). Our system is not completely analogous to this process as it lacks the 6-fold symmetry necessary by KTNHY theory.

Additionally, it is not strictly 2D due to the existence of a substrate and is in the presence of a host lattice. However, some tenants of the theory remain. The ground state is defined by a solid phase that has quasi-long range positional (translational) order and long ranged orientational order. The system then undergoes an initial transition into an intermediate phase that has short ranged positional order and quasi-long ranged orientational order. Both positional and orientational order of the striped phase then become short ranged, which defines the second transition into an isotropically melted system. The first transition appears to be of second order (continuous), while the second appears discontinuous (from both visual evidence of phase coexistence and the behavior of the area fraction order parameter). These similarities make this system highly unique in its ability to observe the 2D melting process atomically.

3.5 ARPES on the K/Sn/Si(111) system

Kagome systems are particularly interesting due to possible emergent phases of matter due to high electron correlations in the presence of partially filled bands. Similarly to the previously discussed triangular Sn/Si(111) surface, the balance between kinetic energy and the Coulomb interaction for this lattice can lead to collective electronic behavior that could result in unconventional magnetism, charge or spin density wave instabilities, unconventional superconductivity, and/or quantum spin liquids (Bilitewski & Moessner, 2018).

The bandstructure calculated for a Kagome lattice is composed of two bands that cross at a Dirac point, in addition to a band that is completely flat (Figure 3.29(a)). This is direct result of geometric frustration and electron confinement. This geometric frustration is due to a kinetic energy effect that leads to a 'macroscopically quasi degenerate low-energy structure', resulting in non-trivial low energy states (Sutherland, 1986; Plat *et al.* , 2018). The concept behind this geometric frustration can be visualized in Figure 3.29(b) (Kang *et al.* , 2020). In short, due to opposite phases of the electronic states on neighboring sites of the internal hexagon within the kagome lattice, the electronic states will be confined within this hexagon. More specifically, the hopping of electrons to the next cell along the chained triangles of the kagome lattice is forbidden due to destructive phase interference of

the wavefunction. This 'kinetic energy frustration' results in a dispersionless flat band due to the electronic localization.

One way of deducing geometric frustration in a Kagome-ordered system includes performing a detailed study of the electronic bandstructure using ARPES. These flat bands should be observed due to the strong correlations that lead to highly localized electrons within the Kagome lattice (Li *et al.* , 2018; Bilitewski & Moessner, 2018; Iglovikov *et al.* , 2014; Kauppila *et al.* , 2016). However, when dealing with real systems, the system will stray from the ideal two-dimensional Kagome ground state. This is due to several factors, such as interlayer coupling due to the presence of a substrate, hopping beyond the nearest neighbor, multiorbital effects, etc. (Kang *et al.* , 2020). So far, ARPES experiments have been performed on several layered kagome systems such as Fe_3Sn_2, $Co_3Sn_2S_2$, and CoSn, where only the latter has been able to resolve all three bands (Liu *et al.* , 2019; Ye *et al.* , 2018; Kang *et al.* , 2020). Though other surface kagome systems exist, this one is unique in that it is strictly 2D in nature. This provides a unique platform for studying a kagome lattice that is closer to the ideal case. The possibility of realizing these flat electronic states could be a large step towards engineering and realizing novel correlated physics within a geometrically frustrated platform.

The samples were grown and measured in-situ by transferring through our state-of-the-art coupled LT-STM/ARPES system as described in Section 2.1. The process to transfer the sample to the ARPES location is delicate for these K/Sn/Si(111) samples, as fast thermalization of the as-grown sample can quickly degrade the surface. Therefore, great care was taken to reduce the transfer time of the samples from the LT-STM location to the ARPES manipulator, ensuring that the sample spends as little time as possible outside of contact with a cold cryostat (transfer times were typically on the order of 5 minutes).

Sample quality was first checked by STM at 77 K to ensure consistent samples across various experimental runs. The surface quality was then checked after the transfer by LEED as shown in Figure 3.30(a). The (1×1), $(\sqrt{3} \times \sqrt{3})$R30°, and $(2\sqrt{3} \times 2\sqrt{3})$R30° diffraction spots are connected by dashed lines and are colored in black, red, and blue, respectively. In Figure 3.30(b), the surface Brillouin zone is marked for each. LEED was also taken

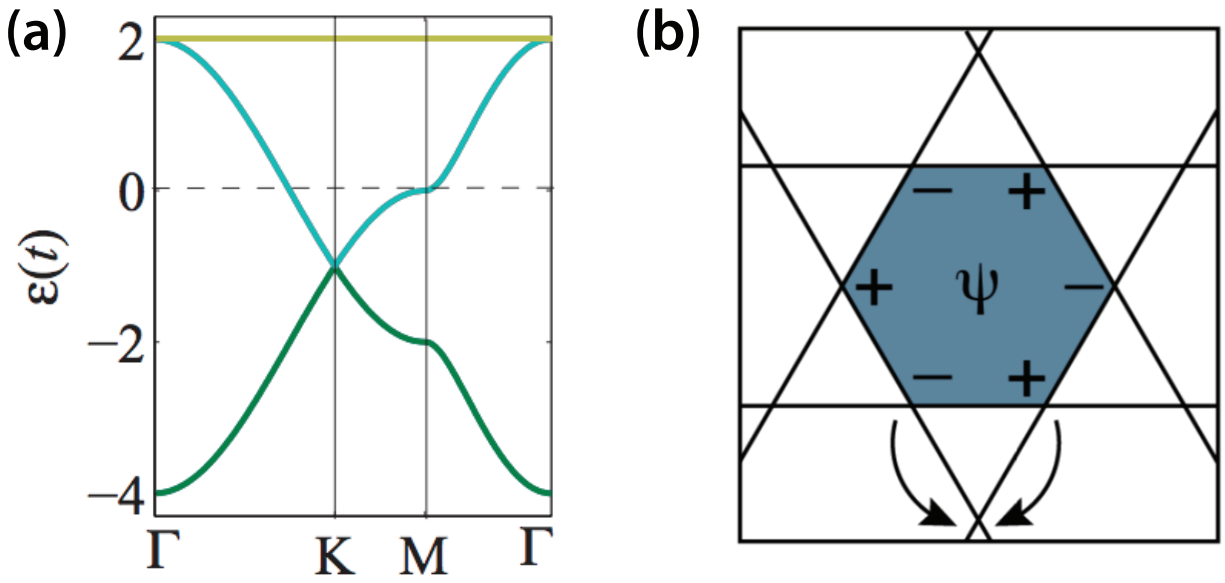

Figure 3.29: (a) Tight binding dispersion for a Kagome lattice. The dashed line is the Fermi level corresponding to "van Hove filling" where the Fermi level intersects a saddle point in the Dirac bands. Taken from Wang *et al.* (2013) (b) Electron confinement within the kagome lattice. The phase of the electron eigenfunctions is indicated by plus and minus signs. The arrows indicate that hoppings outside of the internal hexagon will be cancelled due to destructive interference, which localizes the electron within the hexagon. Figure borrowed from Kang *et al.* (2020).

after ARPES measurements to ensure the quality of the surface did not degrade during the measurement.[‡]

Figures 3.31(a) and 3.31(b) show the band structures of the $(2\sqrt{3}\times 2\sqrt{3})$-K surface along the $\bar{\Gamma}\bar{\mathrm{K}}$ and $\bar{\Gamma}\bar{\mathrm{M}}$ directions, respectively. What appears to be a weakly dispersing surface band is located ∼300 meV below the Fermi level, showing the most dispersive behavior between the $\bar{\mathrm{K}}$ and $\bar{\mathrm{M}}$ points of the $(2\sqrt{3}\times 2\sqrt{3})$ lattice. Unfortunately, this surface band seems to completely disappear in higher Brillouin zones, which we attribute to strong matrix element effects on the spectral weight of the surface band in this region (Moser, 2017). Due to this observation, photoemission spectra were collected across several Brillouin zones. The surface band appears again in higher zones near the limits of our angular range.

[‡]This experiment was performed in collaboration with Dr. Norman Mannella's group. Kaleb McClure performed the ARPES measurements while Dr. Paolo Vilmercati performed the data analysis and fitting. Here we only mention the key observations.

A closer analysis of the surface band is performed by directly comparing the spectra collected in different Brillouin zones along the high symmetry points. Figure 3.32(a) shows that a surface band at $\bar{\Gamma}$ in the first zone is clearly visible, whereas the higher zones do not contain much spectral weight at $\bar{\Gamma}$. However, the features along the $\bar{\mathrm{K}}\bar{\mathrm{M}}$ directions are much more complex. Three different bands can be seen from the spectra within the three different zones, as can be observed from the different dispersions and energetic locations of the band maxima. Specifically, at $\bar{\mathrm{K}}$ the bands visible in the 2$^{\mathrm{nd}}$ and 3$^{\mathrm{rd}}$ zone crosses each other but the different dispersions clearly show that there are at minimum two bands around 0.8 eV. This is supported by an analysis of the different zones along the $\bar{\Gamma}\bar{\mathrm{M}}$ direction in 3.32(b). Two bands are clearly distinguishable at ∼500 meV (1$^{\mathrm{st}}$, 4$^{\mathrm{th}}$, and 5$^{\mathrm{th}}$ zone) and ∼700 meV (2$^{\mathrm{nd}}$, 3$^{\mathrm{rd}}$, and 6$^{\mathrm{th}}$ zone).

It is clear that what appears to be a single surface band at first glance is indeed composed of several bands. From the electron count in the STM data, there should be three total. Indeed, DFT results using the PBE0 hybrid functional calculated by the Ortega group (Smith *et al.* , 2020) shows three weakly dispersing bands below the Fermi level, with one

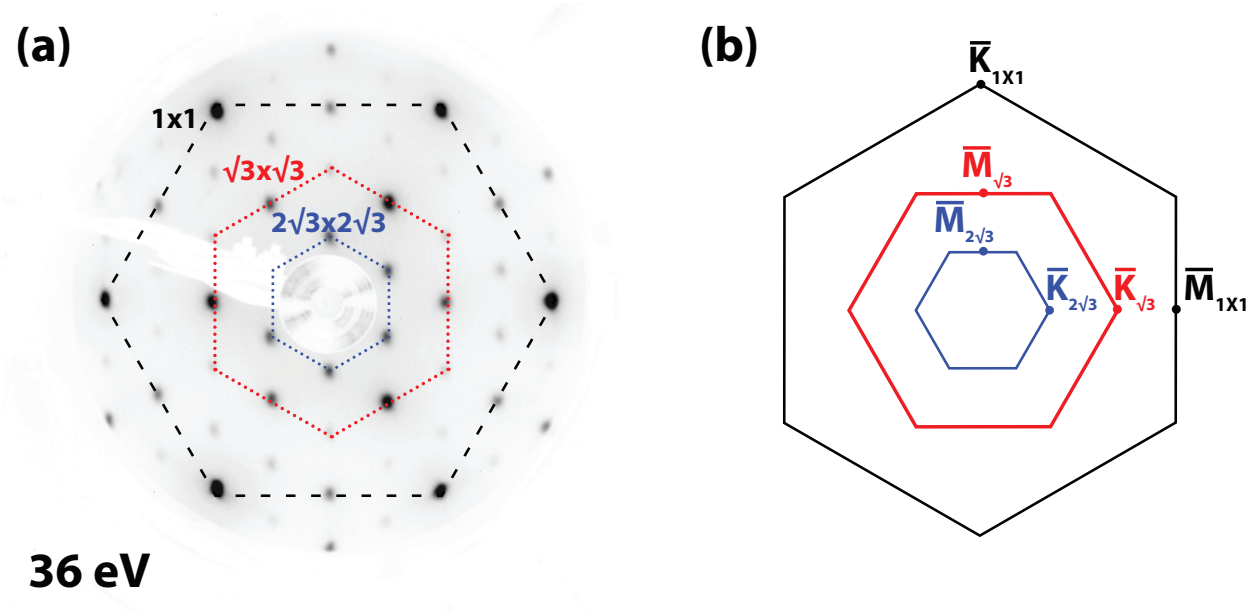

Figure 3.30: (a) LEED image taken at 77 K on the n-type sample. (b) Surface Brillouin zone of the three reconstructions in this system, with the high symmetry points indicated.

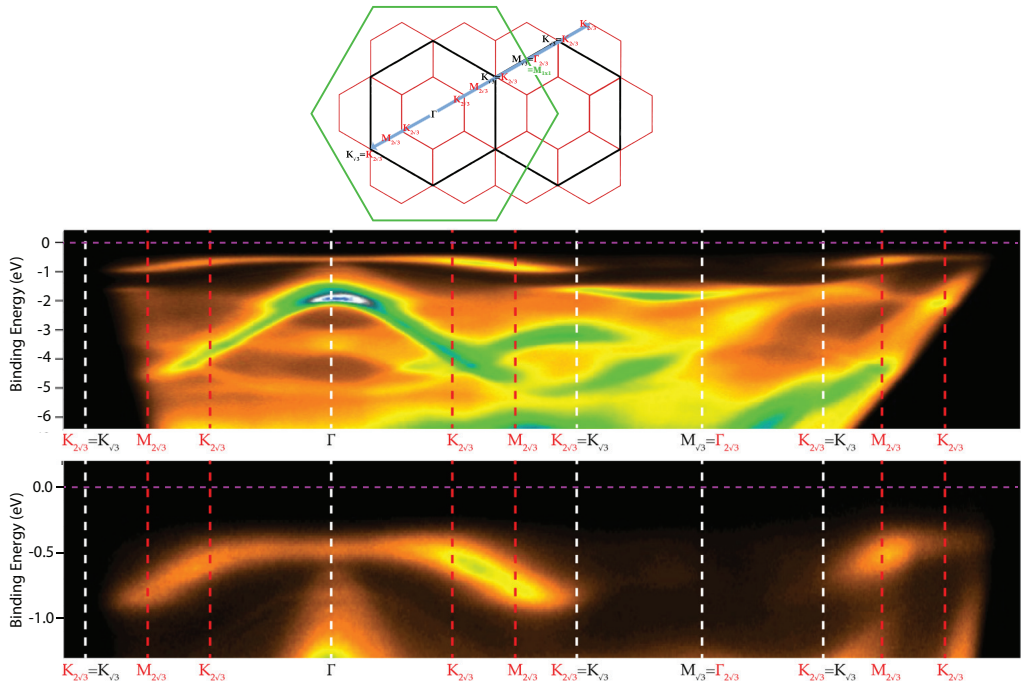

(a)

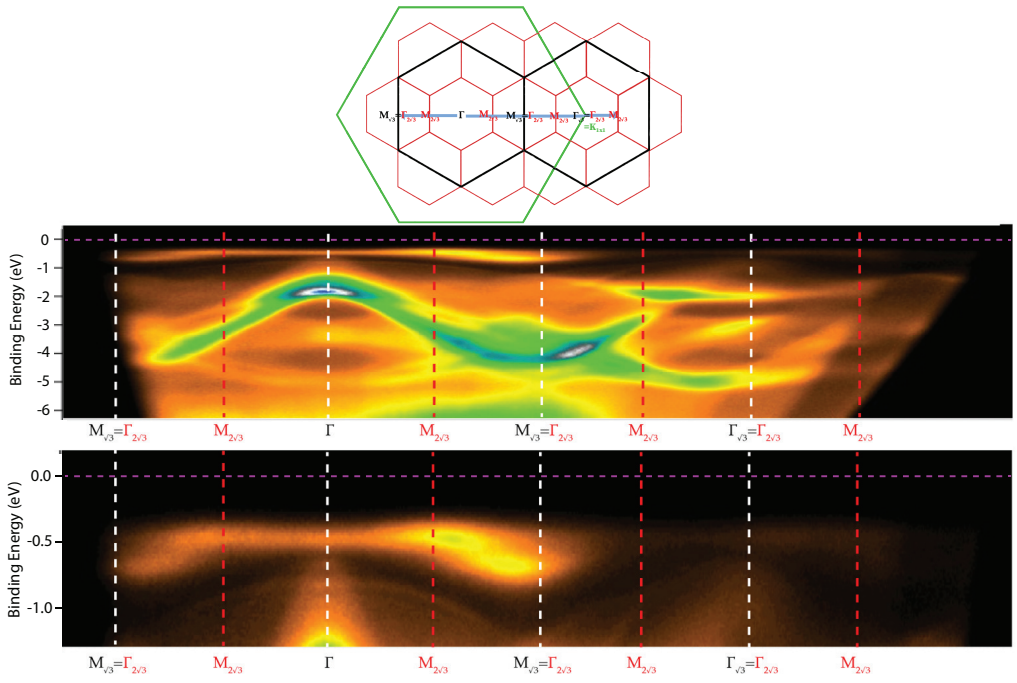

(b)

Figure 3.31: (The ARPES spectra of the $(2\sqrt{3} \times 2\sqrt{3})$-K surface on Si(111) along the (a) $\bar{\Gamma}\bar{K}$ and (b) $\bar{\Gamma}\bar{M}$ directions. Symmetry points of the $(2\sqrt{3} \times 2\sqrt{3})$ unit cell are marked by vertical dashed lines; those that share symmetry points with the $(\sqrt{3} \times \sqrt{3})$ symmetry points are colored white. The Fermi level is marked by the violet line. A schematic of the region in reciprocal space is given at the top, which covers several Brillouin zones.

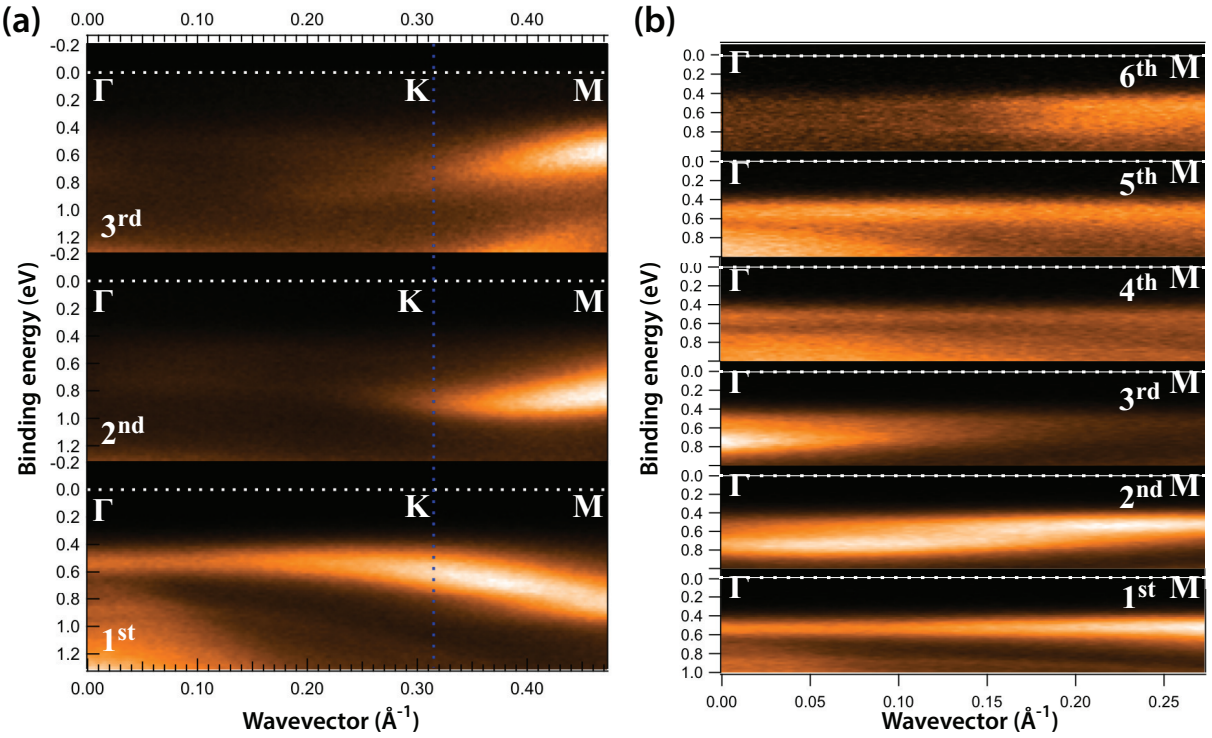

Figure 3.32: Stacked ARPES spectra at the (a) $\bar{\Gamma}\bar{\mathrm{K}}$ and (b) $\bar{\Gamma}\bar{\mathrm{M}}$ symmetry points within different Brillouin zones. No data manipulation is applied.

unoccupied band above (corresponding to the atoms on the triangular, or down, Sn atoms). This is shown in Figure 3.33.

In order to fully identify the number and full dispersion of the surface bandstructure, further work must be completed. A full fitting analysis can possibly be performed within a polaronic model due to the close relationship between the electronic filling of the dangling bonds and the structural degrees of freedom. Due to the very close energy levels of these bands, this requires a very careful analysis of the surface bandstructure at all high symmetry points. As of the writing of this work, this is an ongoing investigation.

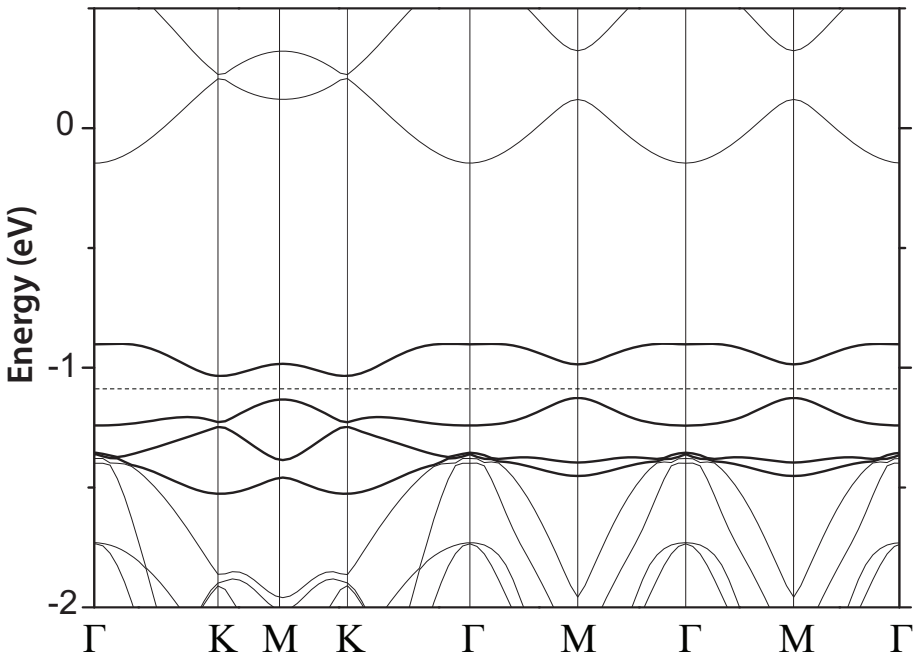

Figure 3.33: DFT bandstructure of the $(2\sqrt{3} \times 2\sqrt{3})$-K, revealing 4 total surface bands corresponding to the Sn atoms (bold lines). There exist three unoccupied bands below the Fermi level, and one occupied above.

3.6 K/Pb/Si(111): A Preliminary Study

To check whether the charged ordered $(2\sqrt{3}\times 2\sqrt{3})$-K structure could form in other α phases of the triangular adatom lattices, a similar experiment is conducted on the (3×3)-Pb surface (described in detail in Chapter 4). Indeed, with the same deposition of 1/6 ML K atoms on top, the surface structure is changed to the $(2\sqrt{3} \times 2\sqrt{3})$-K structure, identical to the structure found on $(\sqrt{3} \times \sqrt{3})$ -Sn surface.

STM topography images summarizing this surface is shown in Figure 3.34. Panel (a) shows a large scale image of the K-decorated surface. The (3×3)-Pb is fully converted to the charge ordered reconstruction, and interestingly the surrounding $(\sqrt{7} \times \sqrt{3})$ domains have converted into another reconstruction, labeled $(\sqrt{7}\times \sqrt{3})$-K. Small patches with higher K coverage appear near the $(2\sqrt{3} \times 2\sqrt{3})$-K boundaries, labeled as HC-K. Identical to the charge ordered surface on the Sn/Si(111) system, the three sublattices appear as a function of

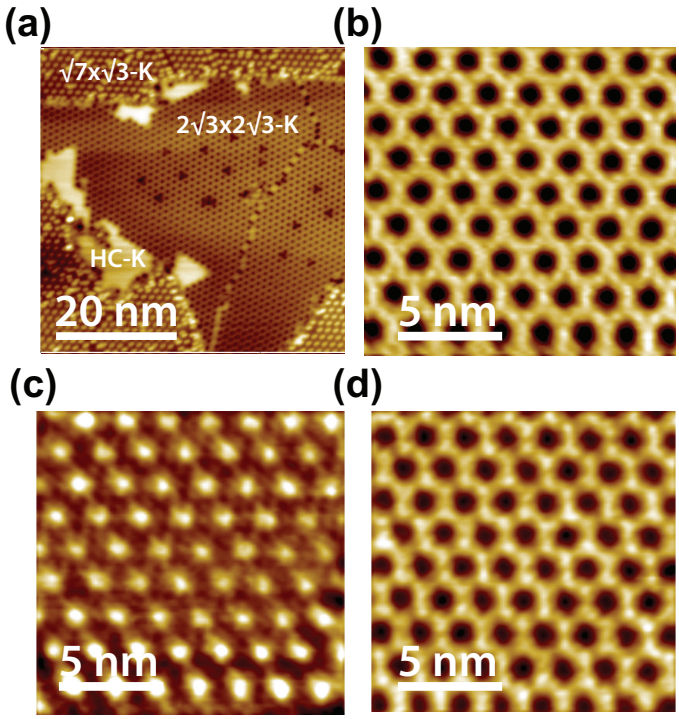

Figure 3.34: (a) Large scale STM image of the (3×3)-Pb surface with 1/6 ML K adsorbed, obtained at 77 K. Neighboring $(\sqrt{7}\times\sqrt{3})$ domains have also been converted into a new phase due to the presence of K adatoms, labeled as $(\sqrt{7}\times\sqrt{3})$-K. (b-c) Small scale STM images of the K-decorated (3×3)-Pb surface. Images are scanned at (a) -1.5 V 30 pA (b) -1.23 V 30 pA (c) 0.15 V 30 pA (d) 1.16 V 30 pA. (e) STS of the $(2\sqrt{3}\times2\sqrt{3})$-K structure grown on (3×3)-Pb surface obtained at 77 K. The 77 K STS of the $(2\sqrt{3}\times2\sqrt{3})$-K structure grown on $(\sqrt{3}\times\sqrt{3})$ -Sn surface shown is also plotted with dashed line for a comparison.

bias: kagome (Figure 3.34(b)), triangular (Figure 3.34(c)), and honeycomb (Figure 3.34(d)). However, the observed contrast change between each of these sublattices seems to appear about 300mV lower in energy. This is supported by normalized $\frac{dI}{dV}$ spectra taken at 77 K, as shown by the black curve in Figure 3.35. The DOS is very similar to that on the K decorated Sn/Si(111) surface, except the DOS has shifted to a lower energy by about 0.3 V. Most interesting is the apparent proximity of the Fermi level to the peak corresponding to the down Pb atoms at $\sim$+100 meV, indicating a possible metallic ground state. However, as this data is taken at the 77 K, there is the possibility that the peak is located above the FL, and just thermally broadened.

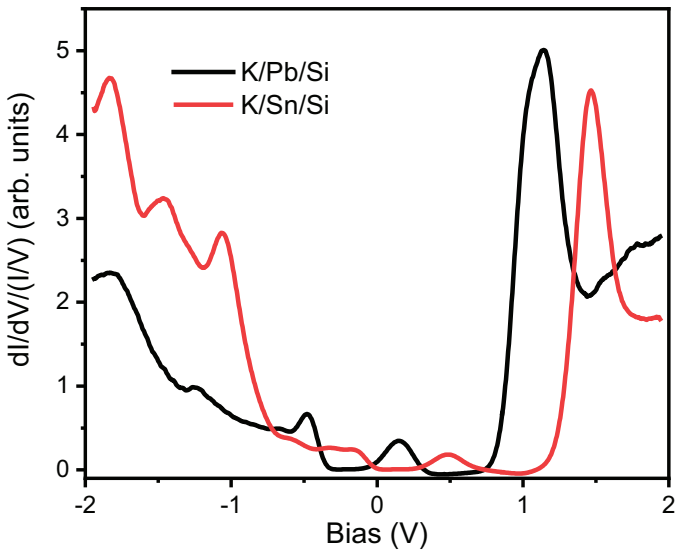

Figure 3.35: Normalized $\frac{dI}{dV}$ of the $(2\sqrt{3} \times 2\sqrt{3})$-K structure grown on (3×3)-Pb surface obtained at 77 K. The 77 K STS of the $(2\sqrt{3} \times 2\sqrt{3})$-K structure grown on $(\sqrt{3} \times \sqrt{3})$ -Sn surface shown is also plotted in red line for a comparison.

Unfortunately, attempts to measure this surface at 4 K return inconclusive results. Figure 3.36(a,b) contains STM topography images of a $(2\sqrt{3} \times 2\sqrt{3})$-K domain at two different biases. Not only are the domain boundaries in the filled state image more disordered, the HOMO-LUMO gap varies significantly across the domain Figure 3.36(c). The gap is as large as 2.0 eV in the middle of the domain, where the edges of the domain have gap as small as 0.3 eV, similar to the gap observed at 77 K. However, the spectra also appears to be rigidly shifted by $\sim$+0.2 eV. Possible explanations for this effect is that the $(2\sqrt{3}\times 2\sqrt{3})$-K domains have very limited conductivity at 4.5 K, while the neighboring $(\sqrt{7} \times \sqrt{3})$-K domains are more effective in draining the tunnel current. This could be due to band bending below the different surface domains, leading to lateral variations of the surface potential. This could possibly be combined with tip induced band bending effects in the $(2\sqrt{3} \times 2\sqrt{3})$-K domains (McEllistrem *et al.* , 1993; Stroscio *et al.* , 1988).

Regardless, it remains clear that the potassium adatoms form the charge ordered ground state on the α phases on Si(111) substrates in the same manner. The striking result of an identical morphology and electronic structure with only a rigid shift due to the different atomic species makes this surface highly desirable to grow on the other two systems in this

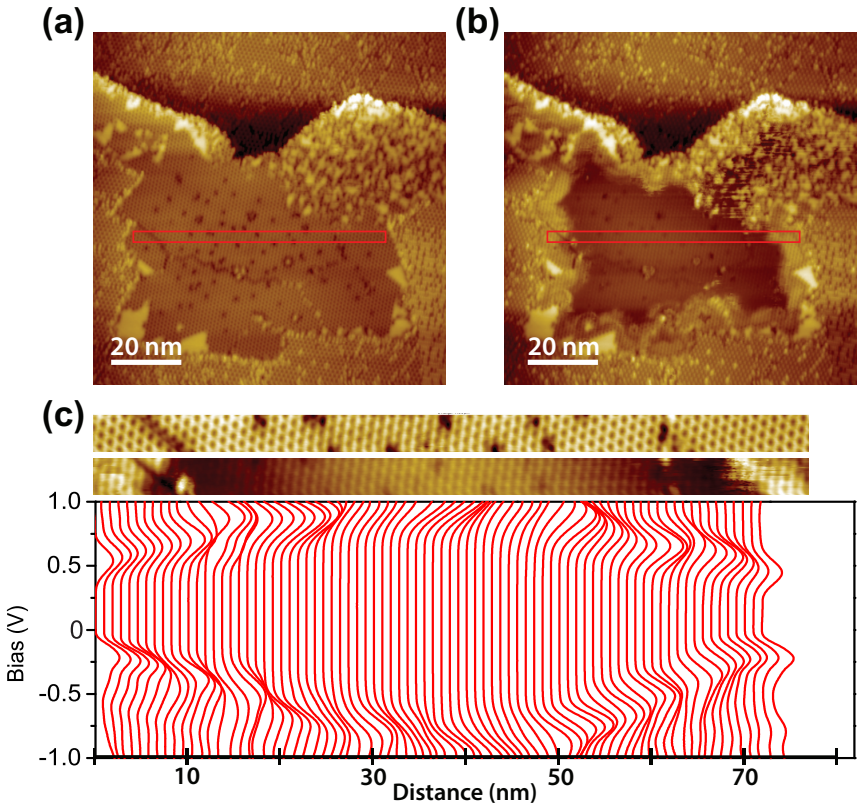

Figure 3.36: STM images measured in the filled (a) and empty (b) states on the Pb/Si(111) surface with 1/6 ML K, taken at 4.5 K. The charge ordered domain appears inhomogeneous in (b) near the domain boundaries. (c) $\frac{dI}{dV}$ spectra taken across the domain (marked as red rectangles in (a),(b)) showing that the DOS is vastly inconsistent. Tunneling parameters are (a) -1.5 V 30 pA and (b) +1.5 V 30 pA.

family of surfaces: Sn and Pb on Ge(111). The intriguing prospect of a flat-band metallic kagome system on either of these surfaces could lead to possible quantum spin liquid or even unconventional superconductivity (Wen *et al.* , 2019b).

3.7 Conclusion

The goal of this experiment was to electron dope the Si(111)-($\sqrt{3} \times \sqrt{3}$) R30°-Sn in an attempt to further explore the electronic phase diagram of a 2D Mott insulator. Surprisingly, the potassium adatoms had a preferential absorption site in the lattice, inducing a charge

ordered phase. Though this did not directly dope the surface, as intended, it did produce insightful results into the role of the adatom dynamics on the stability and melting of the charge ordered $(2\sqrt{3} \times 2\sqrt{3})$-K phase. In addition, it revealed atomistic insights into the process of 2D sublattice melting. ARPES studies indicated the presence of multiple surface state bands associated with the Kagome sublattice. The bands have very small dispersions and are all located just below the Fermi level. This suggests the possibility of creating unconventional magnetism or superconductivity through additional hole doping. Finally, potassium doping experiments on the sister Pb/Si(111) surface reveals a very similar charge ordered reconstruction with a rigid shift of the electronic structure, motivating further attempts on the other α-phases on Ge(111).

Chapter 4

Growth and Characterization of the Pb/Si(111) surface

4.1 Introduction

The study of electronic Coulomb correlations within adatom surface systems has been a strong area of study in condensed matter physics for many years. Specifically, the strong relationship between electronic interactions, charge delocalization, and structural instabilities remains a large focus in these types of materials. As mentioned in the previous chapter, metallic adatom species on Si(111) are good candidates for observing such an interplay. The focus of this chapter will be Pb deposited onto the Si(111) surface, which is isoelectronic with the Sn/Si(111) surface system. However, whereas the Sn case is a Mott insulator, adsorption of the heavier and more polarizable Pb atoms produces a 3x3 charge-ordered metallic phase, posited to be due to more heavily screened Coulomb interactions resulting in a lower Hubbard U (Hansmann *et al.* , 2013). This surface does not undergo a superconductive transition at low temperature, at least not above 4.5 K. The charge ordered ground state is characterized by a vertical buckling and tripling of the unit cell (Ortega *et al.* , 2002). However, the exact buckling pattern of the unit cell has long been in debate (Cortés *et al.* , 2013). Additionally, the heavier Pb atoms have been predicted to exemplify Rashba spin-orbit coupling effects (Tresca *et al.* , 2018). Figure 4.1 shows the calculated bandstructure from Tresca et al.. Here, the spin orbit coupling and Hubbard splitting are similar in magnitude and thus important

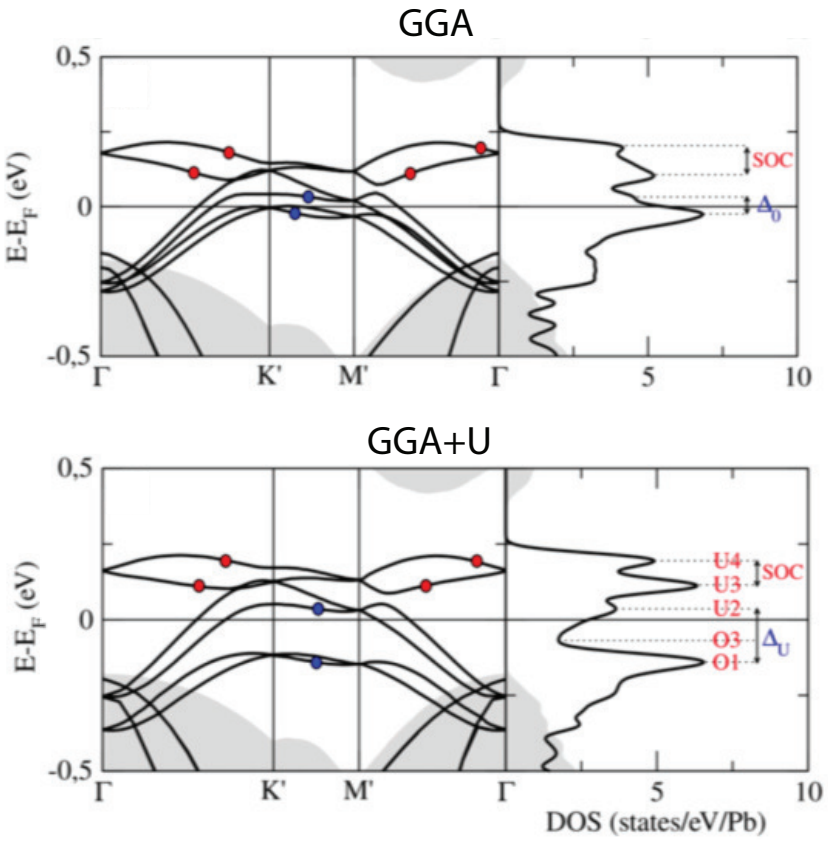

Figure 4.1: Fully relativistic electron structure for (a) $U = 0$ eV and (b) $U = 1.75$ eV for the Si(111)(3×3)-Pb surface (Tresca *et al.* , 2018).

to a complete understanding of the 3x3 ground state itself. This makes for an ideal system to study electronic correlations and spin orbit effects through careful STS, QPI, and magnetic scattering.

The Pb/Si(111) system itself has not been studied extensively in the past due to morphological difficulties, as the 1/3 ML reconstruction is unstable for larger domains. Therefore, a true study of the morphology and electronic structure of this system is limited to experimental methods that are sensitive in the nanoscale, limiting the study of this surface to STM and STS methods. As described extensively in Section 3.2, it is clear that these systems are highly sensitive to electronic composition (doping), as removing or adding electrons from Pb dangling bonds could possibly suppress or enhance the charge order buckling due to orbital rehybridization. Following the success of previous modulation

doping results, it is worth an attempt to grow this surface in a similar fashion, i.e. on various substrate doping types. However, as will be shown, the surface morphology is highly sensitive to the doping level of the Si substrate, which complicated the interpretation of our data. Instead, by optimizing the growth of the undoped system, we were able to acquire Quasiparticle Interference Images (QPI) that provide a critical test of the GGA+U bandstructure calculations for this interface by Tresca *et al.* (2018). Our STS data also provided strong evidence for a *1 up 2 down* buckling pattern, in strong contrast to the recent interpretation by Adler *et al.* (2019) that claimed a 2 up 1 down pattern. Possible evidence for spin split surface state bands will then be provided by using magnetically active impurities to access forbidden backscattering channels.

Section 4.2 contains the deposition rate calibration, growth optimization, structure details, and work on other substrates. Section 4.3 includes the results of the QPI study. Section 4.4 describes the growth and QPI of the system with magnetic scattering centers.

4.2 Sample growth

4.2.1 Deposition rate calibration with XPS and STM

Preliminary growth of the Pb/Si(111) system was initially performed in the Growth and XPS chamber as described in Section 2.1. The deposition rate of Pb was calibrated by measuring the evolution of the Pb and Si core level intensities as a function of deposition time using XPS. Pb was deposited onto the clean Si(111) 7x7 surface, and the Si $2p$ and Pb $4d$ peaks were measured. The sample was then flashed to 1200° C and Pb was then deposited again. This was repeated for a range of deposition times at room temperature. Pb growth on this surface follows the Stranski-Krastanov mechanism in which 3D islands begin to nucleate after the first 2D monolayer is completed (Özer, 2006). From this knowledge, the intensity of the Pb $4d$ core level spectrum will initially be proportional to the number of Pb atoms in the first layer, and thus the signal should increase linearly until the 2D layer is completed. The XPS intensity will continue to increase upon deposition of a second or third layer but with reduced slope, as the photoemission intensity from the first monolayer

will be attenuated by a factor $\exp(-d/\lambda)$ (where d is the thickness of the Pb overlayer(s) and λ the mean free path of the Pb $4d$ photoelectron). Likewise, the intensity of the Si $2p$ core level signal will be attenuated exponentially by the Pb overlayer, but the mean free path of the Si $2p$ photoelectron will be different. In practice we measure the ratio of the Pb $4d$ and Si $2p$ core level intensities as a function of deposition time, which eliminates many of the experimental uncertainties related to, *e.g.*, precise sample positioning, fluctuations in the x-ray flux, etc. When plotting the intensity ratio as a function of deposition time, one observes a clear king at the completion of the first physical monolayer or 'wetting layer'. Our calibration procedure is based on the fact that 3D islands are formed on top of the Pb wetting layer, which has an absolute coverage of 0.65 ML Pb, where 1 ML = 9.43×10^{14} atoms/cm^2 (Mans *et al.* , 2005; Tanaka *et al.* , 1996). The raw data and intensity ratios are plotted in Figure 4.2. A very clear kink is seen in panel (b), corresponding to a deposition rate of ∼0.32 ML/min.

After the preliminary determination of growth parameters was understood within the Growth and XPS chamber, the growth process was then moved to the newer Coupled LT-STM/ARPES chamber (Section 3.2). As this required use of a new effusion cell and manipulator, an independent coverage calibration of this system was performed for consistency. Due to the lack of a photoemission spectrometer in this chamber, calibration was performed in a different manner. This process involves depositing several monolayers onto the Si(111) surface at room temperature, and then measuring the surface morphology at 77 K by STM. The 2D wetting layer can be observed at approximately 0.65 ML, followed by the formation of islands within the re-entrant bilayer-by-bilayer (RBBB) mode (Özer *et al.* , 2005; Michailov, 2011; Yakes & Tringides, 2011). As a result, these islands appear on the surface in discrete height intervals, allowing a volumetric calculation of the overall Pb coverage. Figure 4.3 shows the Pb/Si(111) surface after depositing for several minutes. The overall deposition rate is then calculated to be ∼0.55 ML/min. The deposition time is then adjusted to ensure the same conditions for sample growth between the two systems.

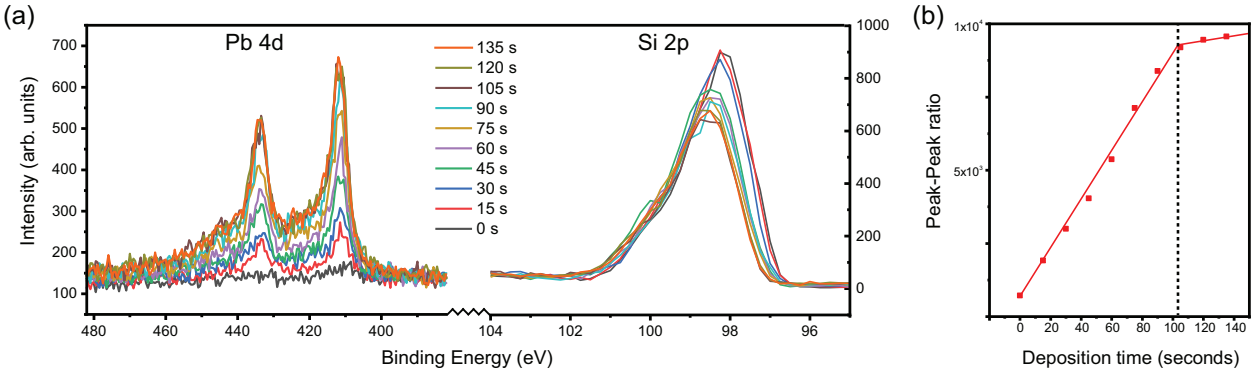

Figure 4.2: (a) Pb 4d and Si 2p core levels for different deposition times as measured by XPS. The ratio of the peak intensities (calculated by integrating the peaks) is given in panel (b). A clear kink is seen at 103 seconds upon the saturation coverage at 0.65 ML Pb.

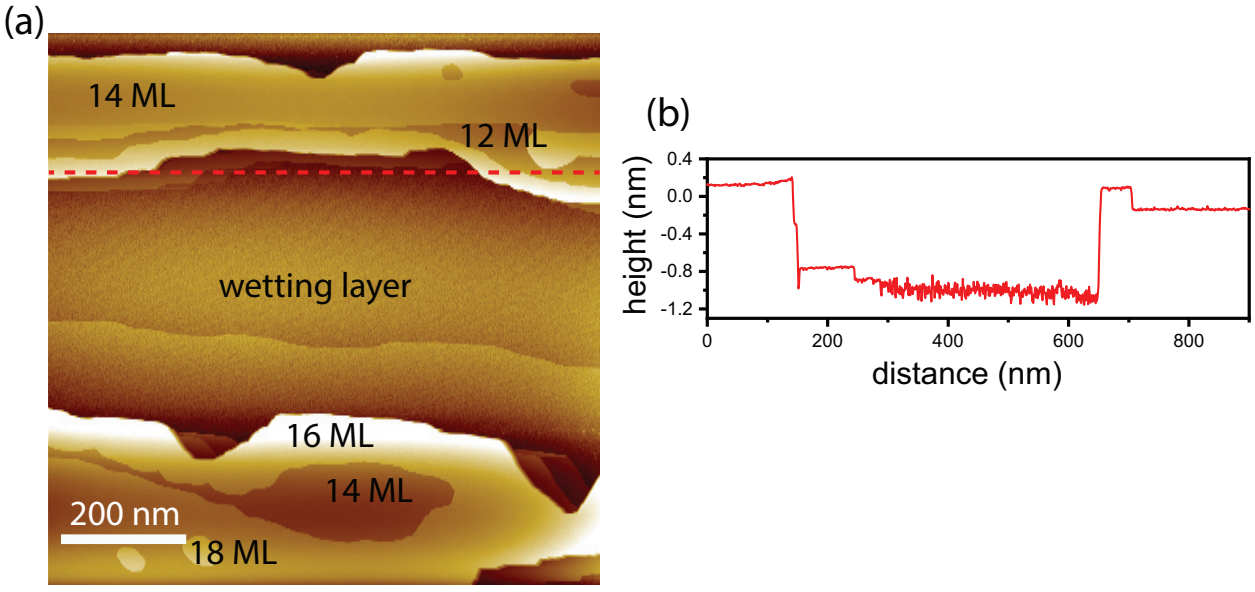

Figure 4.3: (a) STM topography image on the Si(111) surface after depositing Pb for 20 minutes. A majority of the surface is composed of the wetting layer. The island heights are used to determine the absolute coverage. (b) Line profile across the STM image (marked as a red dashed line in (a)), showing an apparent bilayer Pb height of $\sim$.21 nm.

4.2.2 Optimization of growth on the undoped surface

Growth of the 1/3 ML Pb/Si(111) surface begins with the preparation of Si(111) wafers as mentioned in the first paragraph of Section 3.3. For initial growth studies, this was done in the Growth and XPS chamber, but all data shown in this work will be from samples grown in the LT-STM/ARPES coupled chamber. The clean and well-ordered Si(111) substrates are then brought to the growth position onto a transfer arm located within the LT-STM chamber, and are held at room temperature. About 1.5 ML Pb is then deposited from a SciCam low temperature effusion cell held at 480° C (outfitted with a PBN crucible). This is followed by transferring to the metal MBE chamber and annealed at around 400° C for less than one minute.

Figure 4.4 shows the surface grown under three different annealing temperatures on the n-type Si(111). The surface coverage of Pb is found to be extremely sensitive to the post-annealing temperature and time, with only minor differences causing a large variation away from the optimal growth conditions. Figures 4.4(a),(b) show the surface after a 46 second annealing at ∼420° C. The surface morphology at this temperature composes of the coexistence of several domains. Most of the surface consists of a high coverage (1.2 ML) striped $(\sqrt{7} \times \sqrt{3})$ domain (Brihuega *et al.* , 2007; Custance *et al.* , 2001; Brochard *et al.* , 2002). In patches and along the step edges, the surface is composed of a diluted phase consisting of a 2D solid solution of Si and Pb adatoms sitting on the T4 sites on top of Si dangling bonds. This solution can be composed of a variable number of Pb and Si atoms commonly called the mosaic phase, denoted as Si_xPb_{1-x}/Si(111) (Slezák *et al.* , 1999). This is labeled in Figure 4.4(a) as MP, with a zoomed in image shown in (b). As the annealing temperature is decreased to ∼405° C, the $(\sqrt{7}\times\sqrt{3})$ domains increase in size, and the mosaic phase mostly converts into a reconstruction in which every T4 site contains a Pb atom (the mixture of Si and Pb atoms still persists closest to the step edges). This is the $(\sqrt{3} \times \sqrt{3})$ phase (at room temperature), analogous to the Sn $(\sqrt{3}\times\sqrt{3})$ phase in the previous chapter. The optimization of this phase leads to domains as large as 10,000 nm^2, which has so far not been achieved in literature. Figures 4.4(c),(d) show large and small scale images of such a case, respectively. A lower temperature annealing of ∼385° C returns a surface that is

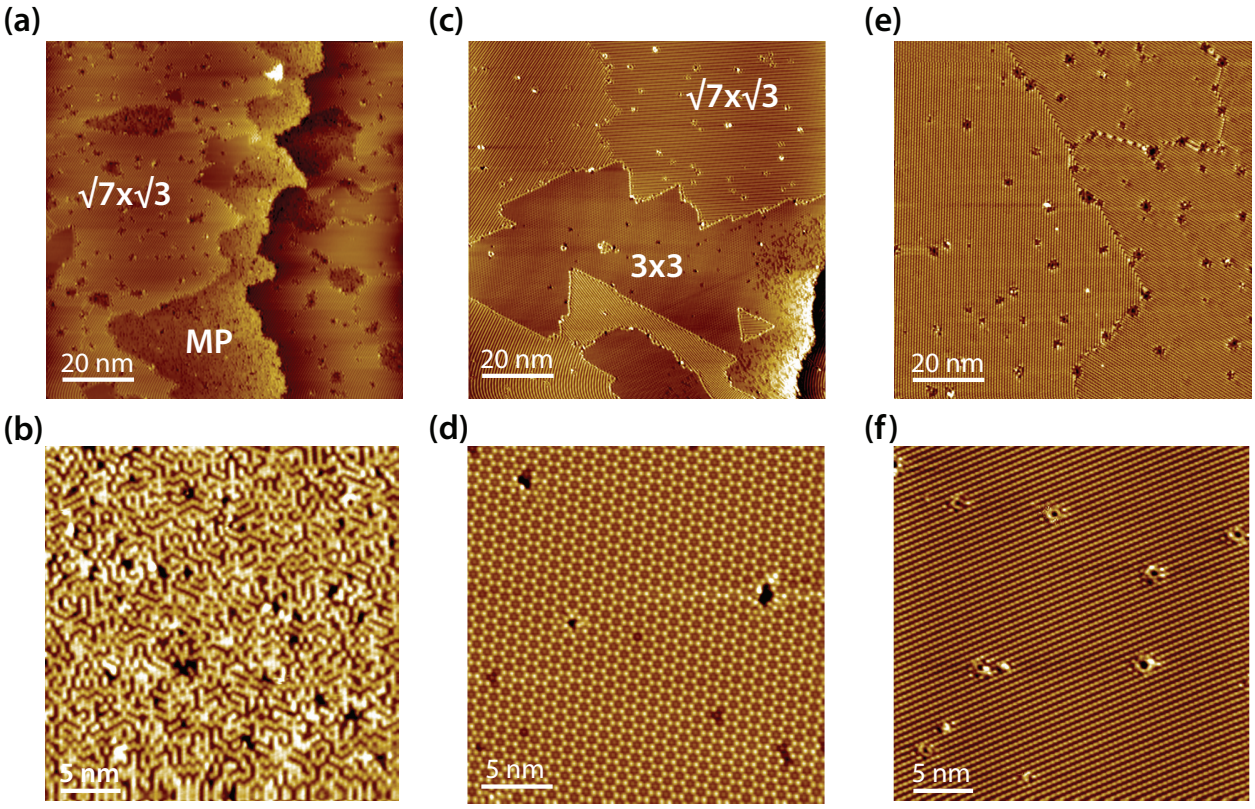

Figure 4.4: STM topography images on surfaces with various annealing temperatures. (a) shows a large scale image of the "overannealed" surface, a small scale image of the mosaic phase on this surface is given in (b). (c) shows a large scale image of the "optimized" surface, with large domains of the 1/3 ML Pb/Si(111) phase. A zoomed in image of the 1/3 ML phase is given in (d). (e) shows the "underannealed" surface, which is entirely composed of the high coverage $(\sqrt{7} \times \sqrt{3})$ Pb/Si(111) phase. (f) is a zoomed in image of (e). The annealing temperatures for the three cases are ∼420° C, ∼405° C, and ∼385° C, respectively. Image parameters are (a) +2.0 V 30 pA (b) +2.0 V 30 pA (c) +1.0 V 30 pA (d) +1.0 V 100 pA (e) +1.5 V 30 pA (f) +1.5 V 30 pA.

fully covered by the $(\sqrt{7} \times \sqrt{3})$ phase. Figures 4.4(e),(f) shows the topography in this case. With these observations, it is possible to reproduce samples with large enough domains of the 1/3 ML Pb/Si(111) phase to ensure that finite size effects such as edge states or strain contributions will not affect a comprehensive study of the ground state properties of this system.

High resolution STM topography images taken at 77 K are given in Figure 4.5. As stated previously, this system exemplifies a charge order transition from $(\sqrt{3} \times \sqrt{3})$ to a (3×3)-Pb

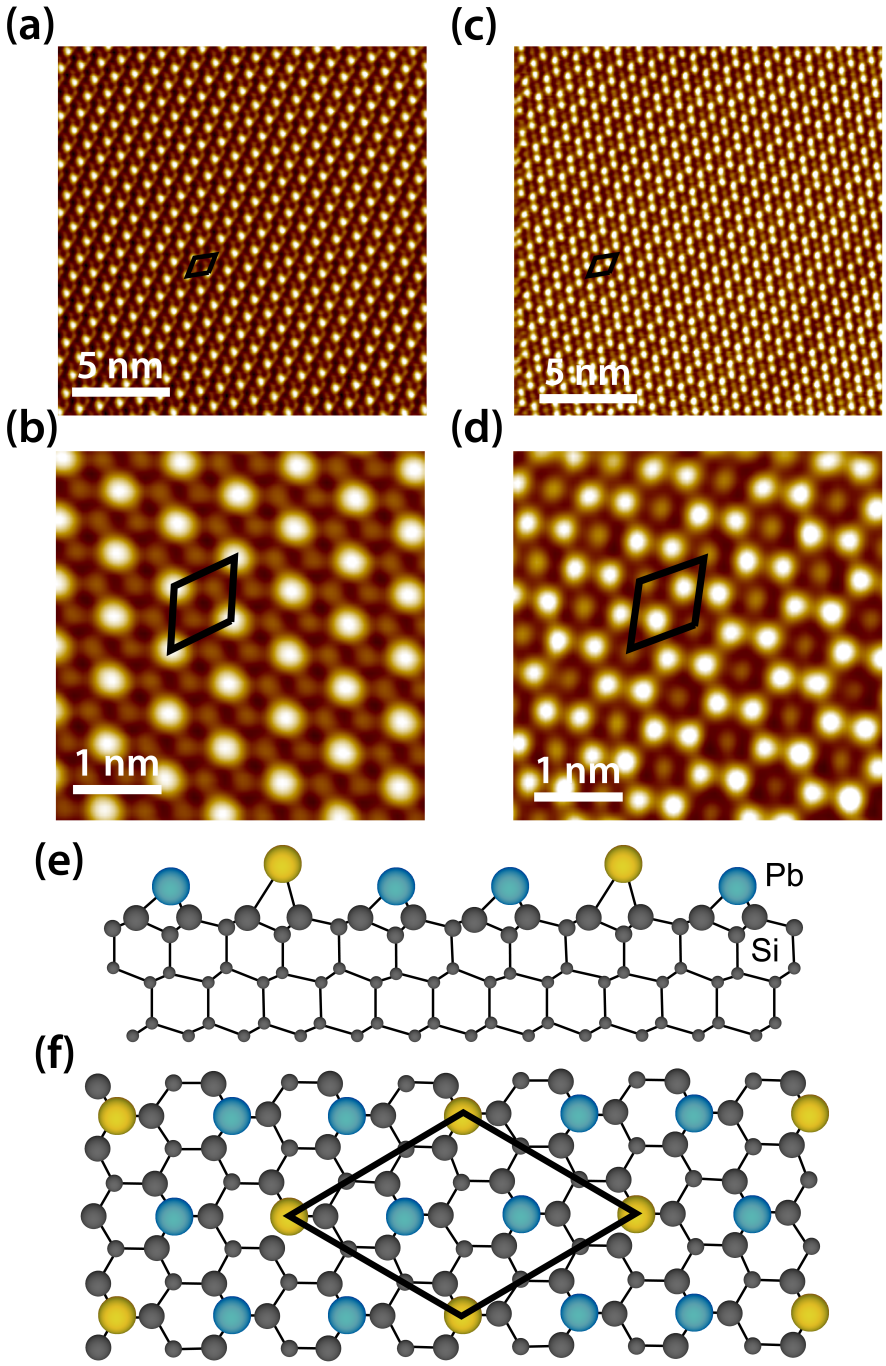

Figure 4.5: STM topography on the (3×3)-Pb surface on the n-type Si(111), forming a triangular lattice in the occupied states (a),(b), and a honeycomb lattice in the unoccupied states (c),(d). Tunneling parameters are -0.5 V 300 pA, -1.0 V 100 pA, +0.5 V 300 pA, and +1.5 V 100 pA, respectively. (e),(f). Atomic ball models (top and side views) for the (3×3) structure. The smaller gray spheres are the Si atoms, the Pb up atoms of the triangular lattice are yellow, and the honeycomb lattice atoms are the light blue spheres. Note the *1 up 2 down* configuration in (e).

reconstruction at 86 K (Brihuega *et al.* , 2005). This reconstruction appears as a triangular lattice in the filled states, and a honeycomb lattice in the unoccupied states. Though the mechanism and the exact structure of the charge ordered lattice is still under debate, this work will later show evidence for the *1 up 2 down* model, where the atoms that make up the triangular lattice are above those of the honeycomb lattice (Cortés *et al.* , 2013; Tejeda *et al.* , 2007). This is shown in an atomic ball model of the (3×3)-Pb reconstruction at the bottom of Figure 4.5.

To further explore the electronic structure of this system, atomically resolved STS was performed on individual atoms of the (3×3)-Pb unit cell. The LDOS of the "honeycomb" atoms is dominated in the unoccupied states, consistent with dangling bonds that contain a lower electron filling. The LDOS of the "triangular" atoms have much more spectral weight

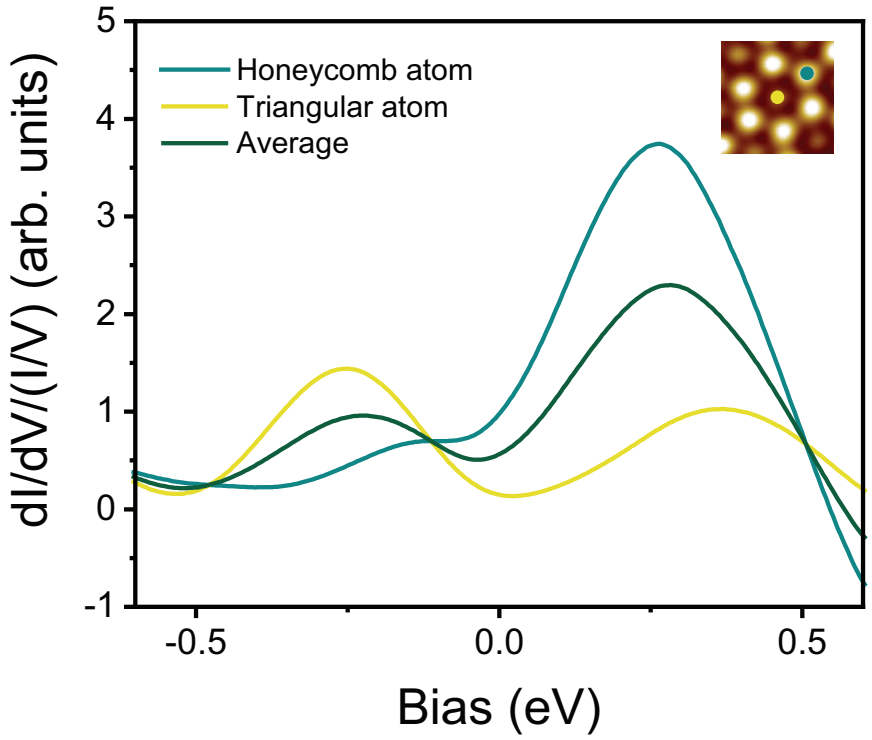

Figure 4.6: Atom-resolved normalized dI/dV spectra, showing a switch of spectral weight between the honeycomb atoms and triangular atoms in the unoccupied and occupied states. The average is taken by performing several STS measurements on different areas of the (3×3)-Pb domain. Inset: STS locations for the atom resolved measurements.

in the occupied states, indicating that these dangling bonds have a higher electron filling. The averaged LDOS from taking spectra on many areas on the (3×3) domains contains both peaks at -0.25 eV and +0.3 eV. The surface is metallic, with a dip near the Fermi level.

With these observations in the LDOS, and by using arguments similar to those for the Sn/Ge(111) systems, a simplistic picture can be drawn for the up-down atom buckling when the on-site U is small (U<W). When an sp^3 hybridized adatom with a nominally half-filled dangling bond orbital acquires extra charge from e.g. a neighboring adatom, the dangling bond charge will repel the Pb-Si backbonds. Accordingly, the backbond angles become smaller (closer to 90 degrees) and the backbonds become more p-like. This orbital rehybridization makes the occupied dangling bond more s-like (and thus lower in energy). Smaller backbond angles in turn increases the adatom-surface distance, leading to the upward relaxation of the Pb adatom. On the other hand, if the gives up charge, it becomes more p_z like while the backbonds become sp^2 like. This leads to a downward movement of the Pb atom (Dávila *et al.* , 2004). For the (3×3) charge ordered lattice, there are three Pb adatoms per unit cel. The up atoms have fully occupied dangling bonds and form a 3x3 triangular sublattice. This leaves one electron to be shared between the two down atoms. The latter form a honeycomb sublattice with two quarter-filled surface state bands, that is, in the absence of a Hubbard U (Ortega *et al.* , 2002). The obvious switch of spectral weight between the hexagonal and triangular atoms continues to support the prevailing theory of the *1 up 2 down* model. (It is to be noted that the up-down buckling distortion is predicted to be enhanced due to the local Coulomb repulsion, but does not affect the principle mechanism responsible for the buckling (Tresca *et al.* , 2018)). It is to be noted that recent works by Adler *et al.* (2019) positing a *1 down 2 up* structure gives a false interpretation of the low bias STM imaging results showing the local LDOS at low bias voltages. In fact, low bias voltages are very sensitive to the local density of states on the surface, and does not give a true picture of the structure. The *1 up 2 down* model still remains the prevailing structure supported by our experimental LDOS.

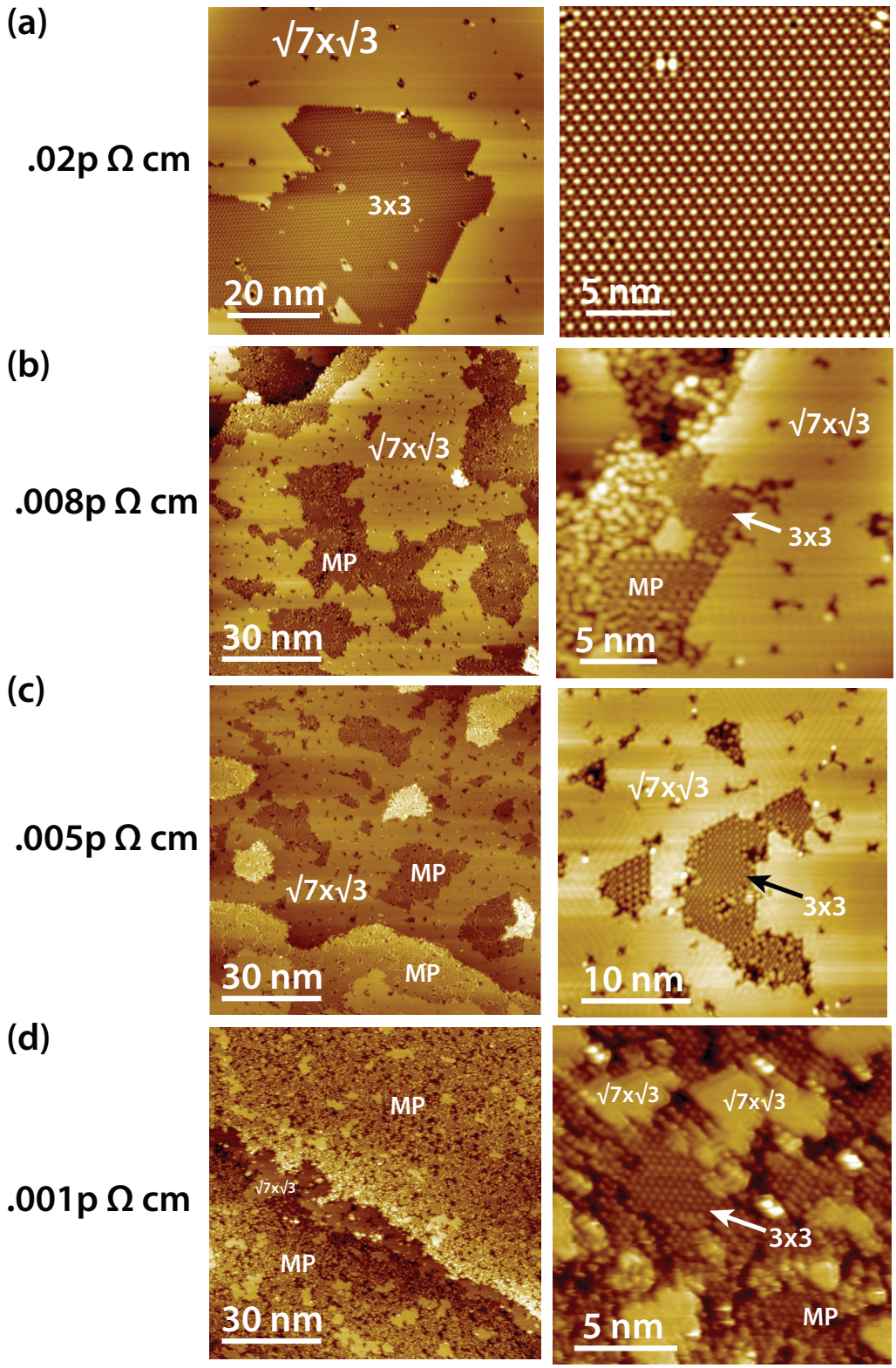

Figure 4.7: Pb grown on substrates with different doping concentrations. Tunneling parameters are (a) left: +1.0 V 30 pA right: +1.5 V 100 pA (b) left: +1.0 V 30 pA right: +1.0 V 30 pA (c) left: +2.0 V 30 pA right: +1.5 V 30 pA (d) left: +2.0 V 30 pA right: +2.0 V 30 pA.

4.2.3 The Pb/Si surface on various substrates

Inspired by the success of the effect of modulation doping on the Sn/Si(111) system, the Pb/Si(111) surface was then grown on various Si(111) substrates. Only one n-type (As-doped) silicon substrate with room temperature (RT) resistivity of 0.002 was implemented in this case, and three p-type (B-doped) substrates with RT resistivities of 0.02, 0.008, 0.005, and 0.001 Ω cm were used. They are labeled according to their resistivity and doping type, for instance, "0.002n" or "0.001p" (smaller numbers represent higher bulk doping levels). The .001p substrate is the highest doping level achievable with our approach (see discussion of this unique surface in section 3.1).

Figure 4.7 summarizes the topography on the p-type substrates (the optimally grown .002n substrate is shown in Figures 4.4 and 4.6). The surface morphology of the optimized .02p samples is given in panel (a). It grows in an identical manner to the .002n substrate, with domains of the (3×3)-Pb reconstruction reaching a similar size of up to 3000 nm^2; the majority of the surface is covered by the higher coverage $(\sqrt{7} \times \sqrt{3})$ reconstruction. Upon growing on the .008p substrate (Figure 4.7(b)), the surface begins to show signs of higher disorder. The $(\sqrt{7} \times \sqrt{3})$ domains begin to shrink in size, and the lower coverage domains begin to appear more diluted (in the same manner as the previously described Si_xPb_{1-x}/Si(111) reconstruction (Slezák *et al.* , 1999)). Areas near domain boundaries still show some sign of small patches of the (3×3)-Pb phase. The .005p substrate (Figure 4.7(c)) shows a similar behavior, with perhaps even more of a preference towards the diluted Pb phase. The right side of panel (c) shows the largest domain found on this surface after searching this surface for several hours. Some (3×3) charge ordering is observed, but the small domain size makes a study of this system quite complicated, as the high defect density and proximity to the high coverage phase tends to cause an inversion or even suppression of the (3×3) ordering. This has been observed previously on surfaces grown on relatively undoped samples with higher defect densities, where the defects are observed to generate an exponentially attenuated modulation with (3×3) symmetry characterized by a decay length which is temperature dependent (Brihuega *et al.* , 2007). Pb grown on the .001p substrate shows even more instability, with domain sizes smaller than 25 nm^2. These small domains

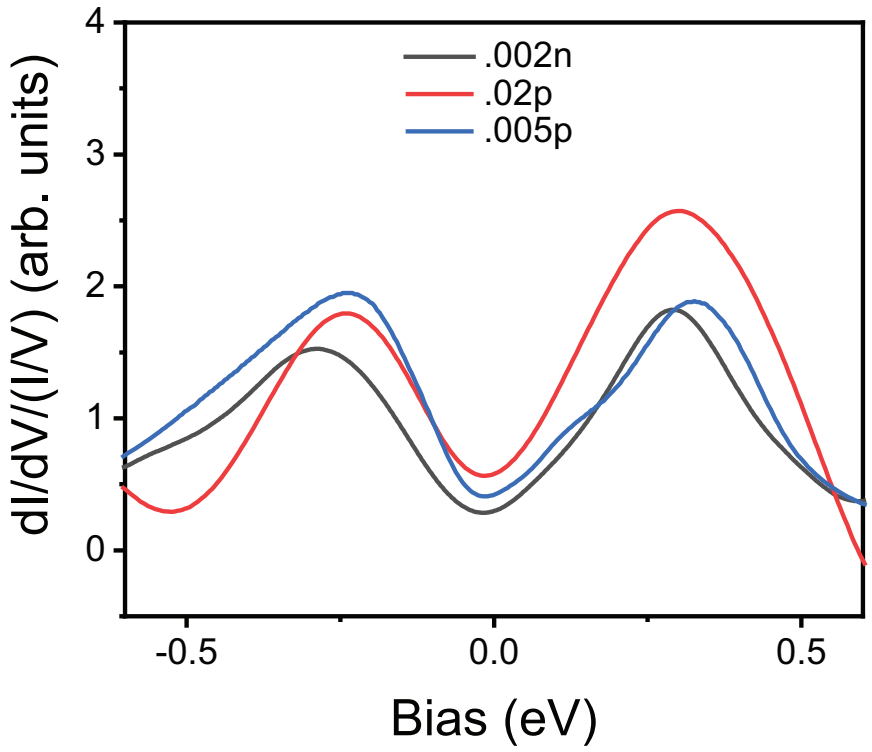

Figure 4.8: LDOS of the (3×3)-Pb reconstruction on three doping types.

completely lack charge order, though whether this is from the role of defects or is a result of doping remains an open question.

Though the domains on the most heavily p-type doped substrate are too small to measure with consistency, the local electronic structure of the .005p, .02p, and .002n (3×3)-Pb domains can still be compared. These results are shown in Figure 4.8. The most obvious difference is a small shift of the features of approximately 45 meV to higher energy upon higher hole doping. However, great caution should be shown drawing conclusions from these observations, as the buckling of the Pb atoms on the .005p surface appears to be strongly affected by the proximity to defects. Qualitatively, the peak positions can be taken as within the error bar of the experiment, which does not produce much variation away from the .002n case. It is clear that the modulation doping approach is not as effective on the Pb/Si(111) α-phase, as expected from the already unstable (3x3) domains on the 'undoped' substrate. It is intriguing that hole doping destabilizes the ordered structure in favor of a more dilute mosaic phase, and warrants future studies of the interplay between substrate doping and

surface reconstruction on this system. Nonetheless, other doping approaches must be taken if the electronic phase diagram is to be explored in a similar fashion to the Sn/Si(111) case.

4.3 Mapping Constant Energy Contours and Dispersion through QPI

The new growth parameters acquired during the morphology optimization of Section 4.2.2, in combination with the metallicity of the (3×3)-Pb reconstruction, makes this system highly accessible by Quasiparticle Interference Imaging (QPI). Specifically, the large domains allows QPI to be performed with high enough resolution to observe weakly dispersing **q**-vectors. The argument goes as follows: the resolution Δq in reciprocal space is determined by the real space length L of the image size, and is given by $\Delta q = 2\pi L^{-1}$. However, to choose a correct sampling rate, one must employ the Nyquist sampling theorem in 2D, which dictates that the sampling rate w must be chosen carefully to fully resolve and describe the continuous signal that is being discretized (Oppenheim *et al.* , 1997). Specifically, our sampling rate is the size of an imaging pixel in the real space image, and should be chosen so that $w \leq \frac{2\pi}{2u_b}$. Here, u_b is the upper limit for the wavevector in the measured system. To fully capture possible high **q** features, we choose the reciprocal lattice vector for the $\sqrt{3} \times \sqrt{3}$ Brillouin zone, whose magnitude is $\frac{4\pi}{\sqrt{3}a}$ ($a = 6.65$Å). Then, w must chosen to be less than 2.88 Å/px. Therefore, imaging parameters must be precisely chosen to acquire adequate **q**-space resolution while also providing enough information within higher zones to draw correct conclusions regarding the origin of various scattering vectors. The imaging time must be taken into account as well, as doubling the linear dimension **or** the image resolution of the **r**-space image quadruples the time (Hoffman, 2003). The chances of tip changes due to a crash or other experimental uncertainties makes it desirable to keep the measurement time within a reasonable window.

An average image size of 35×35 nm^2 was chosen for the **r**-space dI/dV images, corresponding to a **q**-space resolution of ∼5.4% of the 3×3 Brillouin zone. In addition, to satisfy the Nyquist sampling theorem, the pixel density is chosen to be 8 pixels for each nm, corresponding to a real space resolution of $w = 1.25$ Å/pixel. With these parameters,

each image takes approximately three hours, allowing a full data collection of the energy dependent constant energy contour to be completed in only a few days.

The following discussion will explore the evolution of the energy resolved modulations in the local tunneling density of states $N(\mathbf{r}, E)$ in the $\frac{dI}{dV}\Big|_V$ images by computing the Fourier Transform:

$$N(\mathbf{q}, E) = \sum_{\mathbf{r}_i \in (L_x \times L_y)} e^{-i\mathbf{q}\cdot\mathbf{r}_i} N(\mathbf{r}_i, E)$$

followed by the wave-vector power spectrum (Capriotti *et al.* , 2003):

$$P(\mathbf{q}, E) = \frac{|N(\mathbf{q}, E)|^2}{L^2}$$

Here, L_x,L_y is the x-y grid upon which the $\frac{dI}{dV}$ image is taken, and are not always chosen to be equivalent. The final Fourier transform will then be rectangular, but the distortion of the final image is corrected in accordance with the known symmetry using the Bragg points.

Figure 4.9 shows a QPI image of the surface following the above procedure. The topography and $\frac{dI}{dV}$ images were taken simultaneously with a tunneling bias of -2 mV, an oscillation frequency of 831 Hz, and a feedback current of 100 pA at 4.4 K. Clear signs of periodic intensity modulations within the LDOS map are observed in Figure 4.9(b). The power spectrum is given in (c) (For QPI processing, including any filtering and symmetry averaging, see Appendix A). The pattern appears to be quite complicated at first glance, but as is shown from the drawing in Figure 4.9(d), these are all from the same scattering channel. That is, the features within the circle are simply from replicas of the same circle in the next Brillouin zone, translated by a reciprocal lattice vector $\mathbf{G}$. The circle appears to slightly flatten out towards the higher symmetry points.

To study the evolution of the observed high intensity features, multiple $\frac{dI}{dV}$ images were taken at several energies around the Fermi level. A select few of these images are shown in Figure 4.10. The circle corresponding to the single scattering $\mathbf{q}$ vector remains very clear within 100 mV of the Fermi level. The circle gradually grows from negative to positive bias, indicating that the scattering vectors disperse with energy. The circle also begins to develop some hexagonal character at +20 meV, probably due to distortion of the underlying

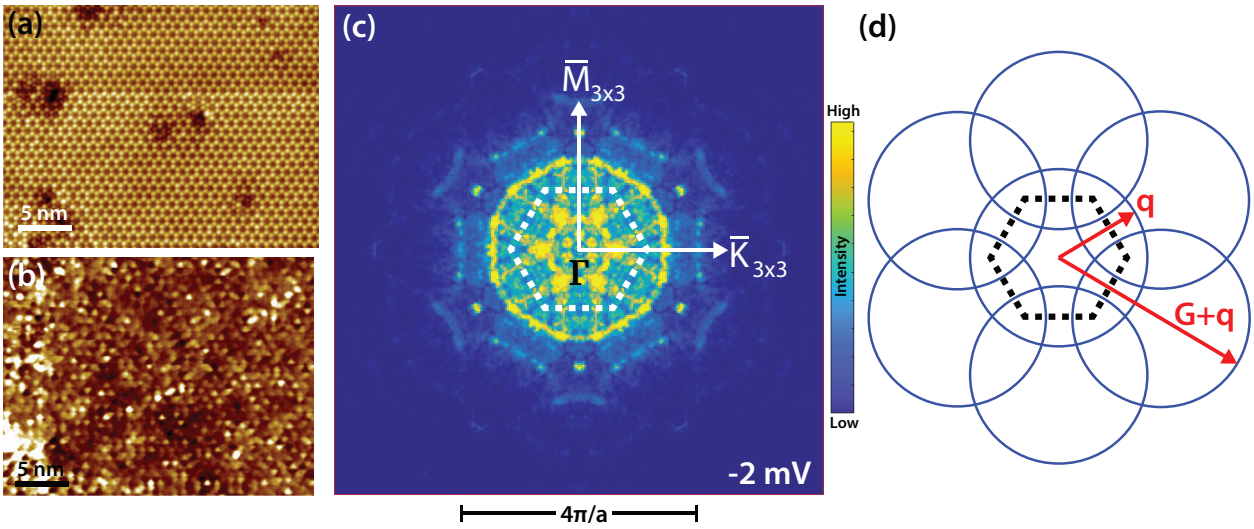

Figure 4.9: (a) STM image on the (3×3)-Pb surface, taken at a sample bias of +2 mV at 4.4 K. The area is chosen so that the defect density is adequate enough to generate scattering centers for elastic scattering between different eigenstates. The defects appear as dark "blotches" at such a low tunneling voltage. (b). $\frac{dI}{dV}$ image taken on the same area and using the same tunneling parameters as (a). Lock in setpoint was $V_{osc} = 0.5$ mV. (c). FT power spectrum of the $\frac{dI}{dV}$ image in (c). (d) Schematic illustration of the high intensity features from the experimental data, indicating that all features come from a single scattering channel.

free-electron-like bandstructure as the constant energy contour approaches the edges of the first Brillouin zone (the hexagon at the highest energies makes up approximately 80% of the first Brillouin zone). Power spectra for higher biases (not shown) only show the Bragg points that coincide with the periodicity of the crystal.

Around the time that this data set was completed, the first *ab initio* calculation for the (3×3)-Pb charge ordered structure was published, as previously it was only limited to the high temperature $(\sqrt{3} \times \sqrt{3})$ Pb/Si(111) phase (Tresca *et al.* , 2018). In this work, they propose a Fermi surface with two hexagons, due to a strong spin-orbit splitting of almost pure Rashba type. This leads to a large spin-orbit splitting as large as 0.13 eV. As the STM measurement described in the previous chapters is inherently non-spin sensitive, it is necessary to consider the effect that this would have on the Fermi surface, and thus what it would appear as in the case of isotropic scattering with time reversal symmetry conserved.

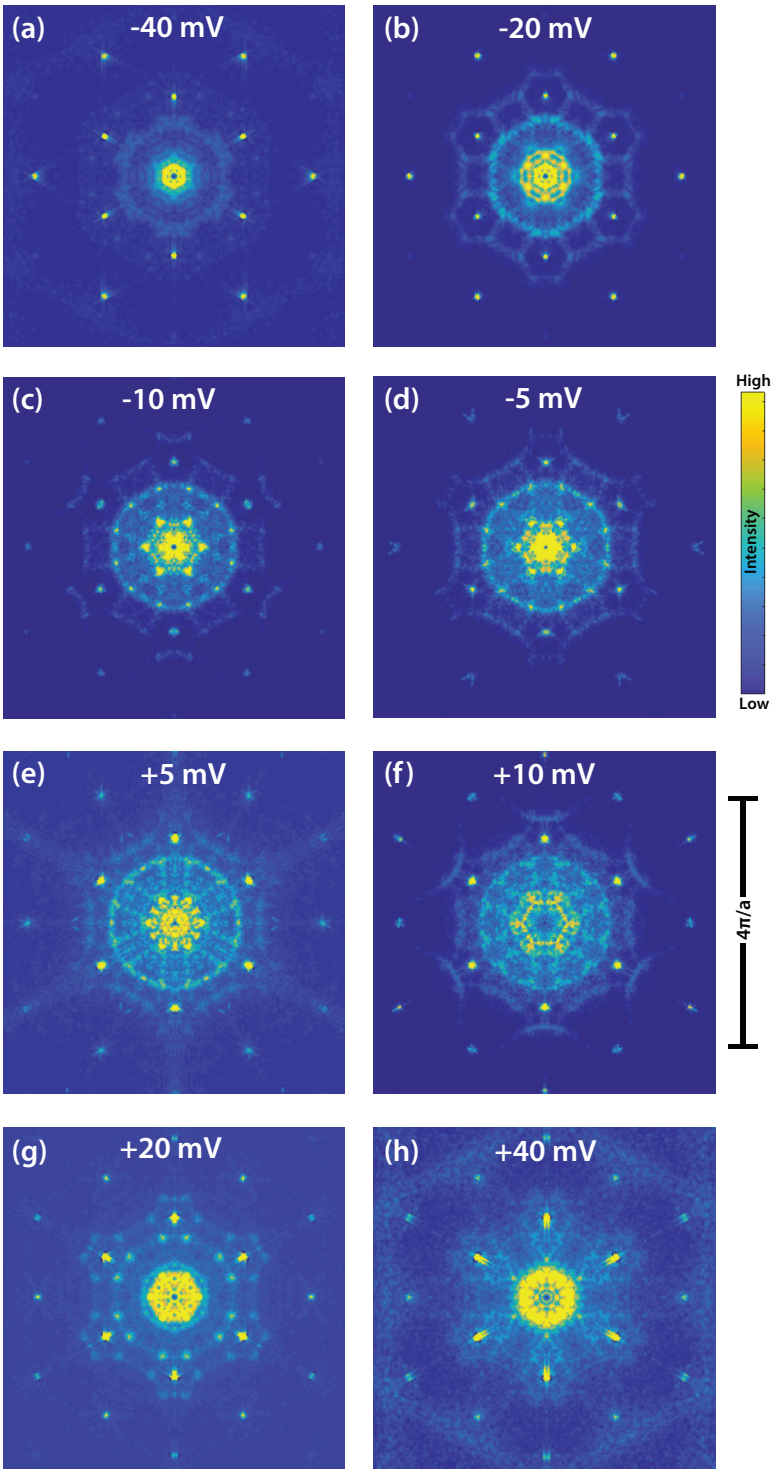

Figure 4.10: Various QPI patterns of the (3×3)-Pb structure. All images have been rotated such that the direction runs $\bar{\Gamma}\bar{M}$ vertically while the $\bar{\Gamma}\bar{K}$ direction runs horizontally. Image parameters are (a) I_T=300 pA V_{OSC}=2 mV (b) I_T=300 pA V_{OSC}=2 mV (c) I_T=150 pA V_{OSC}=1 mV (d) I_T=150 pA V_{OSC}=0.8 mV (e) I_T=150 pA V_{OSC}=0.8 mV (f) I_T=150 pA V_{OSC}=1 mV (g) I_T=300 pA V_{OSC}=2 mV (h) I_T=300 pA V_{OSC}=2 mV. All images were taken with an oscillation frequency of 831 Hz and at T=4.4 K.

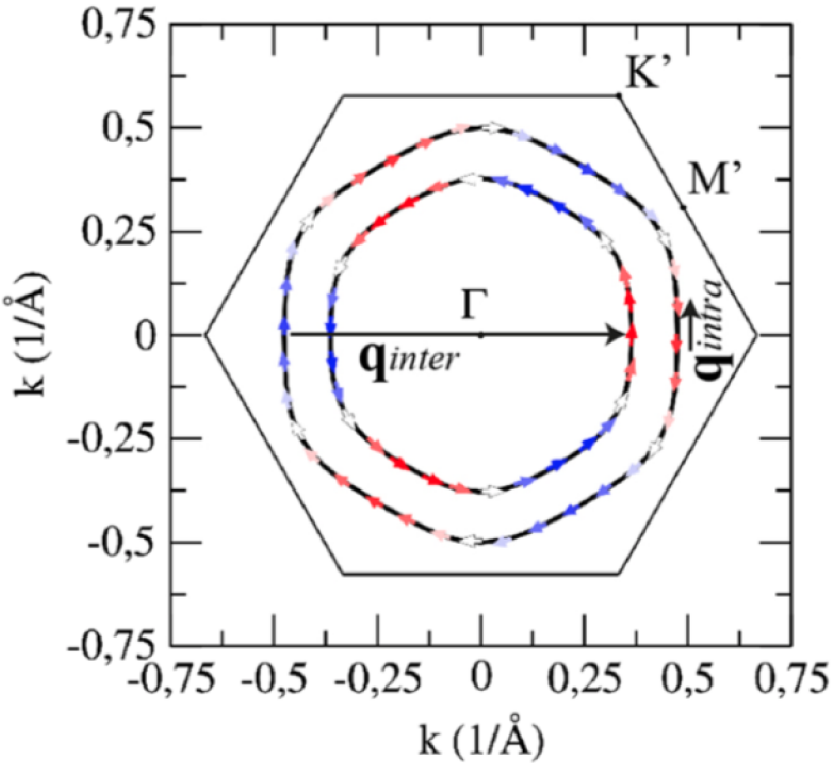

Figure 4.11: Fermi surface from fully relativistic GGA+U calculations from Tresca *et al.* (2018). The arrows indicate the spin polarization of the spin-split surface band, and the colors indicate out of plane components (these are $< 1\%$ of in plane one, so this will be taken as negligible in the discussion).

Figure 4.11 shows the calculated Fermi surface of the (3×3)-Pb surface reconstruction extracted from Tresca *et al.* (2018). The two Fermi circles carry opposite helicities, indicated by the arrows. Intraband backscattering is mostly forbidden because the backscattering from k to -k is suppressed due to the antiparallel spin orientations. Meanwhile, the interband scattering is always allowed because the spin orientations are nearly entirely parallel. This will result in only one circle with radius $\mathbf{q}_{inter}$ in the data, as the features between both circles will simply overlap due to the interband scattering.

As the paper published by Tresca et. al. also includes the calculated dispersion for the *1 up 2 down* (3×3) ground state including spin-orbit coupling, we can compare the dispersion of our experimental data with their calculated values. The $\mathbf{q}$ vectors along the $\bar{\Gamma}\bar{\mathrm{M}}$ direction are extracted by taking line profiles of each of the QPI results and plotting the maximum

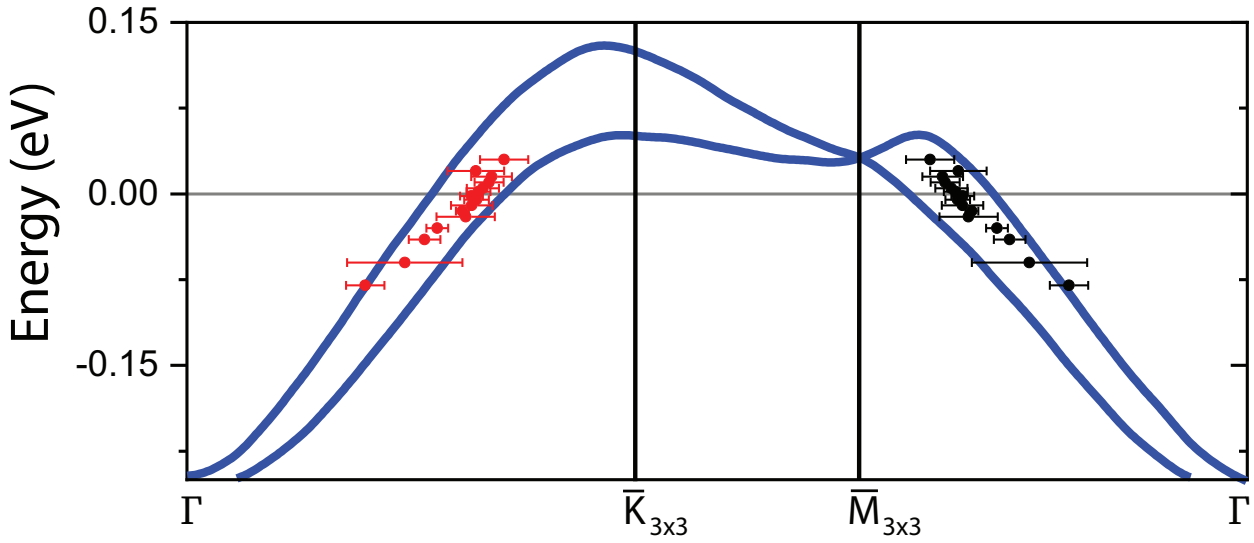

Figure 4.12: Surface dispersion as published by Tresca *et al.* (2018) within GGA+U with U=1.75, compared with the dispersion observed from QPI. Data is extracted for only the spin split band that crosses the Fermi level (blue line). The collected data is plotted by black points along the $\bar{\Gamma}\bar{\mathrm{M}}$ direction, and red points along the $\bar{\Gamma}\bar{\mathrm{K}}$ directions. Error bars are the full width half max (FWHM) of the peaks taken from line profiles in the constant energy contours.

of the most intense part of the Fermi circle (many of the values are taken approximately from the QPI image, as the intensity of the QPI features tends to be quite small). These values are then converted to **k**-space and plotted alongside the calculated bandstructure in Figure 4.12. The data is in good agreement with theory. The Fermi wavevector is found to be $k_f = .234 \pm .005\ \text{Å}^{-1}$, in good agreement with more recent works (Adler *et al.* , 2019).

4.4 Impurity Doping for Magnetic Scattering

To access the forbidden backscattering channels mentioned in the previous section, magnetic impurities can be introduced onto the surface to locally break the time reversal symmetry. The process can be visualized in the following way: A magnetic scattering potential can rotate the spin of an itinerant electron. This rotation will then evolve the scattering states. That is, the spin overlap will not prevent backscattering, and the forbidden channels will then be accessed. This method has had mixed results when used on other systems. Depositing Co

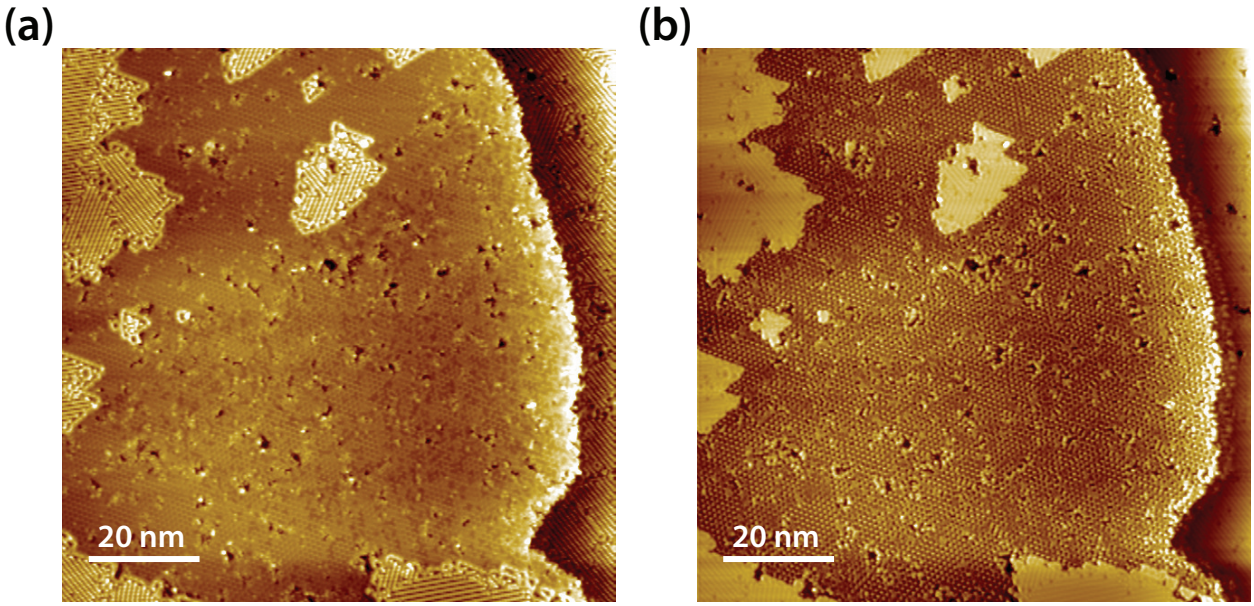

Figure 4.13: The (3×3) Pb/Si(111) surface with $<$ .01 ML of vanadium deposited. The surface periodicity is nearly completely destroyed. Images are on the same area at (a) -1.5 V 30 pA (b) +1.5 V 30 pA.

atoms on the topological insulator $Bi_{1-x}Sb_x$ enhanced the spin-conserving scatterings but did not reveal any new features (Yoshizawa *et al.* , 2015). The attempt of depositing the magnetic MnPc molecule on Bi(111) returned no new features as well, predicted to be due to inequivalent rotations of spin states of the electrons (Stróżecka *et al.* , 2011). However, work on the doped topological insulator $Bi_{2-x}Fe_xTe_{3+\delta}$ using Fe atoms as magnetic scatterers revealed clear evidence of broken time reversal symmetry (Okada *et al.* , 2011). A more recent work has shown that spin-orbit scattering can substantially influence the features within QPI patterns of polar semiconductor BiTeI (Kohsaka *et al.* , 2017).

In the attempt to access the forbidden backscattering channels for the (3×3) Pb/Si(111) phase, two species of magnetic dopants were used. The first candidate attempted was Vanadium due to its spin of 3/2 and availability of a V source already mounted inside the MBE chamber. However, as can be seen in Figure 4.13 , the V adatoms tend to imbed themselves into the surface and destroy any periodicity that existed before.

A more careful deposition is clearly needed in order to create a surface decorated by magnetic impurities without destroying the surface. One possibility to decrease motion of

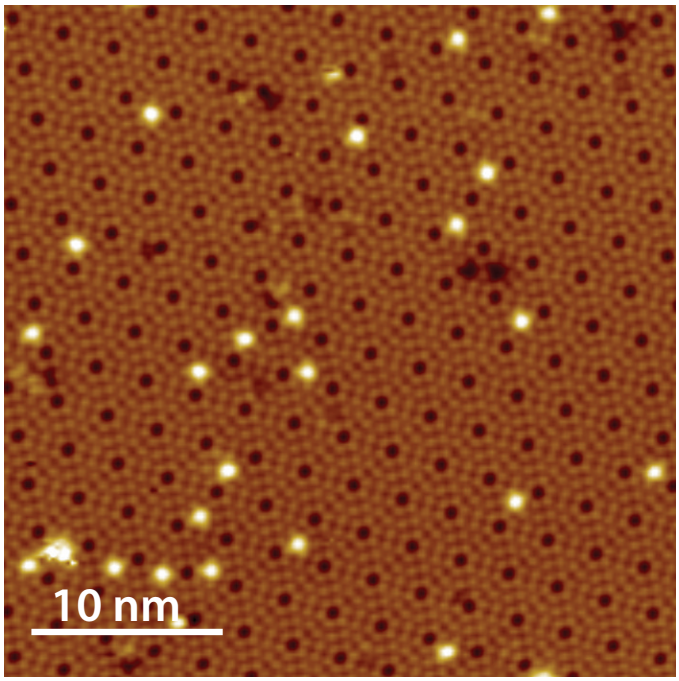

Figure 4.14: A small amount of Mn deposited on the clean Si(111)-7x7 surface. Tunneling parameters are 2 V 30 pA.

the impurities on the surface is to deposit while the sample is cold, which will help to "freeze" the motion of the adatom as soon as it hits the sample. However, this raises the complication of mounting a Knudsen cell within the LT-STM chamber. In this case, Vanadium is no longer an option, as the high temperature needed for effusion is greater than 1000° C. Such a high temperature, even with the addition of radiation shielding, can greatly affect the stability of the temperature of the LT-STM when it is at the low temperature of 4.5 K. Therefore, another candidate must be considered that fits the following requirements: 1) it must have a relatively low temperature of effusion, and 2) it must possess a large spin. The element eventually decided upon was Mn, which has an effusion temperature of $\sim 550°$ C and a spin of 5/2. The material was mounted in a custom effusion cell prototype similar to the one described in Section 2.2. With this design, the pressure of the LT-STM chamber during deposition hardly increased above the base pressure of 3×10^{-11} mbar, and the LT-STM did not show any sign of temperature instability due to the hot effusion cell.

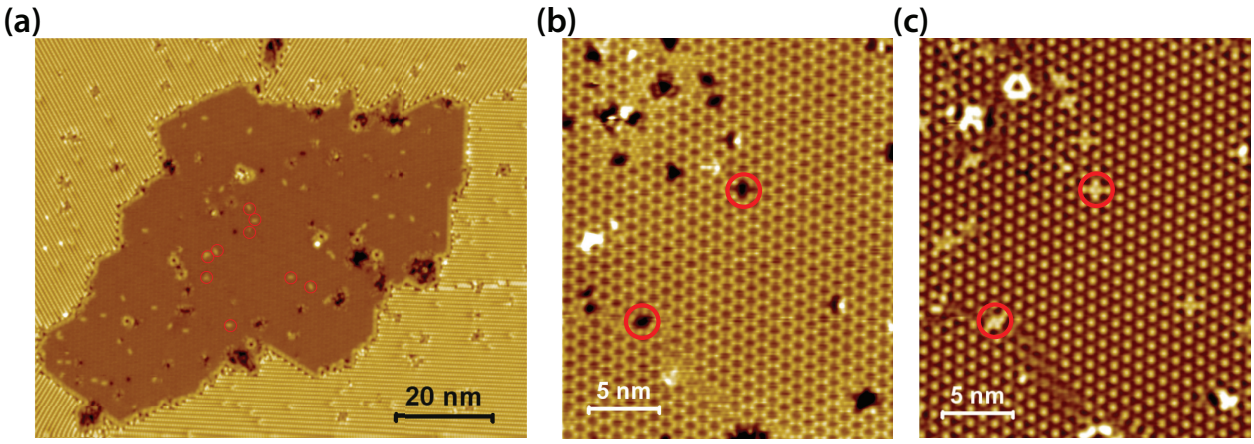

Figure 4.15: The Mn decorated (3 × 3)-Pb surface at 4.5 K. Some of the Mn adatoms are circled in red. A contrast inversion of the Mn defects appears upon a polarity switch. Tunneling parameters are (a) +1.5 V 30 pA (b) +1.0 V 30 pA (c) -1.0 V 30 pA.

The Mn was deposited onto the sample held by wobblestick directly over the Mn effusion cell, after being in contact with the cold LT-STM sample stage. The effusion cell crucible temperature was held at 550° C, and the sample was placed several mm over the effusion cell aperture for less than 10 seconds. This ensured a minimal sample temperature variation during deposition. In fact, when this deposition is done at 4.5 K, the sample stage temperature only rises to ∼10 K after reinserting the sample. For initial tests, a small amount of Mn was deposited on the clean Si(111)-7x7 surface. The resulting Mn decorated surface is shown in Figure 4.14. The Mn atoms appear as single bright point defects, with ∼1 Mn atom per 50 nm^2.

Figure 4.15 shows the Mn decorated (3 × 3)-Pb surface. The bright Mn defects are marked by red circles. They are characterized by a contrast inversion between the empty and filled states. In contrast to the vanadium adatoms, the Mn decorated surface maintains its periodicity. QPI imaging was then performed exactly in the same way as the clean (3 × 3)-Pb system.

The QPI patterns from the surface with Mn are given in Figure 4.16. Remarkably, several new features are seen in nearly all of the QPI patterns (these are emphasized with green arcs within the figure). At -40 mV (Figure 4.16(a)), the circle looks broader than that without the presence of Mn. In the QPI pattern taken at -20 mV (Figure 4.16(b)), signs of a fine

structure within the initial Fermi circle begin to appear, as well as a slight broadening of the circle itself. The differences become much more clear in the -10 mV QPI pattern (Figure 4.16(c)), as the fine structure appears as an ordered "crosshatch" within the circle. The semicircles responsible for this crosshatch are centered around ($\sqrt{3} \times \sqrt{3}$) reciprocal lattice points. In addition, the Fermi circle appears broader towards the $\bar{\Gamma}\bar{\mathrm{K}}$ direction. At -5 mV, an internal hexagon appears at smaller **q** (Figure 4.16(d)). Perhaps the most interesting are the two semicircles that only appear around the (3×3) Bragg points in the higher zones within the +5 mV image. The circle observed for the system without the presence of Mn is marked in red, while a new semicircle of larger radius is marked in green. This is remarkably similar to what one would expect to observe in the spin split Fermi surface (Tresca *et al.* , 2018). In fact, though shifted towards higher momentum, the difference between the **k** values extracted from this pattern agrees well with the splitting calculated by Tresca et. al of $\sim$.12 1/Å (Figure 4.17). The QPI results at higher energies (Figures 4.16(f-h)) do not show clear differences, except for a possible enhancement of isotropic scattering from the greater amount of defect scattering centers.

As the QPI image taken at -10 mV seems to contain the most amount of detail, further processing was done to reduce the noise of the FT and enhance the fine structure at low **q**. This was done by applying a Weiner filter, an image processing tool used to deconvolve the noise from the signal (for details, see González & Woods (2002)) . The final result is given in Figure 4.18. The "crosshatch" pattern is much more obvious, though it is still much less intense than the inner Fermi circle. The features that make up the crosshatch can be reproduced by three large circles (green in Figure 4.18) centered around the ($\sqrt{3} \times \sqrt{3}$) reciprocal lattice points, reminiscent of an underlying ($\sqrt{3} \times \sqrt{3}$) periodicity. These new circles correspond to k values of 4.63 1/Å 5.16 1/Å 5.74 1/Å, respectively. There appears to be two arcs of different radii that overlap, following the symmetry of the surface reconstruction. Interestingly, the largest circle seems to make up the inner hexagon at lower energy in Figure 4.16(d).

Unfortunately, the new features in the presence of Mn defects seem appear in only a few energies, making a full dispersion analysis of the primary features difficult. Whether this is due to the resolution of the experiment or to a greater scattering cross section at these

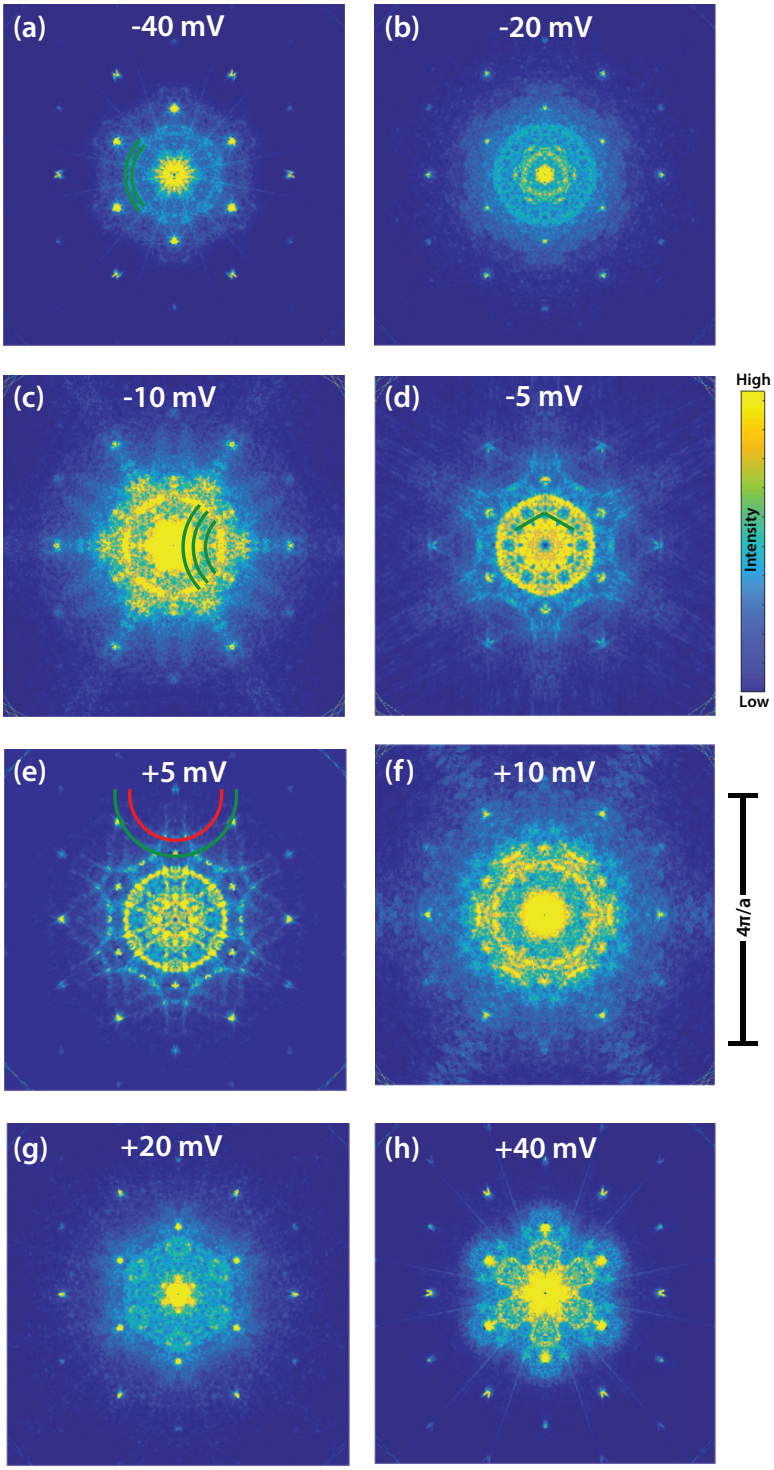

Figure 4.16: Various QPI patterns of the Mn decorated (3×3)-Pb structure. All images have been rotated such that the $\bar{\Gamma}\bar{M}$ direction runs vertically while the $\bar{\Gamma}\bar{K}$ direction runs horizontally. Image parameters are (a) I_T=200 pA V_{OSC}=3 mV (b) I_T=150 pA V_{OSC}=2 mV (c) I_T=150 pA V_{OSC}=1 mV (d) I_T=100 pA V_{OSC}=0.8 mV (e) I_T=100 pA V_{OSC}=0.8 mV (f) I_T=150 pA V_{OSC}=1 mV (g) I_T=150 pA V_{OSC}=2 mV (h) I_T=200 pA V_{OSC}=3 mV. All images were taken with an oscillation frequency of 831 Hz and at T=4.4 K.

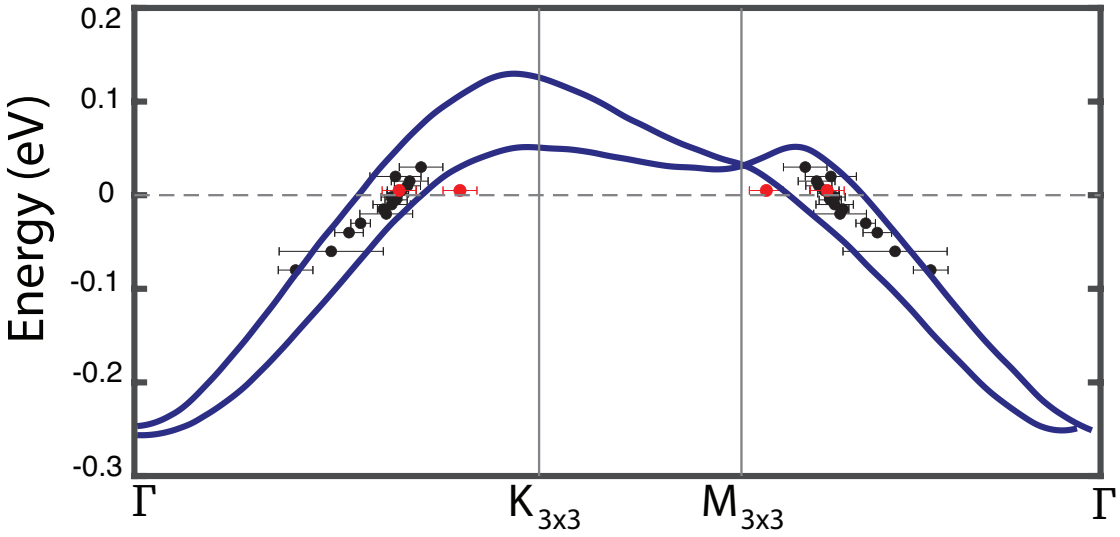

Figure 4.17: Surface dispersion as published by Tresca *et al.* (2018) within GGA+U with U=1.75, with data points overlaid from the dispersion in the +5 mV QPI pattern (red).

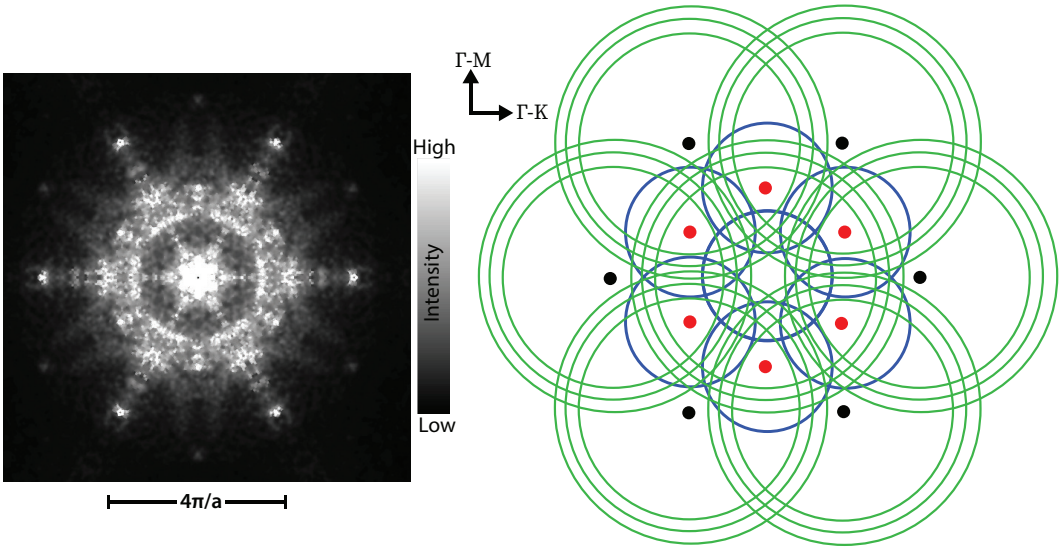

Figure 4.18: Processed -10 mV QPI image using a Weiner filter. The low **q** features become much sharper, revealing a crosshatch pattern. A schematic of the major features is shown on the right. The blue circles are the original circles as seen in the case without Mn defects, the large green circles surrounding the $(\sqrt{3} \times \sqrt{3})$ reciprocal lattice points completely match the crosshatch pattern.

biases with the Mn atoms remains in question. Nonetheless, it is clear that the Mn has a significant effect on the observed QPI images. Perhaps the biggest evidence for a spin split bandstructure is from the +5 mV QPI pattern, as the two semicircles appears similar to the that calculated in (Tresca *et al.* , 2018). However, the appearance of these features around only the (3×3) Bragg points and large circles around the $(\sqrt{3}\times\sqrt{3})$ reciprocal lattice points at -10 mV indicates a more complex band splitting mechanism.

4.5 QPI simulations

To more closely compare the theoretical dispersion with the experimental quasiparticle interference patterns, we move to simulations of the quasiparticle interference patterns using the T-matrix approximation. The theory will be briefly summarized here. In a nutshell, the T-matrix formalism involves a perturbative summation of diagrams resulting from the expansion of the Green function of a system to finite order in the impurity scattering (Bena, 2016). We start with the "bare" Green's function, given by

$$G_0(\omega) = \frac{1}{\omega + i\delta - H_0}.$$

Here, the energy is ω, H_0 is the Hamiltonian for the "clean" system, and δ reflects broadening due to impurities, and is taken to be an infinitesimal positive constant. The next step in the model is to introduce a single impurity into the system: in our case, we will assume a point-defect potential scatterer of strength V. The Green's function for this system in the presence of the impurity is obtained from adding all of the contributions from scattering processes of all orders (i.e. including multiple elastic scattering events) to the "bare" Green's function. The diagram for this process is given in Figure 4.19 (Bena, 2016), and the dressed Green's function in the presence of elastic scattering is given by

$$G(\mathbf{k},\mathbf{k}') = G_0(\mathbf{k})\delta_{\mathbf{k},\mathbf{k}'} + G_0(\mathbf{k})T_{\mathbf{k},\mathbf{k}'}G(\mathbf{k}'),$$

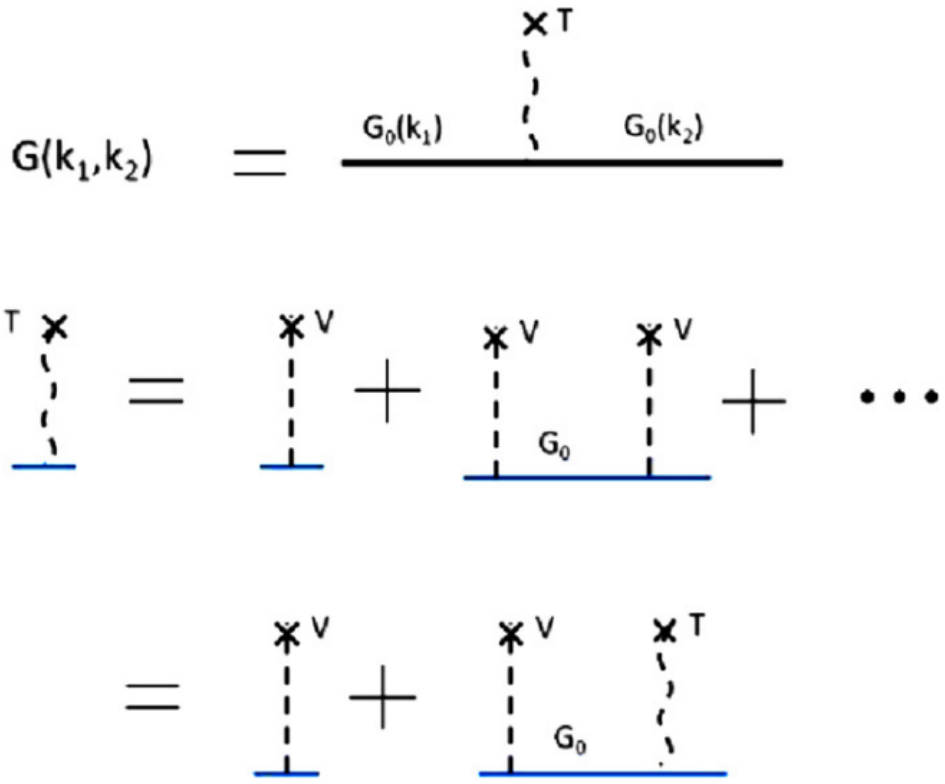

Figure 4.19: Feynman diagrams of the T-matrix approximation, where the Green's function for a surface with an impurity is given by the addition of the bare Green's function and the various scattering processes. Figure taken from Bena (2016).

with the T-matrix given by

$$T_{\mathbf{k},\mathbf{k}'} = V_{\mathbf{k},\mathbf{k}'} + \frac{1}{N}\sum_{k''} V_{\mathbf{k},\mathbf{k}''} G_0(\mathbf{k}'') T_{\mathbf{k}'',\mathbf{k}'}.$$

A further approximation to simplify this self-consistent equation is to assume that the impurity scattering potential is in the form of a delta function (i.e. isotropic point scatter), so that the momentum dependence is then lifted. This simplifies the T-matrix to

$$T(\omega) = \frac{V_0}{1 - \frac{1}{N} V_0 \sum_{\mathbf{k}} G_0(\mathbf{k}, \omega)}.$$

In order to generalize this expression to a multi-band system, the bare Green's function can be given by $G_0(\mathbf{k},\omega) = \sum_n g_n(\mathbf{k},\omega)|\psi_n(\mathbf{k})\rangle\langle\psi_n(\mathbf{k})|$ where $g_n(\mathbf{k},\omega) = (\omega + i\delta - \epsilon_n(\mathbf{k}))^{-1}$. The scattering potential then is a matrix operator, for example, in the case of isotropic scattering, $\hat{V} = V_0 I$, where I is the identity matrix. Here, $\epsilon_n(\mathbf{k})$ and $\psi_n(\mathbf{k})$ are the nth eigenvalue and the nth eigenstate of the bare Hamiltonian Kohsaka *et al.* (2017). Then, adding in the frequency dependence to the modulations in the local density of states due to the impurities, the final expression for the QPI pattern is then given by

$$\delta\rho(\mathbf{q},\omega) = \frac{i}{2\pi}\sum_{\mathbf{k}}\left[G_0(\mathbf{k},\omega)T(\omega)G_0(\mathbf{k}+\mathbf{q},\omega) - G_0(G_0(\mathbf{k}+\mathbf{q},\omega)T(\omega)G_0(\mathbf{k},\omega)^*\right].$$

For best comparison with the power spectral density given from the experimental data, calculated QPI patterns will be plotted as $|Re(\rho(\mathbf{q},\omega)|$.

Initial QPI calculations to understand primary observations in the experimental QPI were performed for the using a tight binding dispersion with nearest neighbor hopping on a triangular lattice. This is given by

$$\epsilon_0(\mathbf{k}) = -2t[\cos(k_x) + \cos(\frac{1}{2}k_x + \frac{\sqrt{3}}{2}k_y) + \cos(\frac{1}{2}k_x - \frac{\sqrt{3}}{2}k_y)] - \mu.$$

In this calculation, the nearest neighbor hopping is held at $t_1 = 32$ meV, and $\mu = 25$ meV to more closely match the data. It is to be emphasized that this is merely for initial comparison, as this dispersion lacks the energy renormalization performed by the GGA+U dispersion in Reference Tresca *et al.* (2018), more hopping integrals are needed as these surfaces require next nearest neighbor hopping terms Li *et al.* (2013), and Rashba effects are not included. However, the region within 100 meV of the Fermi level is in good agreement with the experimental dispersion extracted from the experimental QPI.

The QPI simulations are compared to the experimental data in Figure 4.21. The theory agrees very well with the experiment, with identical Fermi wavevectors and replicas within the first BZ. However, the consistency between the data and theory is not exclusive of a spin split electronic ground state, as the tight binding dispersion lies directly between the two theoretical surface bands at the Fermi level while the error bars for the momentum values

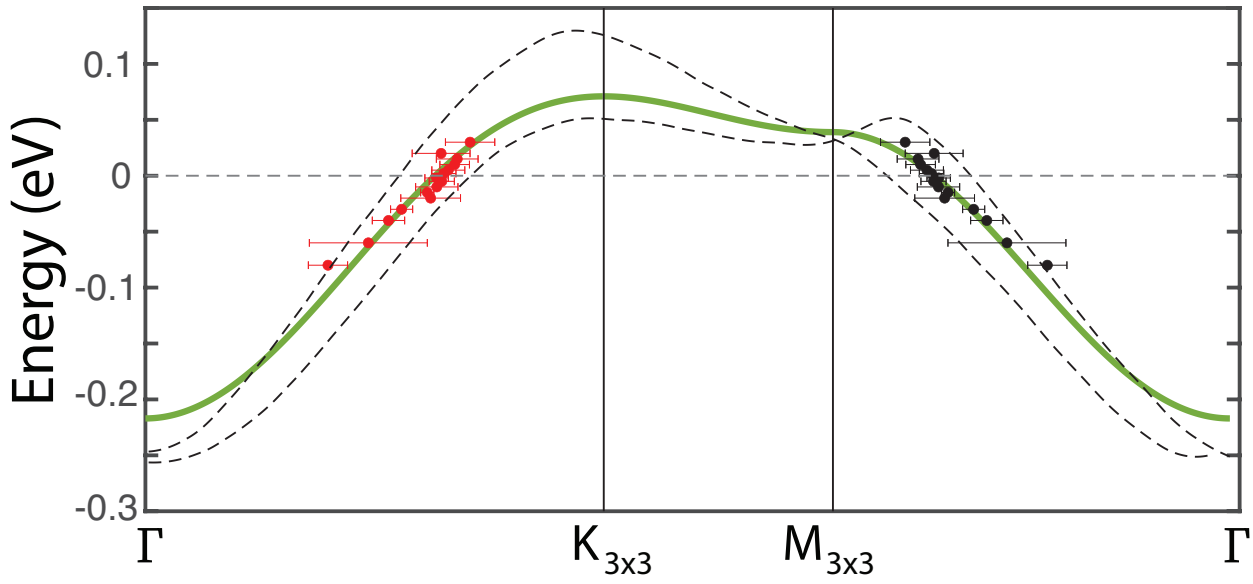

Figure 4.20: Tight binding dispersion for nearest neighbor hopping (green line) compared with the GGA+U spin split dispersion from Tresca *et al.* (2018) (dashed lines). Parameters are chosen for a best fit with the experimental data.

are quite large. The next step would be to calculate the QPI pattern with two bands that contain the spin character that defines the Rashba spin split system.

The Rashba Hamiltonian in 2D is given by contributions from both the tight binding model and the Rashba component: $H = H_{TB} + H_R$. The Rashba component of the Hamiltonian is an effect due to the spin orbit interaction and the lack of inversion symmetry perpendicular to the plane for a 2D surface, and is given by

$$H_R = \lambda_R(\nabla V \times \mathbf{p}) \cdot \mathbf{s}.$$

Here, λ_R is the coupling constant between the potential gradient at the surface ∇V and the electron's momentum in the plane $\mathbf{p}$. The vector of Pauli matrices describing the spin is given in the vector $\mathbf{s}$. Diagonalizing this Hamiltonian returns two bands with opposite spin texture, given by (Mii *et al.* , 2014)

$$\epsilon_{\pm}(\mathbf{k}) = \epsilon_0(\mathbf{k}) \pm \left| H_k^{\uparrow\downarrow} \right|.$$

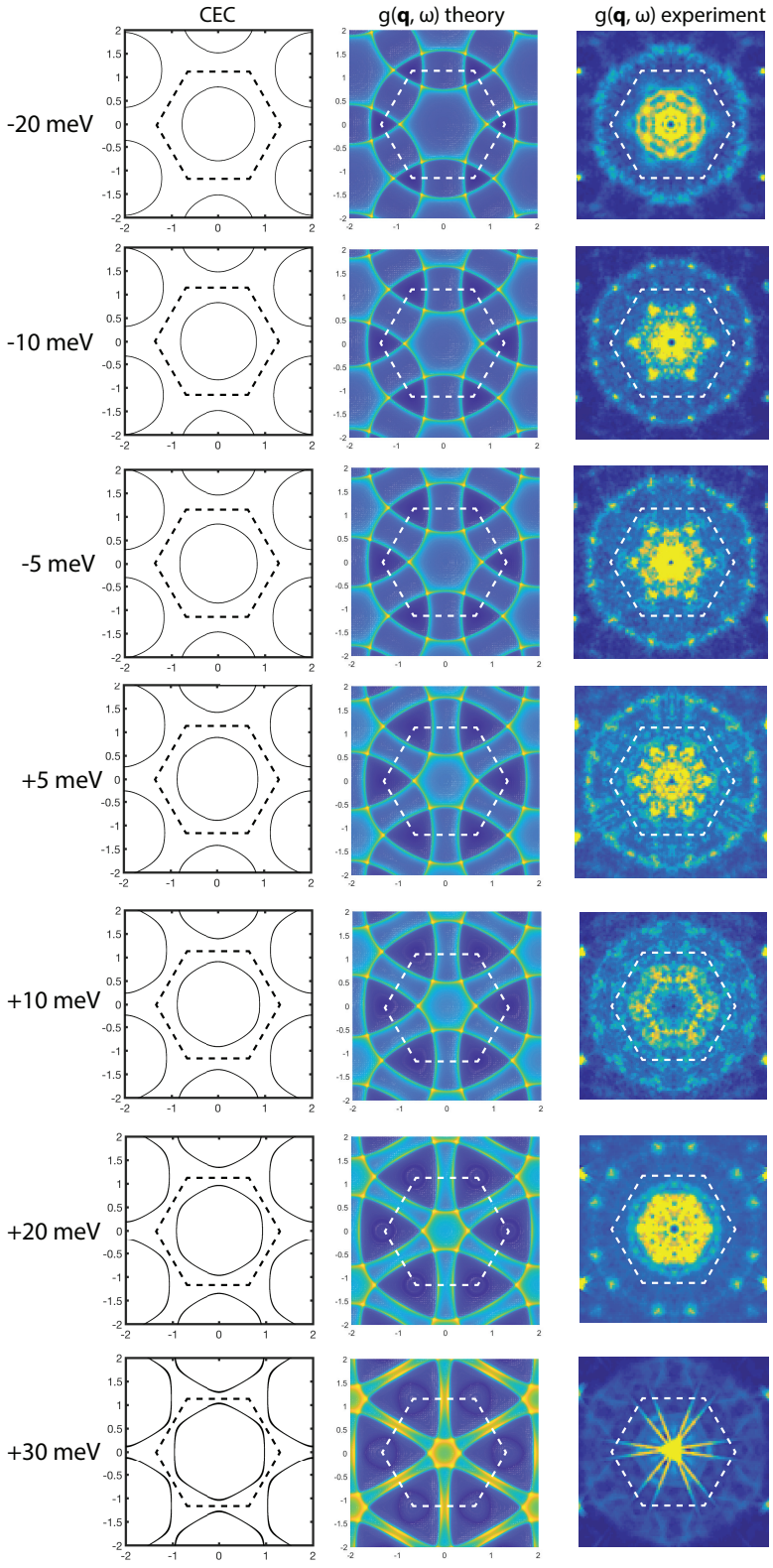

Figure 4.21: Comparison between experimental and theoretical QPI. The leftmost column contains the constant energy contours (CEC) for the tight binding dispersion. Brillouin zones are marked by dashed hexagons.

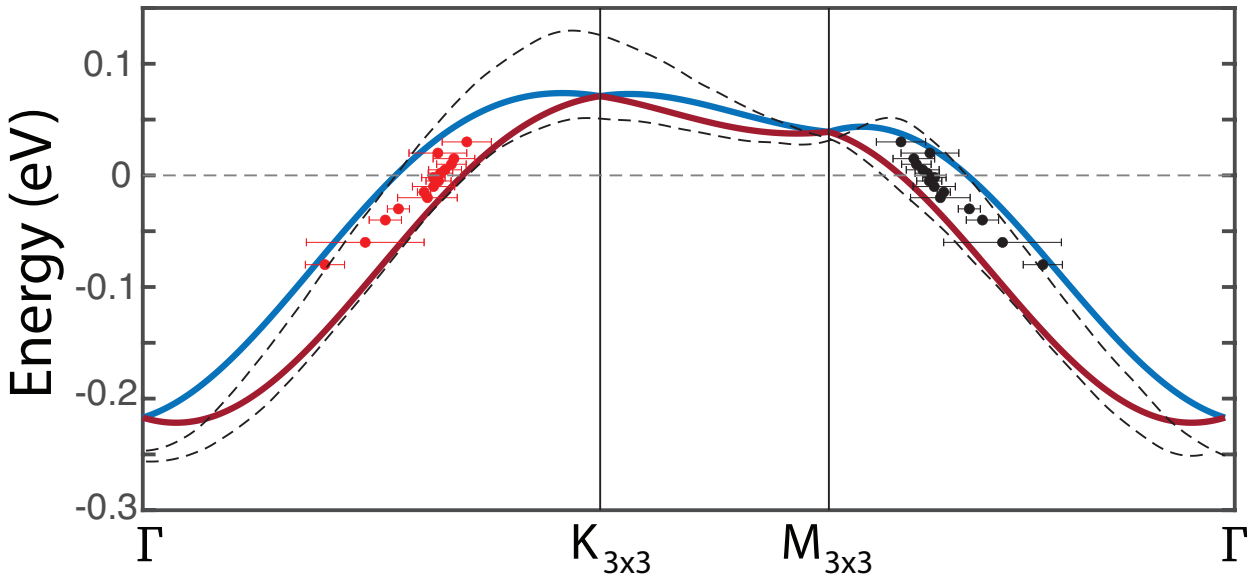

Figure 4.22: Calculated spin split dispersion within the Rashba Hamiltonian showing a spin split dispersion, indicated by the red and blue lines. The experimental dispersion is given by the data points with error bars. Overlaid with GGA+U dispersion from Tresca *et al.* (2018) (dashed lines).

The upper and lower energy bands are signified in the $\pm$ subscript, and the bare tight binding dispersion $\epsilon_0(\mathbf{k})$ is the same as that given for the non-polarized case on the previous page. For the triangular lattice, the spin character is in the form

$$H_k^{\uparrow\downarrow} = 2it_{sf}[e^{\frac{i\pi}{6}}\sin(k_x) + e^{\frac{-i\pi}{6}}\sin(\frac{1}{2}k_x + \frac{\sqrt{3}}{2}k_y) + e^{\frac{i\pi}{2}}\sin(\frac{1}{2}k_x - \frac{\sqrt{3}}{2}k_y)].$$

The two bands are plotted in Figure 4.22 with the same tight binding parameters for the non-Rashba case. t_{sf} is chosen to be 10 meV to more closely match the GGA+U dispersion (Tresca *et al.* , 2018). It is worth noting that the largest difference in this calculation from the GGA+U dispersion (dashed line) is the degeneracy at the K point. This is simply due to the calculation given in this work being a pure 2D triangular lattice calculation, where the GGA+U includes several silicon layers beneath, which lacks the 6-fold symmetry of the triangular surface lattice. Nonetheless, the window within the Fermi level that pertains to the experimental data is still in close agreement.

A first attempt at simulating the QPI map is calculated assuming pure scalar impurity scattering by neglecting the spin contribution of the two bands. A very real possibility is that the scattering features are simply enhanced as more scattering centers are introduced (Yoshizawa *et al.* , 2015). The results of these calculations are given in Figure 4.23. The results are as follows: though the "fine" structure that appears within the Fermi circle does not agree at all with the calculations (such as the 'arcs' at -10 mV or the internal hexagon at -5 mV), there exists some possible similarities. That is, the data at +10 mV appears to show small signatures of another Fermi circle towards the $\bar{\Gamma}\bar{\mathrm{K}}$ directions, and the larger width of the Fermi circle at 10 mV indicates a possible envelope of several features. However, the results are not conclusive in either support or disagreement with the calculated QPI. In additional disagreement, calculations were performed using the full spin texture of the Rashba spin split bands, which led to a full cancelation of the QPI pattern, most likely due to the exact cancellation of the components when a spin flip is introduced.

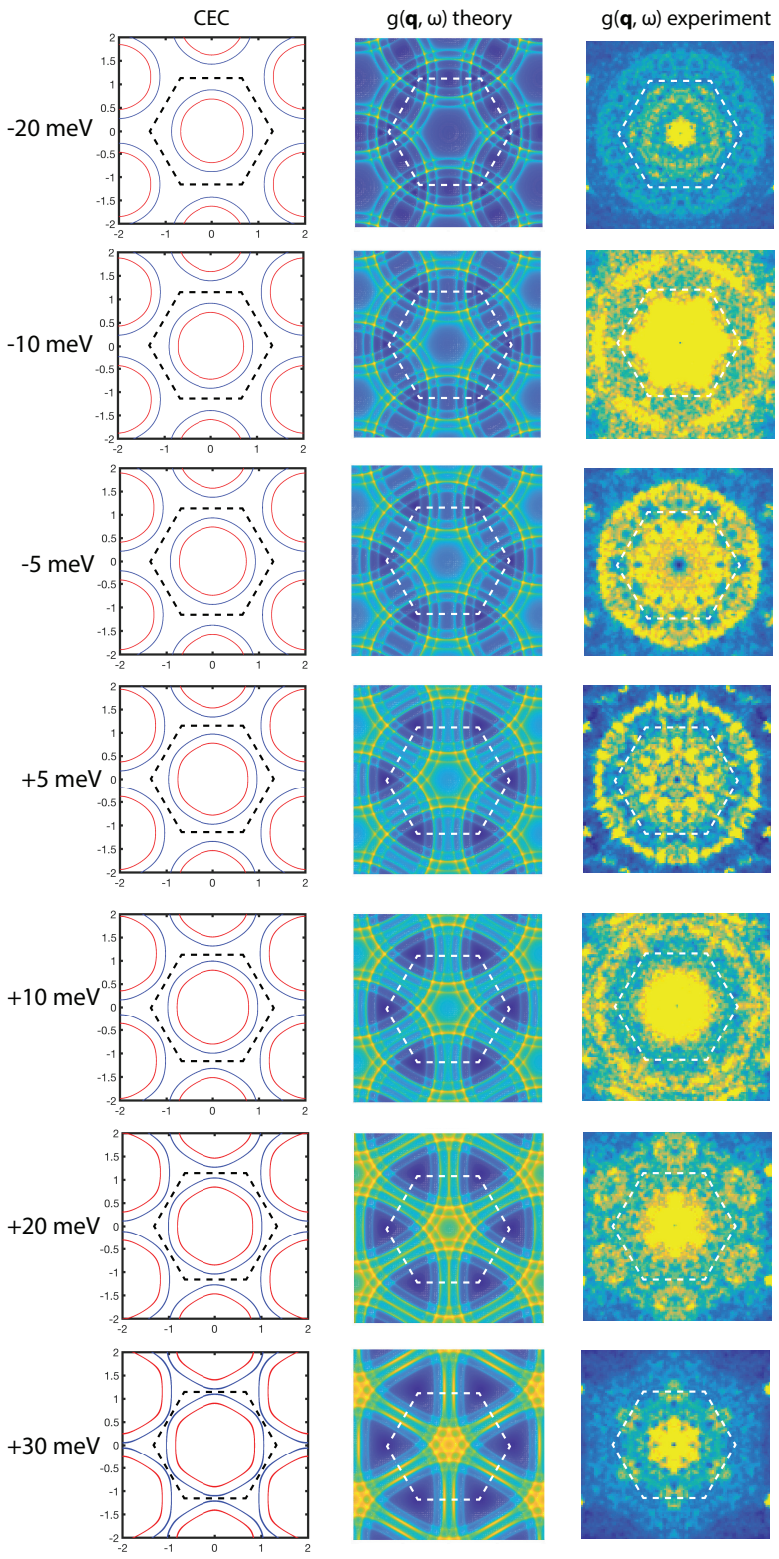

Figure 4.23: Comparison between experimental and theoretical QPI. The leftmost column contains the constant energy contours (CEC) for the tight binding dispersion. Brillouin zones are marked by dashed hexagons.

4.6 Conclusion

The goal of the Pb/Si(111) experiment was ultimately to explore the doping phase diagram of the 1/3 ML (3×3)-Pb reconstruction, and to provide further insight into whether the charge ordered ground state is in a *1 up 2 down* or *1 down 2 up* configuration. Unfortunately, it was found that this phase becomes unstable as hole doping is increased. However, the full morphology study on these various Si(111) substrates gleaned valuable information on the optimal growth conditions for the "undoped" case, allowing much larger domains to be grown than previously seen in other works. This, combined with the metallic ground state of the surface, fit the requirements for high resolution QPI imaging. The bandstructure extracted from these curves provides valuable experimental evidence for a *1 up 2 down* charge ordered ground state. In addition, our work supports some of the recent predictions by Tresca *et al.* (2018). Specifically, the STS results are in good agreement with the GGA+U results with Rashba spin splitting (Figure 4.1(b)), reinforcing the role of the Hubbard U in this system. Additionally, QPI features only show components that are consistent with the surface state bands with U included, in contrast to the $U = 0$ case in Figure 4.1(a). In an attempt to verify possible Rashba spin split bandstructure, magnetic impurities were introduced onto the surface, after which new scattering features were observed. Though the exact origin of these new features remains to be determined, it is evidence enough that this system contains some degree of spin texture. More theoretical work is needed to fully elucidate the origins of these observations in the experimental data.

Chapter 5

Adsorbate Hole Doping Attempts on the Sn/Si(111) Surface

5.1 Introduction

The success of the modulation doping technique for the Si(111)-($\sqrt{3} \times \sqrt{3}$) R30°-Sn surface described in Section 3.2 provides incentive to use other doping methods to further explore the electronic phase diagram of this system. This work has already covered the use of adsorbate doping using potassium adatoms that act as electron donors, with the surprising effect of induced charge ordering, resulting in a new reconstruction. On the other side of the phase diagram, we can use electron accepting molecules in a similar fashion. However, finding appropriate adsorbates that will accept a large percentage of electrons from the surface without causing huge defect contributions is a difficult task. Recent work has shown that the organic molecules TCNQ and F4-TCNQ are strongly electronegative and have been used as electron acceptors on graphene surfaces (Kumar *et al.* , 2017). Indeed, the lowest unoccupied molecular orbital of the F4-TCNQ molecule is located 5.24 eV below the vacuum level, slightly below the valence band maximum of silicon (the electron affinity of Si is 4.07 eV and the band gap is 1.12 eV) (Figure 5.1). Since the Fermi level of the Si(111)-($\sqrt{3} \times \sqrt{3}$)R30°-Sn system is located 0.5 eV above the valence band maximum of Si(111) (Ming *et al.* , 2017), adsorption of the F4-TCNQ molecule could be an efficient way to further hole dope the Mott insulating parent system.

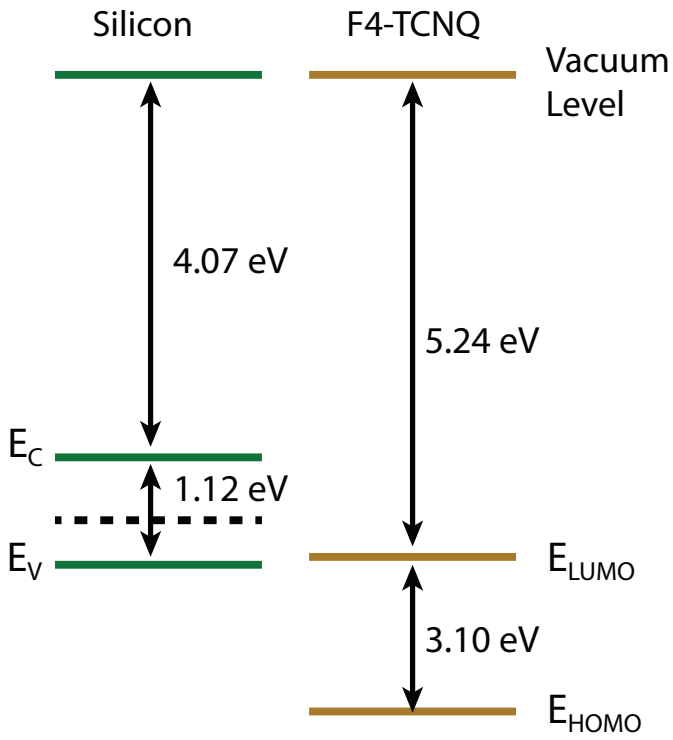

Figure 5.1: Band-energy levels in silicon and F4-TCNQ. The position of the Fermi level of the Si(111)-($\sqrt{3} \times \sqrt{3}$) R30°-Sn is marked by a dashed line.

5.2 Results and Discussion

Similar to the Mn deposition on the Pb/Si(111) system in Section 4.4, a custom effusion cell was mounted directly into the LT-STM chamber for low temperature F4-TCNQ deposition. However, as the sublimation temperature of the molecule is $< 100°$ C, a special procedure for preparing the chamber is required. Since the bake-out temperature for a clean UHV environment is $\sim 150°$ C, if the cell is simply baked along with the rest of the chamber, all of the F4-TCNQ source material would be deposited throughout the entire system. After several trials, an effective procedure for preparing the experiment was found to be as follows:

1. The LT-STM chamber is baked at the normal temperature of $\sim 150°$ C **without** the F4-TCNQ effusion cell mounted.

2. The LT-STM chamber is then quickly vented with ultra-high purity nitrogen gas.

3. While the gas is flowing, the F4-TCNQ effusion cell is mounted onto the chamber.

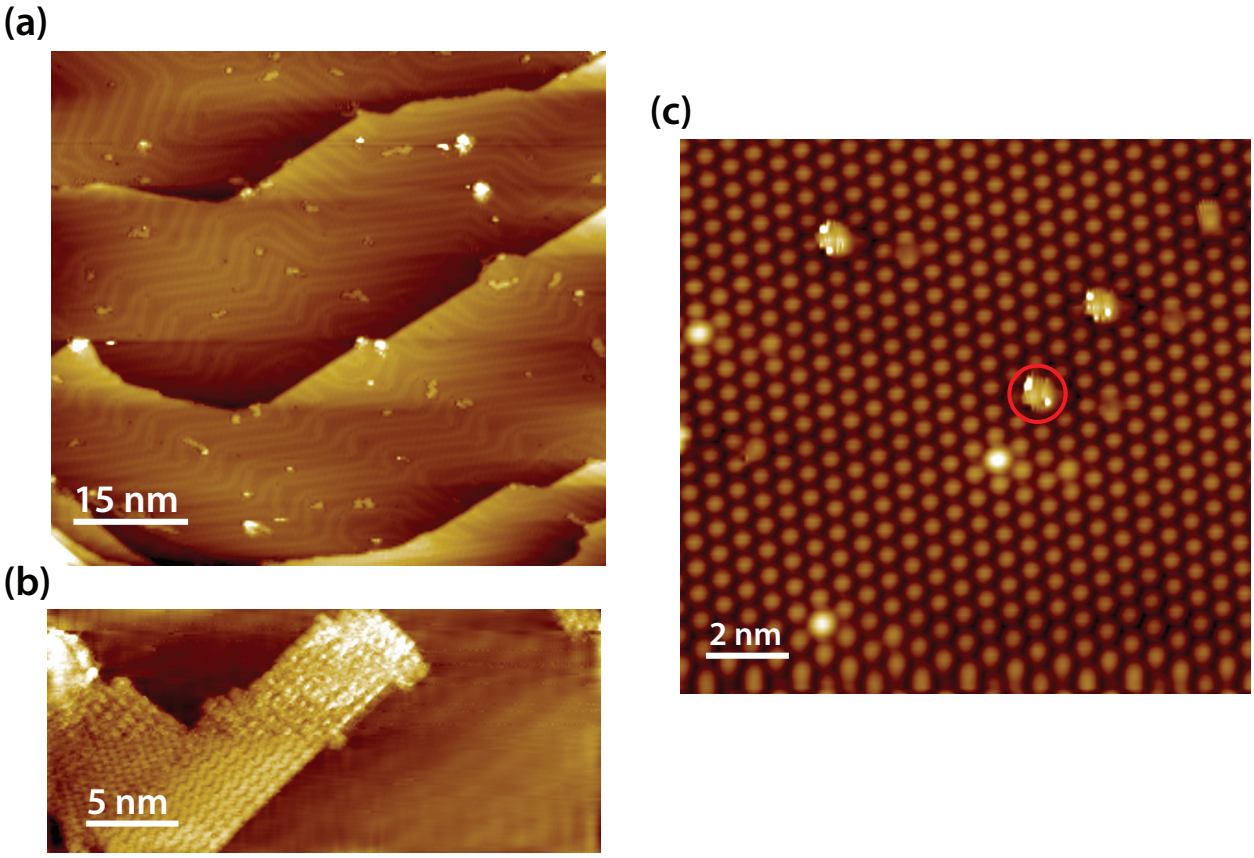

Figure 5.2: (a) STM image of the bare Au(111) surface showing the herringbone reconstruction. Bright spots are small areas of disorder. (b) The Au(111) surface after deposition of F4-TCNQ. The molecule network is observed as a 'zigzag' pattern. (c) The most heavily p-type doped Si(111) surface with a small amount of F4-TCNQ deposited. One of the molecules is marked by a red circle. Tunneling parameters are (a) -0.5 V 500 pA (b) -1.5 V 500 pA. (c) +2.0 V 30 pA.

4. The system is quickly pumped back down.

5. The chamber is baked out again, but this time at low temperature ($\sim 90^\circ$ C).

After the completion of this procedure, no signs of F4-TCNQ molecules are found on the inside of the chamber, and the LT-STM base pressure is found to be 3×10^{-11} mbar.

For an initial test of the custom effusion cell, epitaxial gold Au(111) thin films grown on mica substrates were purchased from PHASIS. Samples were prepared by repetitive cycles of Ar+ sputtering and annealing at $\sim 500^\circ$ C in the metal MBE chamber. Figure 5.2(a) shows the surface after ten cycles. Although the surface still shows some signs of disorder,

the well-known ($\sqrt{22} \times \sqrt{3}$) 'herringbone' reconstruction composes a majority of the surface (Takeuchi *et al.* , 1991). F4-TCNQ molecules (97%, Aldrich) were then deposited onto the clean Au(111) surface kept at room temperature and held by the LT-STM wobblestick over the effusion cell for several seconds. The effusion cell was kept at a sublimation temperature of ∼340 K. After this deposition, no further annealing was carried out, and the sample was placed inside the cold LT-STM cryostat. The STM topography of the as-deposited surface in Figure 5.2(b) shows a network of F4-TCNQ molecules (as described in Faraggi *et al.* (2012); Wang *et al.* (2016)). This confirms that the above procedure and custom effusion cell fits the requirements for this study: The deposition rate is ∼1 ML/minute and the deposited molecules are free from contaminants. The molecules were then deposited onto the most heavily p-type doped Si(111) substrate for a final calibration (details on this surface are given in Section 3.3). The surface with a small amount of F4-TCNQ is shown in Figure 5.2(c). The molecules appear more or less round with two bright spots that reflect the symmetry of the molecule (one of the molecules is marked by a red circle).

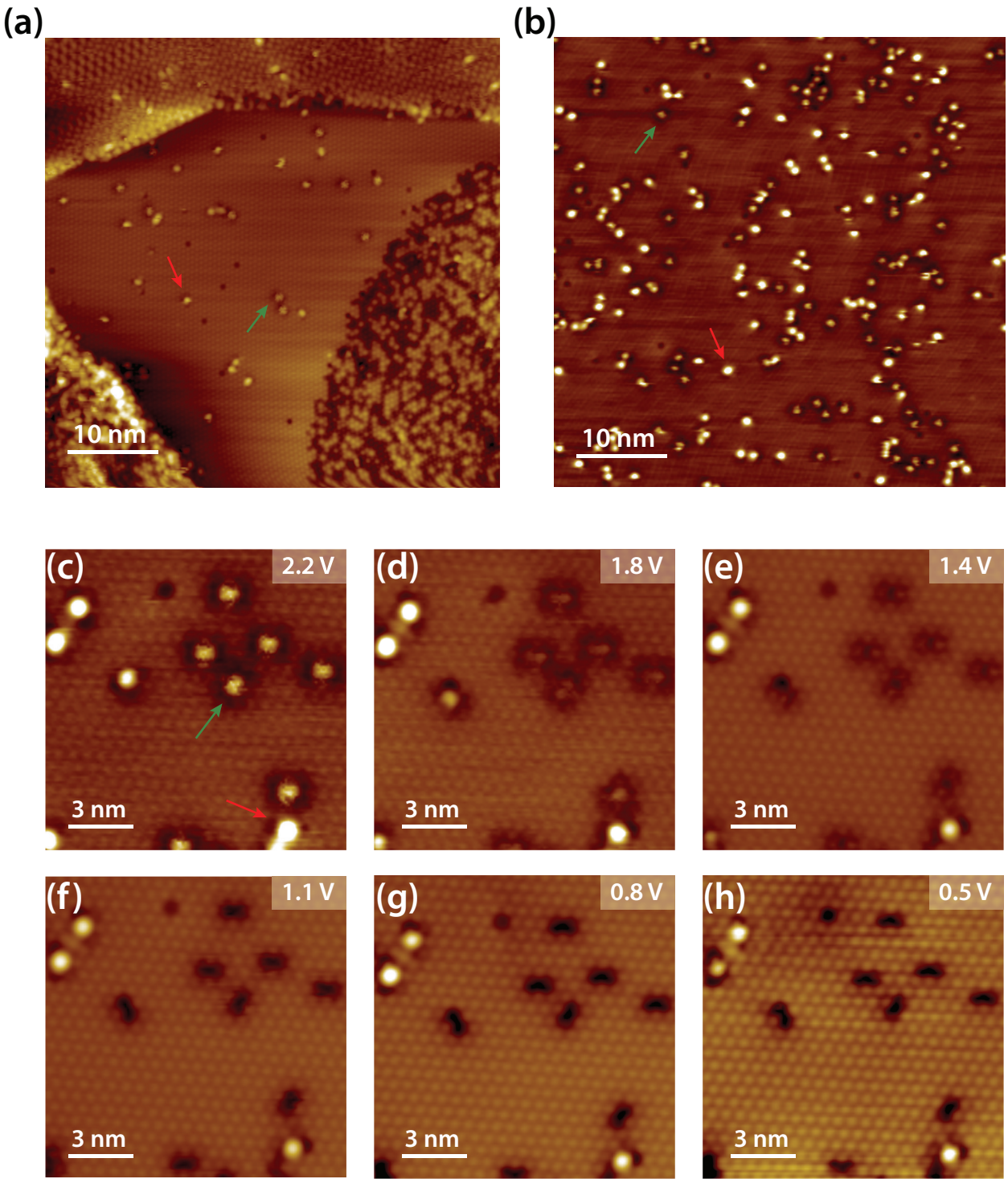

Figure 5.3: STM topography image of the F4-TCNQ decorated ($\sqrt{3}\times\sqrt{3}$) R30°-Sn surface on the (a) most heavily doped p-type and (b) most heavily doped n-type substrate (c)-(h) Bias dependent STM topography on the most heavily doped p-type surface, indicating a contrast inversion of the "rattling" F4-TCNQ molecules (marked by green arrows), while the "bright" molecules (marked by red arrows) remain relatively unchanged. Image parameters are (a) +2.5 V 30 pA (b) +2.5 V 10 pA (c)-(h) 10 pA.

The F4-TCNQ molecules were then deposited onto the grown Si(111)-($\sqrt{3}\times\sqrt{3}$) R30°-Sn surface on both the most heavily doped p-type and n-type samples. Figure 5.3 summarizes the observations on both molecule-decorated surfaces. It is first observed that the molecules tend to bond to defect sites first until the defects are nearly saturated and then begin to sit on top of the ($\sqrt{3}\times\sqrt{3}$) lattice. The molecules on defects appear brighter on the surface, while the molecules that are frozen on top of the Sn lattice appear slightly dimmer with an apparent "rattling" behavior. These are marked by red and green arrows in Figure 5.3, respectively. The ($\sqrt{3}\times\sqrt{3}$) domains on the most heavily p-type doped substrate tend to have fewer defects. Fewer molecules are therefore needed to be deposited on this surface in order to see the "rattling" molecules (Figure 5.3(a)). On the other hand, the most heavily doped n-type sample has a higher defect density, so more F4-TCNQ molecules are required for both molecule configurations to exist (Figure 5.3(b)).

A more detailed study of these two types of molecule configurations on the surface is performed by bias-dependent STM, where the differences become much clearer. A few of these images are shown in panels (c)-(h) in Figure 5.3. Starting at V_s=+2.2 V, the molecules appear as described previously. As the tunneling bias is reduced, the "rattling" molecules begin to appear as dumbbells, similar to their appearance on graphene (Kumar *et al.* , 2017). The molecules then undergo a contrast inversion at ∼+1.4 V . In the smallest bias measured, these molecules appear only as dark dumbbell-shaped defects on the surface, indicating that the molecule does not contain enough electronic density to tunnel at this bias. Attempts to measure the surface in the occupied states are not successful, possibly due to the F4-TCNQ molecules being dragged by the tip in these conditions. Notably, no contrast or shape change of the bright molecules is observed throughout these bias changes.

Spectroscopy results for the two types of molecule on the most heavily doped p-type substrate are given in Figure 5.4. The numbers corresponding to each curve indicate the number of Sn atomic distances from the molecule. The "rattling" molecules in panel (a) show a negligible effect on the LDOS near the molecule. However, STS directly next to the molecule (labeled '1') begins to show a suppression of the negative differential resistance (NDR) effect at about +1.0 V by a small peak, and another peak at -1.25 V (new features are marked by a dashed gray line in Figure 5.4). These can be assigned to the highest

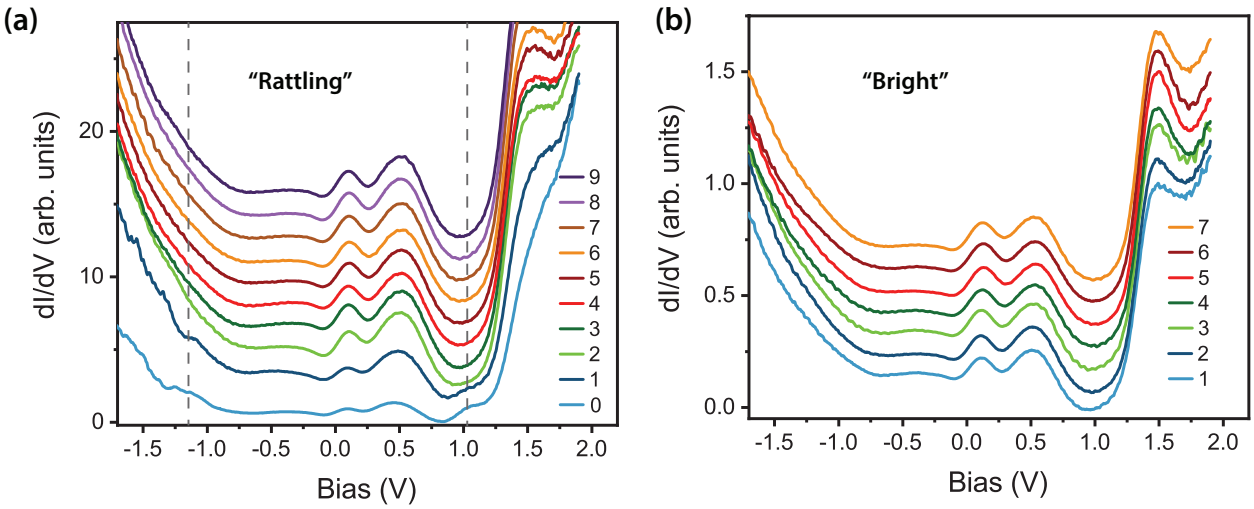

Figure 5.4: dI/dV spectra approaching the "rattling" (a) and "bright" (b) molecules on the most heavily doped p-type substrate. All curves are collected using the exact same tunneling conditions. The numbers for each curve indicate the number of Sn atomic distances from the molecule. Locations of new peaks close to the molecule are marked by a dashed gray line.

occupied molecular orbital (HOMO) and lowest unoccupied molecular orbital (LUMO) of the F4TCNQ molecule, which explains the loss of contrast on the F4TCNQ molecules between these biases. STS directly on the molecule shows only a drop in the overall intensity of the curve, with a slightly stronger signal at the two new peak locations. However, the QPP and UHB intensity ratios remain relatively constant throughout the measurement, indicating that there is no doping of the surface in this case. The same measurement is taken in the vicinity of a "bright" molecule (Figure 5.4)(b)). The LDOS remains unchanged, even in the vicinity of the molecule. The two new peaks that appear on the "rattling" molecule do not appear for this case. In addition, STS directly on the molecule is not possible, as the STS measurement tends to be very unstable on the bright molecule.

STS results on the most heavily doped n-type substrate are much more difficult. Shown for only the "bright" molecule in Figure 5.5, the QPP and UHB once again remain relatively the same. However, the two new peaks that appear near the molecule for the p-type case retain their approximate shape even fairly far away from the molecule. The I/V signal taken before these curves are differentiated also tend to show "spikes" in the signal, which

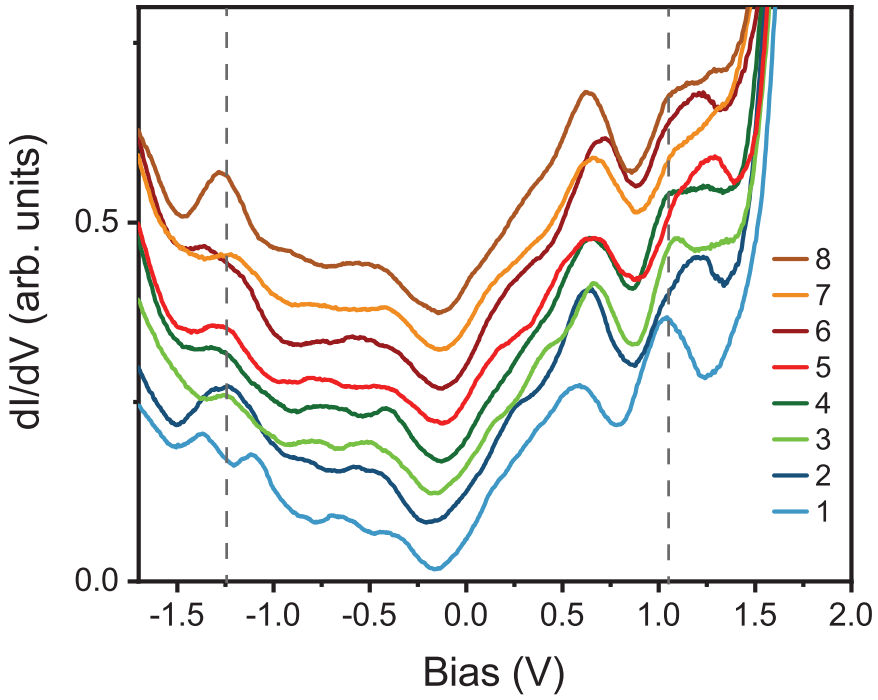

Figure 5.5: dI/dV spectra approaching a "bright" molecule on the most heavily doped n-type substrate. Details are as in Figure 5.4.

is often a sign of hopping or diffusing molecules. This is possibly due to the higher density of F4-TCNQ molecules needed for this surface. Indeed, it is seen that with more F4-TCNQ deposition, the molecules begin to diffuse, even at the low temperature of 4.5 K (not shown).

With this set of data, it is clear that the F4-TCNQ molecules are not accepting electronic charge from the surface. The hallmark of doped Mott physics seen in the modulation doping experiment is not observed, and the effect of the F4-TCNQ molecules seems to be highly local. The very small differences in the electronic structure near the molecules do appear to affect the overall ground state of the Si(111)-($\sqrt{3} \times \sqrt{3}$) R30°-Sn surface reconstruction. Other methods of doping the surface further will need to be explored. Possible avenues include using additional boron dopant enrichment methods, such as using B, BO_2 or $B_{10}H_{14}$ as the source material (see Weitering *et al.* (1993) and Lyo *et al.* (1989)) . This could conceivably lead to a larger subsurface boron concentration and a higher modulation doping.

Chapter 6

Summary and Outlook for Future Research

In this thesis, we studied the effects of adsorbates on the α-phases on Si(111). Following the success of modulation hole doping of the Sn/Si(111) system that ultimately led to the observation of a new superconducting state, adsorbate doping this system with electron-donating alkali species revealed a charge-ordering transition as the alkali adatoms condense at specific lattice locations and form a well-ordered honeycomb lattice. This led to unprecedented insights into the interplay between dopant site, dopant diffusion, and the charge ordering of the host lattice. In addition, it provided a unique insight into the process of sublattice melting in 2D. Potassium adatoms were also deposited onto the iso-electronic Pb/Si(111) interface. Remarkably, the surface morphology of this system was found to be identical to the Sn/Si(111) case, except for a rigid Fermi level shift of +0.3 V, which is indicative of a surface doping effect. Moreover, ARPES studies on this same surface revealed flat-band like conditions within the kagome sublattice formed by the Sn up atoms that are interesting candidates for future doping experiments.

The undoped Pb/Si(111) system was also studied, where a novel MBE method was synthesized in order to create large domains of the α-phase on this system. Significant support was found for a *1 up 2 down* charge ordered ground state, both from spectroscopy and by comparing the extracted dispersion from Quasiparticle Interference imaging by STM. The data also was in good agreement with the GGA+U calculation in Tresca *et al.* (2018),

emphasizing the importance of the Hubbard U for a proper description of the (3x3)-Pb system. Elemental Mn adatoms were then deposited on this surface to ascertain possible spin texture for the Pb/Si(111) ground state, also predicted by Tresca *et al.* (2018). Our QPI experiments revealed new features indicative of possible time reversal symmetry breaking, with evidence for some degree of spin texture. Though our results do not rule out the predictions from Tresca et al. , the new observations do not seem to be fully explained by the calculated ground state. Further work is needed to fully elucidate the origin of our experimental data.

Finally, adsorbate molecules were then attempted to be used in an attempt to further hole dope the Sn/Si(111) system. F4-TCNQ molecules were deposited at low temperature, and were found to weakly interact with the Sn dangling bonds and as a result did not modify the local electronic structure.

There are still many open questions that requires further experimental and theoretical study. Only a few are provided here. First, as discussed in Chapter 3, the adsorbate doping scheme is very difficult to implement without introducing structural complications. Adsorbates may create defects and destabilize the parent phases, as observed on the K/Sn/Si(111) case. Meanwhile, the subsurface doping scheme is limited by the solid solubility of the dopant species in the silicon substrate, and has only been successful for hole doping. Other modulation doping schemes will have to be explored in order to enhance the superconducting temperature of the hole-doped Sn/Si(111) system, and/or to realize electron doping without introducing structural modifications into the parent phase.

Possible avenues for further hole doping studies were given in Chapter 5 using additional boron dopant enrichment methods, such as using B, BO_2 or $B_{10}H_{14}$ as the source material (see Weitering *et al.* (1993) and Lyo *et al.* (1989)). Additionally, surfactant methods can be used to enrich the Si(111) substrate with higher subsurface electron donors, such as arsenic (Dubon *et al.* , 2001). Secondly, the identical morphology of the Pb and Sn α-phases on Si(111) after the deposition of potassium motivates possible growth studies on the isoelectronic α-phases on Ge(111). In the present study, we found that the Fermi level locations can vary across the band gap, and it is quite possible that a similar effect can be seen on the Ge(111) surface. This shift is likely related to surface doping, and with

the smaller band gap of the Ge(111) substrate, it is possible that the flat bands associated with the kagome sublattice could be doped. The latter could lead to exotic magnetism or superconductivity (Wen *et al.* , 2019b). Lastly, it is clear that more theoretical work must be done to correctly describe the ground state of the Pb/Si(111) system. The clear signs of new features in the QPI images after depositing magnetic scattering centers is a "smoking gun" of a spin-split ground state. However, QPI simulations using the Rashba spin split ground state suggested by Tresca *et al.* (2018) does not agree with our observations.

Despite these open questions, the studies in this work on the Pb and Sn α-phases on Si(111) answered many questions posed at the beginning. The alkali atoms clearly dope the Sn sublattice by transferring their 4s electrons to the dangling bonds of the Sn adatoms. They also induce a structural relaxation and condensation into a charge-ordered ground state. The study allowed a first-ever atomically resolved insight into 2D sublattice melting. The observed two-step melting process supports the predictions of KTHNY theory, with an intermediate phase defined by quasi-long-range order. Additionally, our study of the Pb/Si(111) system confirmed the existence of a spin-split ground state. The QPI results on this surface pose further questions regarding its spin texture. Future studies on related surface systems on simple semiconductor platforms, including 2D Mott insulators and charge ordered metals and insulators, may lead to detailed understanding between the electronic, structural, and spin degrees of freedom in these strictly 2D materials systems.

Bibliography

Adler, F, Rachel, S, Laubach, M, Maklar, J, Fleszar, A, Schäfer, J, & Claessen, R. 2019. Correlation-Driven Charge Order in a Frustrated Two-Dimensional Atom Lattice. *Phys. Rev. Lett.*, **123**(8), 086401. 7, 76, 83, 92

Allan, M P, Rost, A W, Mackenzie, A P, Xie, Yang, Davis, J C, Kihou, K, Lee, C H, Iyo, A, Eisaki, H, & Chuang, T M. 2012. Anisotropic Energy Gaps of Iron-based Superconductivity from Intra-band Quasiparticle Interference in LiFeAs. *Science*, **336**(563). 134

Avella, Adolfo, & Mancini, Ferdinando. 2013. *Strongly Correlated Systems*. Experimental Methods. Springer Science & Business Media. 26, 29

Bardeen, J. 1961. Tunnelling from a Many-Particle Point of View. *Phys. Rev. Lett.*, **6**(2), 57–59. 18, 20

Bardeen, J, & Brattain, W H. 1948. The Transistor, A Semi-Conductor Triode. *Phys. Rev. B*, **74**(2), 230–231. 1

Bechstedt, Friedhelm. 2012. *Principles of Surface Physics*. Springer Science & Business Media. 3

Bedrossian, P, Meade, Robert D, Mortensen, K, Chen, D M, Golovchenko, J A, & Vanderbilt, David. 1989. Surface doping and stabilization of Si(111) with boron. *Phys. Rev. Lett.*, **63**(12), 1257–1260. 36

Bena, Cristina. 2016. Friedel oscillations: Decoding the hidden physics. *Comptes Rendus Physique*, **17**(3-4), 302–321. 99, 100

Bernard, Etienne P, & Krauth, Werner. 2011. Two-step melting in two dimensions: First-order liquid-hexatic transition. *Phys. Rev. Lett.*, **107**(155704). 62

Bilitewski, Thomas, & Moessner, Roderich. 2018. Disordered flat bands on the kagome lattice. *Phys. Rev. B*, **98**(235109). 63, 64

Binnig, G, & Rohrer, H. 1982. Scanning Tunneling Microscopy. *Surface Science*, **126**(Sept.), 236–244. 15

Brihuega, I, Custance, O, Pérez, Rubén, & Gómez-Rodríguez, J M. 2005. Intrinsic Character of the 3×3 to $\sqrt{3} \times \sqrt{3}$ Phase Transition in Pb/Si(111). *Phys. Rev. Lett.*, **94**(4), 046101. 5, 82

Brihuega, I, Custance, O, Ugeda, M M, & Gómez-Rodríguez, J M. 2007. Defects in the $3 \times 3 \Leftrightarrow \sqrt{3} \times \sqrt{3}$ phase transition in the Pb/Si(111)system. *Phys. Rev. B*, **75**(15), 1399. 79, 85

Brochard, S, Artacho, Emilio, Custance, O, Brihuega, I, Baró, A M, Soler, J M, & Gómez-Rodríguez, J M. 2002. Ab initiocalculations and scanning tunneling microscopy experiments of the Si(111)-$\sqrt{7} \times \sqrt{3}$-Pb surface. *Phys. Rev. B*, **66**(20), 7316. 79

Capriotti, L, Scalapino, D J, & Sedgewick, R D. 2003. Wave-vector power spectrum of the local tunneling density of states: Ripples in a d-wave sea. *Phys. Rev. B*, **68**(1), 3363–15. 88

Carpinelli, J M, Weitering, H H, Bartkowiak, M, Stumpf, R, & Plummer, E W. 1997. Surface charge ordering transition: α phase of Sn/Ge(111). *Phys. Rev. Lett.*, **79**(15), 2859–2862. 4, 43, 49

Carpinelli, Joseph M, Weitering, Hanno H, Ward Plummer, E, & Stumpf, Roland. 1996. Direct observation of a surface charge density wave. *Nature*, **381**(6581), 398–400. 4, 30

Chang, Leroy L, & Ploog, Klaus. 1985. *Molecular Beam Epitaxy and Heterostructures*. Dordrecht, The Netherlands: Martinus Nijhoff Publishers. 35

Chen, C Julian. 2008. *Introduction to scanning tunneling microscopy; 2nd ed.* Monographs on the physics and chemistry of materials. Oxford: Oxford University Press. 18

Cortés, R, Tejeda, A, Lobo, J, Kierren, B, Malterre, D, Michel, E G, & Mascaraque, A. 2006. Observation of a Mott Insulating Ground State for Sn/Ge(111) at Low Temperature. *Phys. Rev. Lett.*, **96**(126103), 126103–1–126103–4. 30

Cortés, R, Tejeda, A, Lobo-Checa, J, Didiot, C, Kierren, B, Malterre, D, Merino, J, Flores, F, Michel, E G, & Mascaraque, A. 2013. Competing charge ordering and Mott phases in a

correlated Sn/Ge(111) two-dimensional triangular lattice. *Phys. Rev. B*, **88**(12), 125113. 30, 74, 82

Crommie, M F, Lutz, C P, & Eigler, D M. 1993. Imaging standing waves in a two-dimensional electron gas. *Nature*, **363**(6429), 524–527. 21

Custance, O, Gómez-Rodriguez, J M, Baró, A M, Juré, L, Mallet, P, & Veuillen, J Y. 2001. Low temperature phases of Pb/Si(111). *Surface Science*, **482-485**(June), 1399–1405. 79

Damascelli, Andrea, Hussain, Zahid, & Shen, Zhi-Xun. 2003. Angle-resolved photoemission studies of the cuprate superconductors. *Reviews of Modern Physics*, **75**(2), 473–541. 6

Dávila, M E, Avila, J, Asensio, M C, & Le Lay, G. 2004. Giant effect of electron and hole donation on Sn/Ge(111) and Sn/Si(111) surfaces. *Physical Review B - Condensed Matter and Materials Physics*, **70**(24), 1–4. 83

Dubon, O D, Evans, P G, Chervinsky, J F, Aziz, M J, Spaepen, F, Golovchenko, J A, Chisholm, M F, & Muller, D A. 2001. Doping by metal-mediated epitaxy: Growth of As delta-doped Si through a Pb monolayer. *Appl. Phys. Lett.*, **78**(11), 1505–1507. 117

Dudr, Viktor, Tsud, Natalia, Fabík, Stanislav, Vondráček, Martin, Matolín, Vladimír, Cháb, Vladimír, & Prince, Kevin C. 2004. Evidence for valence-charge fluctuations in the $\sqrt{3} \times \sqrt{3}$-Pb/Si(111) system. *Physical Review B - Condensed Matter and Materials Physics*, **70**(15), R14. 49

Eskes, H, Meinders, M B J, & Sawatzky, G A. 1991. Anomalous transfer of spectral weight in doped strongly correlated systems. *Phys. Rev. Lett.*, **67**(8), 1035–1038. 34, 35

Faraggi, Marisa N, Jiang, Nan, Gonzalez-Lakunza, Nora, Langner, Alexander, Stepanow, Sebastian, Kern, Klaus, & Arnau, Andres. 2012. Bonding and Charge Transfer in Metal–Organic Coordination Networks on Au(111) with Strong Acceptor Molecules. *J. Phys. Chem. C*, **116**(46), 24558–24565. 111

Fert, Albert, & Van Dau, Frédéric Nguyen. 2019. Spintronics, from giant magnetoresistance to magnetic skyrmions and topological insulators. *Comptes Rendus Physique*, **20**(7-8), 817–831. 2

Friedel, J. 1958. Metallic alloys. *Nuovo Cim*, **7**(S2), 287–311. 21

Garza, Alejandro J, & Scuseria, Gustavo E. 2016. Predicting Band Gaps with Hybrid Density Functionals. *J. Phys. Chem. Lett.*, **7**(20), 4165–4170. 57

Goldoni, A, & Modesti, S. 1997. Strong correlation effects in the (3×3) charge density wave phase of Sn/Ge(111). *Phys. Rev. Lett.*, **79**(17), 3266–3269. 30

González, Rafael C, & Woods, Richard E. 2002. *Digital Image Processing*. Prentice Hall. 96

Griffiths, David J. 2017. *Introduction to Quantum Mechanics*. Cambridge University Press. 17

Grothe, S, Johnston, S, Chi, Shun, Dosanjh, P, Burke, S A, & Pennec, Y. 2013. Quantifying Many-Body Effects by High-Resolution Fourier Transform Scanning Tunneling Spectroscopy. *Phys. Rev. Lett.*, **111**(246804). 22

Halperin, B I, & Nelson, David R. 1978. Theory of Two-Dimensional melting. *Phys. Rev. Lett.*, **41**(2), 121–124. 7, 62

Han, Wei, Otani, YoshiChika, & Maekawa, Sadamichi. 2018. Quantum materials for spin and charge conversion. *npj Quantum Mater.*, May, 1–16. 3

Hansmann, Philipp, Ayral, Thomas, Vaugier, Loig, Werner, Philipp, & Biermann, Silke. 2013. Long-range Coulomb interactions in surface systems: a first principles description within self-consistently combined GW and dynamical mean field theory. *Phys. Rev. Lett.*, **110**(Jan.), 166401. 74

Hasegawa, Y, & Avouris, Ph. 1993. Direct observation of standing wave formation at surface steps using scanning tunneling spectroscopy. *Phys. Rev. Lett.*, **71**(7), 1071–1074. 21

Hasnip, Philip J, Refson, Keith, Probert, Matt I J, Yates, Jonathan R, Clark, Stewart J, & Pickard, Chris J. 2014. Density functional theory in the solid state. *Phil. Trans. R. Soc. A*, **372**(2011), 20130270–26. 57

Headrick, R L, Robinson, I K, Vlieg, E, & Feldman, L C. 1989. Structure determination of the Si(111):B($\sqrt{3} \times \sqrt{3}$) R30° surface: Subsurface substitutional doping. *Phys. Rev. Lett.*, **63**(12), 1253–1256. 36

Hoffman, Jennifer Eve. 2003. *A Search for Alternative Electronic Order in the High Temperature Superconductor Bi2Sr2CaCu2O8+[delta] by Scanning Tunneling Microscopy.* 87

Hossain, M A, Mottershead, J D F, Fournier, D, Bostwick, A, McChesney, J L, Rotenberg, E, Liang, R, Hardy, W N, Sawatzky, G A, Elfimov, I S, Bonn, D A, & Damascelli, A. 2008. In situ doping control of the surface of high-temperature superconductors. *Nature Physics*, **4**(7), 527–531. 39

Huang, H, Tong, S Y, Quinn, J, & Jona, F. 1990. Atomic structure of Si(111) ($\sqrt{3} \times \sqrt{3}$) R30°-B by dynamical low-energy electron diffraction. *Phys. Rev. B*, **41**(5), 3276–3279. 36

Hüfner, Stefan. 2013. *Photoelectron Spectroscopy.* Principles and Applications. Springer Science & Business Media. 25

Iglovikov, V I, Hébert, F, Grémaud, B, Batrouni, G G, & Scalettar, R T. 2014. Superconducting transitions in flat-band systems. *Phys. Rev. B*, **90**(9), 094506–6. 64

Imada, Masatoshi, Fujimori, Atsushi, & Tokura, Yoshinori. 1998. Metal-insulator transitions. *Reviews of Modern Physics*, **70**(4), 1039–1263. 33

Kang, Mingu, Fang, Shiang, Ye, Linda, Po, Hoi Chun, Denlinger, Jonathan, Jozwiak, Chris, Bostwick, Aaron, Rotenberg, Eli, Kaxiras, Efthimios, Checkelsky, Joseph G, & Comin, Riccardo. 2020. Topological flat bands in frustrated kagome lattice CoSn. *arXiv*, Feb. 63, 64, 65

Kauppila, V J, Aikebaier, F, & Heikkilä, T T. 2016. Flat band superconductivity in strained Dirac materials. *arXiv*, Jan. 64

Keyes, Robert W. 2005. Physical limits of silicon transistors and circuits. *Rep. Prog. Phys.*, **68**(1), 2701–2746. 2

Kilby, Jack. 1964 (June). *Miniaturized Electronic Circuits*. 1

Kim, Keun Su, Jung, Sung Chul, Kang, Myung Ho, & Yeom, Han Woong. 2010. Nearly massless electrons in the silicon interface with a metal film. *Phys. Rev. Lett.*, **104**(24), 246803. 23

Knudsen, Martin. 1934. *The Kinetic Theory of Gases*. 12

Kohsaka, Y, Machida, T, Iwaya, K, Kanou, M, Hanaguri, T, & Sasagawa, T. 2017. Spin-orbit scattering visualized in quasiparticle interference. *Phys. Rev. B*, **95**(11), 78–9. 93, 101

Kosterlitz, J M, & Thouless, D J. 1973. Ordering, metastability and phase transitions in two-dimensional systems. *J. Phys. C: Solid State Phys.*, **6**(7), 1181–1203. 7, 62

Krantz, Philip, Kjaergaard, Morten, Yan, Fei, Orlando, Terry P, Gustavsson, Simon, & Oliver, William D. 2019. A Quantum Engineer's Guide to Superconducting Qubits. *Appl. Phys. Lett.*, June, 021318. 3

Kumar, Avijit, Banerjee, Kaustuv, Dvorak, Marc, Schulz, Fabian, Harju, Ari, Rinke, Patrick, & Liljeroth, Peter. 2017. Charge-Transfer-Driven Nonplanar Adsorption of F 4TCNQ Molecules on Epitaxial Graphene. *ACS Nano*, **11**(5), 4960–4968. 10, 108, 113

Lee, Patrick A, Nagaosa, Naoto, & Wen, Xiao-Gang. 2006. Doping a Mott insulator: Physics of high-temperature superconductivity. *Reviews of Modern Physics*, **78**(1), 17–85. 6

Li, C H, van 't Erve, O M J, Rajput, S, Li, L, & Jonker, B T. 2016. Direct comparison of current-induced spin polarization in topological insulator Bi2Se3 and InAs Rashba states. *Nature Communications*, **7**(13518), 1–8. 3

Li, Gang, Höpfner, Philipp, Schäfer, Jörg, Blumenstein, Christian, Meyer, Sebastian, Bostwick, Aaron, Rotenberg, Eli, Claessen, Ralph, & Hanke, Werner. 2013. Magnetic order in a frustrated two-dimensional atom lattice at a semiconductor surface. *Nature Communications*, **4**(1), 1196. 5, 30, 101

Li, Guohong, Luican, A, dos Santos, J M B Lopes, Neto, A H Castro, Reina, A, Kong, J, & Andrei, E Y. 2010. Observation of Van Hove singularities in twisted graphene layers. *Nature Physics*, Jan., 1–5. 37

Li, Zhi, Zhuang, Jincheng, Wang, Li, Feng, Haifeng, Gao, Qian, Xu, Xun, Hao, Weichang, Wang, Xiaolin, Zhang, Chao, Wu, Kehui, Dou, Shi Xue, Chen, Lan, Hu, Zhenpeng, & Du, Yi. 2018. Realization of flat band with possible nontrivial topology in electronic Kagome lattice. *Sci. Adv.*, **4**(11), eaau4511. 64

Liehr, M, Renier, M, Wachnik, R A, & Scilla, G S. 1987. Dopant redistribution at Si surfaces during vacuum anneal. *Journal of Applied Physics*, **61**(9), 4619–4625. 39

Liu, D F, Liang, A J, Liu, E K, Xu, Q N, Li, Y W, Chen, C, Pei, D, Shi, W J, Mo, S K, Dudin, P, Kim, T, Cacho, C, Li, G, Sun, Y, Yang, L X, Liu, Z K, Parkin, S S P, Felser, C, & Chen, Y L. 2019. Magnetic Weyl semimetal phase in a Kagome crystal. *Science*, **365**(6), 1282–1285. 64

Lyo, I W, Kaxiras, Efthimios, & Avouris, Ph. 1989. Adsorption of boron on Si(111): Its effect on surface electronic states and reconstruction. *Phys. Rev. Lett.*, **63**(12), 1261–1264. 115, 117

Mans, A, Dil, J H, Ettema, A R H F, & Weitering, H H. 2005. Surface relaxations in quantum-confined Pb. *Phys. Rev. B*, **72**(15), 115406. 77

McEllistrem, M, Haase, G, Chen, D, & Hamers, R J. 1993. Electrostatic sample-tip interactions in the scanning tunneling microscope. *Phys. Rev. Lett.*, **70**(16), 2471–2474. 71

Meinders, M B J, Eskes, H, & Sawatzky, G A. 1993. Spectral-weight transfer: Breakdown of low-energy-scale sum rules in correlated systems. *Phys. Rev. B*, **48**(6), 3916–3926. 34, 35

Michailov, Michail. 2011. *Nanophenomena at surfaces: fundamentals of exotic condensed matter phenomena*. Springer Series in Surface Sciences. Dordrecht: Springer. 77

Mii, Takashi, Shima, Nobuyuki, Kano, Koichi, & Makoshi, Kenji. 2014. Spin–Orbit Interaction in the Tight-Binding Model —Toward the Comprehension of the Rashba Effect at Surfaces—. *J. Phys. Soc. Jpn.*, **83**(6), 064706–4. 102

Ming, Fangfei, Johnston, Steve, Mulugeta, Daniel, Smith, Tyler S, Vilmercati, Paolo, Lee, Geunseop, Maier, Thomas A, Snijders, Paul C, & Weitering, Hanno H. 2017. Realization of a Hole-Doped Mott Insulator on a Triangular Silicon Lattice. *Phys. Rev. Lett.*, **119**(26), 266802–6. 5, 33, 36, 108, 134

Modesti, S, Petaccia, L, Ceballos, G, Vobornik, I, Panaccione, G, Rossi, G, Ottaviano, L, Larciprete, R, Lizzit, S, & Goldoni, A. 2007. Insulating ground state of Sn/Si(111)-(3×3) $R30°$. *Phys. Rev. Lett.*, **98**(12), 126401. 30

Moser, Simon. 2017. An experimentalist's guide to the matrix element in angle resolved photoemission. *Journal of Electron Spectroscopy and Related Phenomena*, **214**(Jan.), 29–52. 65

Noyce, Robert. 1964 (Jan.). *Semiconductor Circuit Complexes*. 1

Okada, Yoshinori, Dhital, Chetan, Zhou, Wenwen, Huemiller, Erik D, Lin, Hsin, Basak, S, Bansil, A, Huang, Y B, Ding, H, Wang, Z, Wilson, Stephen D, & Madhavan, V. 2011. Direct Observation of Broken Time Reversal Symmetry on the Surface of a Magnetically Doped Topological Insulator. *Phys. Rev. Lett.*, **106**(20), 206805–4. 23, 93

Oppenheim, Alan V, Willsky, Alan S, & Nawab, Syed Hamid. 1997. *Signals and Systems*. Prentice Hall International. 87

Ortega, José, Pérez, Rubén, & Flores, Fernando. 2002. Dynamical fluctuations and the $\sqrt{3} \times \sqrt{3} \leftrightarrow 3 \times 3$ transition in α-Sn/Ge(111) and Sn/Si(111). *Journal of Physics: Condensed Matter*, **14**(24), 5979–6004. 4, 30, 74, 83

Oura, K, Lifshits, V G, Saranin, Alexander, Zotov, A V, & Katayama, M. 2010. *Surface Science*. An Introduction. Springer. xi, 14, 24, 26, 27

Özer, Murat. 2006 (Jan.). *Growth and Superconductivity of Pb and Pb-Bi Alloys in the Quantum Regime*. Ph.D. thesis, University of Tennessee, University of Tennessee. 76

Özer, Mustafa M, Jia, Yu, Wu, Biao, Zhang, Zhenyu, & Weitering, Hanno H. 2005. Quantum stability and reentrant bilayer-by-bilayer growth of atomically smooth Pb films on semiconductor substrates. *Phys. Rev. B*, **72**(1), 113409. 77

Palczewski, Ari Deibert. 2010 (Nov.). *Angle-resolved photemission spectroscopy (ARPES) studies of cuprate superconductors*. Ph.D. thesis, Iowa State University. 27

Pérez-mato, J M, Ivantchev, S, García, Alberto, & Etxebarria, I. 2000 (Jan.). Displacive vs. order-disorder in structural phase transitions. *Pages 93–103 of: Ferroelectrics*. Universidad del Pais Vasco - Euskal Herriko Unibertsitatea, Campus Bizkaia, Leioa, Spain. 62

Petersen, L, Sprunger, P T, Hofmann, Ph, Laegsgaard, E, Briner, B G, Doering, M, Rust, H P, Bradshaw, A M, Besenbacher, F, & Plummer, E W. 1998. Direct imaging of the two-dimensional Fermi contour : Fourier-transform STM. *Phys. Rev. B*, **57**(12), R6858–R6861. 22

Petersen, L, Hofmann, Ph, Plummer, E W, & Besenbacher, F. 2000. Fourier Transform-STM: Determining the surface Fermi contour. *Journal of Electron Spectroscopy and Related Phenomena*, **109**(1), 97–115. 21

Petersen, L, Ismail, & Plummer, E W. 2002. Defect-blurred two-dimensional phase transition. *Progress in Surface Science*, **71**(1), 1–29. 4

Piriou, A, Jenkins, N, Berthod, C, Maggio-Aprile, I, & Fischer, Ø. 2011. First direct observation of the Van Hove singularity in the tunnelling spectra of cuprates. *Nature Communications*, Feb., 1–5. 36, 37

Plat, Xavier, Momoi, Tsutomu, & Hotta, Chisa. 2018. Kinetic frustration induced supersolid in the $S = \frac{1}{2}$ kagome lattice antiferromagnet in a magnetic field. *Phys. Rev. B*, **98**(014415). 63

Profeta, G, & Tosatti, E. 2007. Triangular Mott-Hubbard insulator phases of Sn/Si(111) and Sn/Ge(111) surfaces. *Phys. Rev. Lett.*, **98**(8), 381. 4, 5, 30

Sato, Masatoshi, & Ando, Yoichi. 2017. Topological superconductors: a review. *Rep. Prog. Phys.*, **80**(7), 076501–43. 3

Segawa, Kouji, Kofu, M, Lee, S-H, Tsukada, I, Hiraka, H, Fujita, M, Chang, S, Yamada, K, & Ando, Yoichi. 2010. Zero-doping state and electron–hole asymmetry in an ambipolar cuprate. *Nature Physics*, **6**(8), 579–583. 38

Shockley, William. 1951 (Sept.). *Circuit Element Utilizing Semiconductive Material*. 1

Slezák, J, Mutombo, P, & Cháb, V. 1999. Stm study of a pb/si(111) interface at room and low temperatures. *Physical Review B - Condensed Matter and Materials Physics*, **60**(19), 13328–13330. 79, 85

Smith, T S, Ming, F, Trabada, D G, González, C, Soler-Polo, D, Flores, F, Ortega, J, & Weitering, H H. 2020. Coupled Sublattice Melting and Charge-Order Transition in Two Dimensions. *Phys. Rev. Lett.*, **124**(9), 097602. 7, 8, 42, 56, 57, 66

Stewart, G R. 2017. Unconventional superconductivity. *Advances in Physics*, June, 75–196. 3

Stroscio, Joseph A, Feenstra, R M, Newns, D M, & Fein, A P. 1988. Voltage-dependent scanning tunneling microscopy imaging of semiconductor surfaces. *Journal of Vacuum Science & Technology A: Vacuum, Surfaces, and Films*, **6**(2), 499–507. 71

Stróżecka, Anna, Eiguren, Asier, & Pascual, Jose Ignacio. 2011. Quasiparticle Interference around a Magnetic Impurity on a Surface with Strong Spin-Orbit Coupling. *Phys. Rev. Lett.*, **107**(18), 186805–5. 93

Sutherland, Bill. 1986. Localization of electronic wave functions due to local topology. *Physical Review B (Condensed Matter)*, **34**(8), 5208–5211. 63

Takayanagi, K, Tanishiro, Y, Takahashi, M, & Takahashi, S. 1985. Structural analysis of Si(111)-7×7 by UHV-transmission electron diffraction and microscopy. *Journal of Vacuum Science & Technology A: Vacuum*, **3**(May), 1502–1506. 4

Takeuchi, Noboru, Chan, C T, & Ho, K M. 1991. Au(111): A theoretical study of the surface reconstruction and the surface electronic structure. *Phys. Rev. B*, **43**(17), 13899–13906. 111

Tanaka, Yasunori, Morishita, Hideki, Ryu, Juang Tak, Katayama, Itsuo, & Oura, Kenjiro. 1996. The initial stage of Pb thin film growth on Si(111) surface studied by TOF-ICISS. *Nuclear Instruments and Methods in Physics Research, Section B: Beam Interactions with Materials and Atoms*, **118**(1-4), 530–532. 77

Tejeda, A, Cortés, R, Lobo, J, Michel, E G, & Mascaraque, A. 2007. The Fermi surface of Sn/Ge(111) and Pb/Ge(111). *Journal of Physics: Condensed Matter*, **19**(35), 355008. 30, 82

Tejeda, A, Cortés, R, Lobo-Checa, J, Didiot, C, Kierren, B, Malterre, D, Michel, E G, & Mascaraque, A. 2008. Structural Origin of the Sn 4dCore Level Line Shape in Sn/Ge(111)-3×3 . *Phys. Rev. Lett.*, **100**(2). 30

Tersoff, J, & Hamann, D R. 1983. Theory and application for the scanning tunneling microscope. *Phys. Rev. Lett.*, **50**(25), 1998–2001. 19

Tersoff, J, & Hamann, D R. 1985. Theory of the scanning tunneling microscope. *Phys. Rev. B*, **31**(2), 805–813. 19

Tokura, Yoshinori, Kawasaki, Masashi, & Nagaosa, Naoto. 2017. Emergent functions of quantum materials. *Nature Physics*, **13**(1), 1056–1068. 2

Tosatti, E, Bertel, E, & Donath, M. 1995. *Electronic Surface and Interface States on Metallic Systems*. WORLD SCIENTIFIC. 7

Tresca, C, Brun, C, Bilgeri, T, Menard, G, Cherkez, V, Federicci, R, Longo, D, Debontridder, F, D'angelo, M, Roditchev, D, Profeta, G, Calandra, M, & Cren, T. 2018. Chiral

Spin Texture in the Charge-Density-Wave Phase of the Correlated Metallic Pb/Si(111) Monolayer. *Phys. Rev. Lett.*, **120**(19), 196402. xiii, xiv, 5, 7, 9, 74, 75, 76, 83, 89, 91, 92, 96, 98, 99, 101, 102, 104, 107, 116, 117, 118

Wang, Wan-Sheng, Li, Zheng-Zhao, Xiang, Yuan-Yuan, & Wang, Qiang-Hua. 2013. Competing electronic orders on kagome lattices at van Hove filling. *Phys. Rev. B*, **87**(11), 115135–8. 65

Wang, Xiaoming, Esfarjani, Keivan, & Zebarjadi, Mona. 2016. Charge transfer at hybrid inorganic-organic interfaces. *arXiv*, Oct., 15529–15537. 111

Weitering, H H, Chen, J, DiNardo, N J, & Plummer, E W. 1993. Electron correlation, metallization, and Fermi-level pinning at ultrathin K/Si(111) interfaces. *Phys. Rev. B*, **48**(11), 8119–8135. 39, 115, 117

Weitering, H H, Shi, X, Johnson, P D, Chen, J, DiNardo, N J, & Kempa, K. 1997a. Mott Insulating Ground State on a Triangular Surface Lattice. *Phys. Rev. Lett.*, **78**(7), 1331–1334. 4

Weitering, H H, Shi, X, Johnson, P D, Chen, J, DiNardo, N J, & Kempa, K. 1997b. Mott insulating ground state on a triangular surface lattice. *Phys. Rev. Lett.*, **78**(7), 1331–1334. 30

Wen, C H P, Xu, H C, Chen, C, Huang, Z C, Lou, X, Pu, Y J, Song, Q, Xie, B P, Abdel-Hafiez, Mahmoud, Chareev, D A, Vasiliev, A N, Peng, R, & Feng, D L. 2019a. Anomalous correlation effects and unique phase diagram of electron-doped FeSe revealed by photoemission spectroscopy. *Nature Communications*, Apr., 1–7. 39

Wen, Jinsheng, Yu, Shun-Li, Li, Shiyan, Yu, Weiqiang, & Li, Jian-Xin. 2019b. Experimental identification of quantum spin liquids. *npj Quantum Mater.*, **4**(1), 199. 72, 118

Wikipedia. 2020. *Moore's Law*. 2

Wu, Xuefeng, Ming, Fangfei, Smith, Tyler S, Liu, Guowei, Ye, Fei, Wang, Kedong, Johnston, Steven, & Weitering, Hanno H. 2019. Superconductivity in a hole-doped Mott-insulating triangular adatom layer on a silicon surface. *arXiv*, Dec. 5, 38

Yakes, M, & Tringides, M C. 2011. Probing the buried Pb/Si(111) interface with SPA LEED and STM on Si(111)-Pb $\alpha\sqrt{3}\times\sqrt{3}$. *Journal of Physical Chemistry A*, **115**(25), 7096–7104. 77

Ye, Linda, Kang, Mingu, Liu, Junwei, von Cube, Felix, Wicker, Christina R, Suzuki, Takehito, Jozwiak, Chris, Bostwick, Aaron, Rotenberg, Eli, Bell, David C, Fu, Liang, Comin, Riccardo, & Checkelsky, Joseph G. 2018. Massive Dirac fermions in a ferromagnetic kagome metal. *Nature*, Mar., 1–12. 64

Yoshizawa, Shunsuke, Nakamura, Fumitaka, Taskin, Alexey A, Iimori, Takushi, Nakatsuji, Kan, Matsuda, Iwao, Ando, Yoichi, & Komori, Fumio. 2015. Scanning tunneling spectroscopy study of quasiparticle interference on the dual topological insulator $Bi_{1-x}Sb_x$. *Phys. Rev. B*, **91**(4), 045423–6. 23, 93, 105

Young, A P. 1979. Melting and the vector Coulomb gas in two dimensions. *Phys. Rev. B*, **19**(4), 1855–1866. 7, 62

Zhang, Yi, Ugeda, Miguel M, Jin, Chenhao, Shi, Su-Fei, Bradley, Aaron J, Martín-Recio, Ana, Ryu, Hyejin, Kim, Jonghwan, Tang, Shujie, Kim, Yeongkwan, Zhou, Bo, Hwang, Choongyu, Chen, Yulin, Wang, Feng, Crommie, Michael F, Hussain, Zahid, Shen, Zhi-Xun, & Mo, Sung-Kwan. 2016. Electronic Structure, Surface Doping, and Optical Response in Epitaxial WSe 2Thin Films. *Nano Lett.*, **16**(4), 2485–2491. 39

Zhou, Xingjiang, He, Shaolong, Liu, Guodong, Zhao, Lin, Yu, Li, & Zhang, Wentao. 2018. New developments in laser-based photoemission spectroscopy and its scientific applications: A key issues review. *Rep. Prog. Phys.*, **81**(6). 28

Appendices

A Processing of QPI images

As mentioned in Section 4.3, QPI images were taken by collecting various tunneling conductance maps $g(\mathbf{r}, V)$. These were all collected at 4.5K at various rms voltages corresponding to the desired resolution for each tunneling conductance map, using a lock-in frequency of 831 Hz. Figure 1 shows a summary of QPI processing for three of these voltages: -20mV, -5mV, and +2mV. The first row shows $\frac{dI}{dV}$ conductance maps from the same surface area at these three biases. These images are then Fourier transformed. The wave-vector power spectrum calculated from these Fourier transforms (described in Section 4.3) is shown in the second row of Figure 1. This is followed by a distortion correction of the Fourier transforms to compensate for image distortion from drift or piezo creep. The patterns are also rotated so that the $\bar{\Gamma}\bar{\mathrm{M}}$ direction runs vertically, and the $\bar{\Gamma}\bar{\mathrm{K}}$ direction runs horizontally.

With some knowledge of the symmetry of the lattice, symmetrization of the Fourier transform can enhance the detail of the dispersive features. In our case, the 3×3-Pb lattice has 3-fold rotational symmetry and mirror symmetry along the $\bar{\Gamma}\bar{\mathrm{M}}\bar{\Gamma}$ axis. The patterns after distortion correction and 3-fold symmetry averaging is given in row 3 in Figure 1, followed by mirror symmetry averaging in row 4. Additionally, following the technique explained in the Supplementary Information in Ming *et al.* (2017), the low $\mathbf{q}$ features in the patterns are unrelated to the electronic structure. Therefore, they are suppressed using a common Gaussian expression: $g_{supp}(\mathbf{q}, V) = g(\mathbf{q}, V) \times [1 - Gaussian(q = 0, \sigma)]$ where $\sigma = 1.97\pi/a$ (See Supplementary Information in Allan *et al.* (2012) and Ming *et al.* (2017)). The resulting images from this process are given in the last row in the figure.

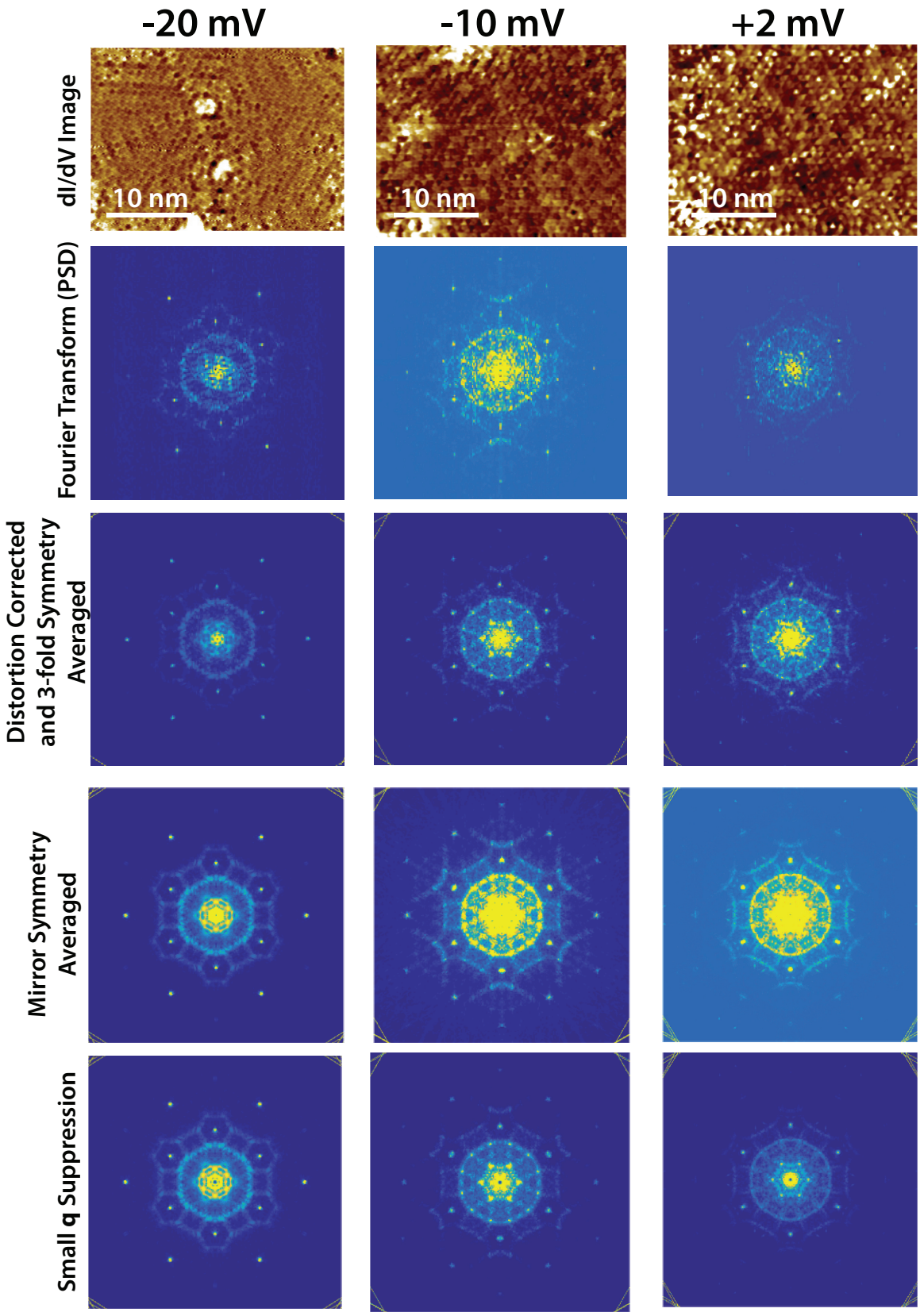

Figure 1: Examples of the processing procedure for the QPI data in Section 4.3.

Vita

Tyler S. Smith was born on October 10, 1989 in Nashville, Tennessee, United States. He attended Lee University (LU) in 2008 after graduating from Greenbrier High School. He spent four years in LU and obtained a Bachelor's degree in Mathematics in 2012. In August 2012, he joined the physics department of University of Tennessee as a graduate student. Three years later, he joined Dr. Hanno Weitering's research group. Since then, he spent five years in the experimental study of adsorbate doping of triangular adatom systems on semiconducting surfaces at the Science and Engineering Research Facility (SERF) and the Joint Institute for Advanced Materials (JIAM) at the University of Tennessee. Throughout his time working under Dr. Weitering, he was the author or coauthor of six peer reviewed journal articles. He expects to receive his Doctorate of Philosophy degree in Physics in August of 2020.